UNIVERSITÀ DEGLI STUDI DI TRIESTE

XXXVIII CICLO DEL DOTTORATO DI RICERCA IN NANOTECNOLOGIE

Airborne exposure, skin contamination and skin absorption to gallium arsenide and other metals in nano dimensions

Settore scientifico-disciplinare: MED/44

DOTTORANDO

MARCO RIZZO

COORDINATORE

PROF. ALBERTO MORGANTE

SUPERVISORE DI TESI

PROF. FRANCESCA LARESE FILON

PROF. MATTEO CROSERA

ANNO ACCADEMICO 2024/2025

Sommario

1. INTRODUCTION

Nanomaterials are a class of materials that possess at least one external dimension in the nanoscale range, typically between 1 and 100 nanometers ('ISO 80004-1:2023(En), Nanotechnologies – Vocabulary — Part 1: Core Vocabulary', n.d., 800). This incredibly small size provides them with unique physicochemical properties that differ significantly from their bulk counterparts. These properties include increased surface area to volume ratio, enhanced reactivity, and quantum effects, making them highly desirable for a wide range of applications (Saleh 2020).

The exceptional properties of nanomaterials have fueled their rapid integration into various industrial sectors (Z. Janković and L. Plata 2019). In materials science, they enable the development of lightweight, high-strength composites for aerospace, automotive, and sporting goods applications. In electronics, they facilitate the fabrication of smaller, faster, and more efficient computer chips and electronic devices.

Nanomaterials also play a crucial role in addressing global challenges (Koltsov and Koltsov 2017). In environmental science, they are used for water purification, pollution remediation, and the development of sustainable energy technologies. In medicine, they are revolutionizing drug delivery, diagnostics, and therapeutics, offering targeted and personalized treatments.

The expanding utilization of nanomaterials across diverse industrial sectors has prompted a rigorous examination of their potential toxicological implications for human health and environmental sustainability. While the unique physicochemical properties of these materials offer significant technological advancements, a balanced assessment of their potential risks is necessary (Ganguly et al. 2018; Sayes and Warheit 2009; Sahu and Hayes 2017).

The observed differences in biological behavior between nanomaterials and their bulk counterparts are primarily attributed to their increased surface area-to-volume ratio (Khushnood 2024). This characteristic enhances their reactivity, potentially leading to increased interactions with biological molecules and cellular structures (Joudeh and Linke 2022). However, it is crucial to acknowledge that

this increased reactivity does not automatically equate to heightened toxicity. The nature and extent of these interactions are highly dependent on the specific nanomaterial, its surface modifications, and the biological context.

Several key aspects that are crucial for understanding their interactions with biological systems (Gatoo et al. 2014). These factors include the size, shape, surface charge, chemical composition, and surface modifications of nanoparticles, as well as the integrity of biological barriers they encounter (Xuan et al. 2023). The size of nanoparticles is a critical determinant of their biological effects. Smaller nanoparticles have a higher surface area-to-volume ratio, which enhances their reactivity and ability to interact with cellular components. This increased reactivity can lead to greater biological activity, including the potential for inducing oxidative stress and inflammation. For instance, nanoparticles smaller than 100 nm can more easily penetrate biological barriers such as the blood-brain barrier (BBB), making them effective for drug delivery to the central nervous system but also raising concerns about potential neurotoxicity. The shape of nanoparticles also influences their biological interactions. Different shapes, such as spheres, rods, and cubes, can affect how nanoparticles are taken up by cells and how they distribute within tissues (Demir 2021). For example, rod-shaped nanoparticles have been shown to have higher cellular uptake compared to spherical nanoparticles, which can enhance their therapeutic efficacy but also their potential toxicity.

The chemical composition of nanoparticles determines their intrinsic properties, such as solubility, stability, and reactivity. Metallic nanoparticles, such as those made from gold, silver, or zinc oxide, can generate reactive oxygen species (ROS) through various mechanisms, including surface oxidation and interaction with cellular components (Fallah et al. 2024). The generation of ROS by metallic nanoparticles is highly dependent on their size, shape, and surface chemistry (Abdal Dayem et al. 2017). The generation of ROS can lead to oxidative stress, which can damage cellular structures and induce inflammatory responses (Wen et al. 2020). Surface modifications of nanoparticles can significantly influence their biocompatibility and interactions with biological systems.

The ability of nanoparticles to cross biological barriers, such as skin, lungs, and blood-brain barrier, is a subject of ongoing investigation. This property raises concerns about potential systemic toxicity but also offers opportunities for targeted drug delivery and diagnostic applications. The extent to which nanoparticles can penetrate these barriers is influenced by their size, surface modifications, and the integrity of the barrier itself. For instance, nanoparticles can penetrate skin through hair follicles, sweat glands, and intercellular pathways, with their ability influenced by size, surface charge and hydrophobicity (Crosera et al. 2009; Larese Filon et al. 2015).

Inhaled nanoparticles can be deposited in various regions of the respiratory tract, and their deposition and clearance are influenced by several factors, including size, shape, and surface properties (Lizonova et al. 2024; Geiser and Kreyling 2010). When nanoparticles are inhaled, they travel through the respiratory system and can be deposited in different regions, such as the nasal passages, trachea, bronchi, and alveoli. The deposition pattern is largely determined by the size of the nanoparticles. Smaller nanoparticles (less than 100 nm) tend to reach the deeper regions of the lungs, such as the alveoli, where gas exchange occurs. Larger particles are more likely to be deposited in the upper respiratory tract.

The shape of nanoparticles also plays a crucial role in their deposition (Lin et al. 2015). For example, rod-shaped nanoparticles have been shown to have different deposition patterns compared to spherical nanoparticles. This is due to differences in how they interact with the airflow and the surfaces of the respiratory tract.

The surface charge of nanoparticles significantly influences their interactions with the respiratory tract lining and their subsequent clearance. Similarly charged particles exhibit repulsion, preventing them from grouping. Conversely, neutral particles readily agglomerate (Braakhuis et al. 2014). Positively charged nanoparticles tend to interact more strongly with the negatively charged components of mucus and epithelial cells, enhancing their retention and penetration. This can lead to increased deposition in the respiratory tract and potentially greater biological effects. Conversely, negatively

charged or neutral nanoparticles may exhibit reduced interactions, leading to faster clearance from the respiratory tract.

The mechanisms underlying nanoparticle toxicity are complex and multifaceted. Cellular uptake, a critical step in nanoparticle-induced effects, can occur through various endocytic pathways (Foroozandeh and Aziz 2018). However, the efficiency of these pathways varies depending on the nanoparticle's properties and the cell type. Intracellular interactions with organelles, such as mitochondria and lysosomes, can potentially disrupt cellular function. However, the extent of this disruption is highly dependent on the nanoparticle's composition, size, and surface modifications.

The inflammatory response, a common consequence of nanoparticle exposure, is a complex process involving the activation of immune cells and the release of cytokines. While some nanoparticles can induce pro-inflammatory responses, others have been shown to possess anti-inflammatory properties. The nature and extent of the inflammatory response are influenced by the nanoparticle's properties and the biological context.

NP’s genotoxic potential is influenced by several factors, including composition, size, surface modifications, and cell type. Nanoparticles may damage DNA directly or indirectly and can also alter epigenetic regulation. Metal-based nanoparticles can generate reactive oxygen species (ROS), leading to oxidative stress and DNA damage (Kohl et al. 2020; Shukla et al. 2021). ROS can cause single and double-strand breaks, base modifications, and crosslinking, all of which disrupt normal cellular processes like replication and transcription. Beyond direct DNA damage, nanoparticles can interfere with mitotic spindle formation and chromosome segregation, leading to aneuploidy and other chromosomal abnormalities. Moreover, NPs can penetrate the nucleus and interact directly with DNA, further amplifying their genotoxic effects.

Epigenetic alterations represent another pathway through which nanoparticles exert genotoxicity. These include changes in DNA methylation patterns, histone modifications, and the expression of non-coding RNAs, all of which can dysregulate gene expression without altering the DNA sequence itself.

1.1 METAL NANOPARTICLES APPLICATIONS

Metal nanoparticles (MNPs) have attracted considerable interest because of their distinctive physicochemical properties, which make them highly suitable for a wide range of applications in medicine, industry, and environmental science.

In the biomedical field, metal nanoparticles such as gold (Siddique and Chow 2020) and silver (Huy et al. 2020) are used as carriers for drug delivery. Their small size allows them to penetrate cells easily, delivering drugs directly to target sites, which enhances therapeutic efficacy and reduces side effects. Additionally, magnetic nanoparticles can be guided to specific locations in the body using external magnetic fields, providing targeted treatment (Ghazi et al. 2025). Silver nanoparticles exhibit strong antimicrobial properties (González-Fernández et al. 2025) and are used in wound dressings, coatings for medical devices, and water purification systems to prevent bacterial infections. They disrupt bacterial cell membranes and interfere with cellular processes, leading to bacterial death. Gold nanoparticles are employed in photothermal therapy, where they are used to target and destroy cancer cells with minimal damage to surrounding healthy tissues (Badir et al. 2025). They can also be used in combination with other therapies, such as chemotherapy and radiotherapy, to enhance treatment efficacy. Metal nanoparticles are also used in imaging techniques such as MRI and CT scans (Saadh et al. 2025). Iron oxide nanoparticles, for example, enhance the contrast in MRI images, aiding in the accurate diagnosis of diseases.

In industrial applications, metal nanoparticles, including platinum (Li et al. 2023; 2023) and palladium (Zhou and Astruc 2024), are widely used as catalysts in chemical reactions due to their large surface area and high reactivity. They are essential in processes like hydrogenation and oxidation, significantly increasing reaction rates and selectivity, making industrial processes more efficient. Silver nanoparticles are used in conductive inks for printed electronics, which are essential for manufacturing flexible electronic devices and circuits (J. Zhang et al. 2022). They enable the creation of lightweight, flexible, and highly conductive components for various electronic applications. Metal nanoparticles are

also used in the development of high-performance batteries. For example, lithium iron phosphate nanoparticles are used in lithium-ion batteries to improve their energy density and charge-discharge rates, contributing to longer-lasting and more efficient energy storage solutions (Zhang et al. 2025).

In environmental applications, metal nanoparticles are used in the removal of pollutants from water and air (Pandiyaraj et al. 2023). For example, iron nanoparticles can degrade organic pollutants in contaminated water through reduction reactions. They can also be used to remove heavy metals and other toxic substances from the environment. Metal oxide nanoparticles, such as zinc oxide (Kumar et al. 2015) and titanium dioxide (Ramanavicius et al. 2022), are used in gas sensors to detect environmental pollutants like carbon monoxide and nitrogen dioxide due to their high sensitivity and selectivity. These sensors can provide real-time monitoring of air quality and help in the early detection of hazardous substances. Metal nanoparticles can also be used to clean up oil spills and other environmental contaminants (Hethnawi et al. 2023). Their high surface area and reactivity make them effective in breaking down complex pollutants into less harmful substances.

The unique physicochemical properties of metal nanoparticles, such as their small size, high surface area, optical properties, magnetic properties, catalytic activity, and thermal stability, make them versatile and valuable in advancing technology across multiple fields. These properties enable metal nanoparticles to interact with biological systems at the molecular level, enhance the efficiency of industrial processes, and provide effective solutions for environmental remediation.

1.2 METAL NANOPARTICLES TOXICITY

Metal nanoparticles (MNPs) have become increasingly prevalent in various fields, including medicine, electronics, and environmental science, due to their unique properties. However, their widespread use has raised concerns regarding their potential toxicity to humans and the environment. Understanding the mechanisms of MNP toxicity is crucial for developing safer nanomaterials and mitigating their adverse effects.

MNPs are typically defined as particles with at least one dimension in the nanoscale range (1-100 nm). Their small size and high surface area-to-volume ratio confer unique physicochemical properties, such as enhanced reactivity and catalytic activity, which are beneficial for various applications. However, these same properties can also contribute to their toxicity. The toxicity of MNPs is influenced by several factors, including size, shape, surface charge, chemical composition, and the presence of surface coatings or functional groups (Sengul and Asmatulu 2020; Y.-L. Wang et al. 2024).

MNP-induced oxidative stress can be articulated into two categories according to the mechanisms of activation. The primary mechanisms of MNP toxicity is the generation of reactive oxygen species (ROS) (Kessler et al. 2022; N. Zhang et al. 2022). When MNPs enter biological systems, they can interact with cellular components and induce the production of ROS via different surface-related processes. ROS are highly reactive molecules that can cause oxidative stress, leading to cellular damage. Additionally, metal nanoparticles and the ions they release can cause secondary effects by participating in Fenton-like and Haber-Weiss reactions (Angelé-Martínez et al. 2017), ultimately enhancing oxidative reactions, where hydrogen peroxide (H_2O_2) is converted into various radicals. This oxidative stress can damage proteins, lipids, and DNA, leading to inflammation, apoptosis, and other adverse effects (Sengul and Asmatulu 2020).

Indirect oxidative stress, also known as secondary oxidative stress, occurs when nanoparticles (NPs) are not the direct cause of oxidative stress. When MNPs are internalized, they release metal ions that can depolarize the mitochondrial membrane and disrupt the electron transport chain, leading to mitochondrial dysfunction. In mitochondria, molecular oxygen is used to produce adenosine triphosphate (ATP) through a series of coupled proton and electron transfer reactions during normal physiological processes. (Y.-L. Wang et al. 2024). Exposure to metal-based NPs can disrupt the mitochondrial electron transport chain (METC), resulting in increased levels of intracellular reactive oxygen species (ROS).

The size of MNPs plays a critical role in their toxicity (Attarilar et al. 2020). Smaller nanoparticles have a larger surface area relative to their volume, which can enhance their reactivity and potential to

generate ROS. Additionally, smaller particles can more easily penetrate biological membranes and accumulate in tissues, leading to higher toxicity. The shape of MNPs also affects their toxicity (Medici et al. 2021). Different shapes, such as spheres, rods, and cubes, can interact differently with biological systems. For example, rod-shaped MNPs may cause more mechanical damage to cells compared to spherical nanoparticles.

Surface charge and chemical composition are other important factors influencing MNP toxicity (Sukhanova et al. 2018). Positively charged nanoparticles tend to interact more strongly with negatively charged cellular membranes, leading to higher uptake and potential toxicity. The chemical composition of MNPs determines their solubility and reactivity. For instance, metal oxide nanoparticles, such as zinc oxide (ZnO) (Senapati and Kumar 2018; Creutzenberg et al. 2022) can dissolve and release metal ions, which can contribute to their toxicity. The presence of surface coatings or functional groups can modify the interactions of MNPs with biological systems. Coatings can enhance the stability and biocompatibility of nanoparticles, reducing their toxicity.

The route of exposure to MNPs also affects their toxicity (Srikanth 2020). Inhalation, ingestion, and dermal contact are common routes of exposure.

Airborne exposure to nanoparticles may pose potential health risks to humans since particles with diameters between 1 nm and 10 µm typically have a residence time in atmosphere of about one week, make them challenging to remove from the air. Inhalation represents the primary and most critical route of exposure, as nanoparticles possess the ability to penetrate deeply into the respiratory system (Sonwani et al. 2021; Akter et al. 2024). The main deposition mechanism for nanoparticles is Brownian diffusion, caused by random motion due to collisions with air molecules. It has been observed that nanoparticle toxicity correlates more accurately with the surface area deposited in the lungs rather than with mass concentration. There are significant differences between nanoparticles and larger particles regarding their behavior during deposition and clearance in the respiratory tract. Particles with a diameter ≥ 5 µm (coarse fraction) typically deposit in the upper airways (nose, pharynx, larynx, trachea, bronchi); those with diameters between 1 and 5 µm (fine fraction) reach the terminal portion

of the respiratory tree (terminal bronchioles, alveoli); ultrafine particles, with diameters < 1 μm, concentrate in the alveolar region, where they can be rapidly absorbed.

Nanoparticles exhibit potentially high toxicity even at low concentrations, as they can carry organic contaminants adsorbed on their surface and generate reactive oxygen species (ROS) due to their high specific surface area. Due to their extremely small size, after penetrating deep into the lungs, MNPs are capable of crossing alveolar cell membranes, and even entering the bloodstream. (Leikauf et al. 2020; Sonwani et al. 2021; Portugal et al. 2024). This can lead to systemic distribution throughout the body, potentially reaching other organs and tissues such as cardiovascular system and brain.

For instance, iron oxide nanoparticles can induce oxidative stress, leading to DNA damage, which has been observed in both human lung epithelial cells and individuals exposed to welding fumes. Additionally, these nanoparticles can trigger inflammation in the respiratory system, with studies showing increased expression of inflammatory genes like IL-6 and IL-8 in cells exposed to iron oxide nanoparticles (Thanachoksawang et al. 2022).

Migration of MNPs in the bloodstream can furthermore impact the cardiovascular system, due to oxidative stress and inflammation caused by ROS species. These processes are implicated in the development of cardiovascular diseases such as hypertension and atherosclerosis (Scafa Udriște et al. 2024; Ichihara 2025).

Nanoparticles have also the ability to to cross the blood-brain barrier (BBB), which can lead to various neurotoxic effects (Teleanu et al. 2018). For instance, they can induce oxidative stress, resulting in cell apoptosis and autophagy, immune responses, and neuroinflammation. For instance iron oxide nanoparticles can cross the blood-brain barrier or enter the brain through the olfactory nerve, making them valuable for drug delivery and imaging diagnostics in the nervous system. However, this same ability also contributes to their neurotoxicity. Studies have shown that daily exposure to iron oxide nanoparticles can disrupt synaptic transmissions and nerve conduction, leading to neural inflammation, cell death (apoptosis), activation of neural antioxidant responses, and infiltration of immune cells (Valdiglesias et al. 2016).

Dermal exposure can lead to the penetration of nanoparticles through the skin and subsequent distribution to other tissues. The biodistribution and accumulation of MNPs in different organs can lead to organ-specific toxicity.

When nanoparticles come into contact with the skin, they can penetrate the stratum corneum, the outermost layer of the skin, and reach deeper layers. This penetration is influenced by several factors, including the size, shape, and surface properties of the nanoparticles, as well as the condition of the skin (Crosera et al. 2009; Zanette and Maina 2009; Larese Filon et al. 2015; Larese Filon, Bello, et al. 2016). Depending on the physicochemical properties of a compound, MNPs can penetrate the skin through four distinct pathways: intercellular, transcellular, and two transappendageal routes, which involve hair follicles and sweat glands (Brouwer et al. 2016). The extent of dermal uptake can be influenced by various factors, including the amount of substance applied, the area of skin exposed, the duration of contact, the specific body site, the thickness and integrity of the skin layers, sweating, temperature, humidity, physical activity, gender, race, age, the properties of the substance, the vehicles used, and the presence of skin conditions such as allergic and irritant contact dermatitis, atopic eczema, and psoriasis. Additionally, mechanical flexions, exposure to irritant detergents, and chemicals can enhance skin absorption (Filon et al. 2006).

MNPs skin penetration can lead to allergic sensitization, resulting in allergic contact dermatitis through a delayed-type hypersensitivity reaction (Larese Filon 2017). This type of reaction occurs when the immune system responds to the presence of metals by releasing inflammatory mediators, causing redness, itching, and swelling at the site of contact. Furthermore, metals can permeate the skin and enter the bloodstream, potentially leading to systemic intoxication. This is particularly concerning for highly toxic metals, such as dimethylmercury, which can cause severe health effects even at low exposure levels. Systemic intoxication can manifest in various ways, including neurological symptoms, organ damage, and other systemic effects depending on the specific metal and the extent of exposure.

Unintended exposure to nanoparticles through ingestion can pose health risks, including potential toxicity and immune responses (Frey et al. 2019). When nanoparticles are ingested, they first

encounter the acidic environment of the stomach, which can affect their stability and surface properties. As they move into the intestines, they interact with various components of the gastrointestinal tract, including the mucus layer, epithelial cells, and immune cells.

The nanoparticles can be absorbed primarily in the small intestine, where they may cross the epithelial barrier through several mechanisms. These include transcellular transport, where nanoparticles are taken up by enterocytes and transported across the cell, and paracellular transport, where they pass between the cells. Additionally, specialized cells such as M cells in the Peyer's patches can facilitate the uptake of nanoparticles and their transport to underlying immune cells (Y. Wang et al. 2024).

Once nanoparticles cross the intestinal barrier, they can enter the bloodstream and be distributed throughout the body. The physicochemical properties of the nanoparticles, such as size, shape, surface charge, and coating, play a crucial role in determining their absorption and biodistribution. For instance, smaller nanoparticles are more likely to be absorbed and distributed systemically compared to larger ones.

1.3 THE RESEARCH PROJECT

The research project focused on assessing occupational exposure to metallic nanomaterials within research activities and was developed along the following lines:

- Characterization of dermal and airborne exposure, as well as biological markers associated with exposure to gallium arsenide (GaAs) nanoparticles in a research laboratory, using a tiered approach, and evaluation of the effectiveness of the mitigation measures implemented.
- Characterization of transdermal absorption of GaAs nanoparticles through an ex-vivo approach using Franz diffusion cells.
- Characterization of transdermal absorption of CdS quantum dots, also conducted via an ex-vivo approach using Franz diffusion cells.

This research project aims to provide a comprehensive assessment of occupational exposure to metallic nanomaterials through an integrated approach combining field-based monitoring and controlled laboratory investigations. The primary objective is to characterize both dermal and airborne exposure to gallium arsenide nanoparticles within an active research laboratory setting, employing a tiered assessment strategy that enables effective real-world exposure evaluation. This characterization extends beyond simple detection to include the characterization of biological markers that can serve as indicators of exposure, thereby establishing important tools for occupational health surveillance programs.

A critical component of this objective involves evaluating the effectiveness of mitigation measures implemented in the research laboratory, providing evidence-based guidance for developing protective strategies that can be adopted across similar research environments. The project seeks to determine whether current control measures adequately reduce exposure to acceptable levels and to identify potential gaps in protection that require enhanced intervention.

Complementing the workplace exposure assessment, the research aims to elucidate the mechanisms of transdermal absorption for gallium arsenide nanoparticles and cadmium sulfide quantum dots through systematic ex-vivo studies utilizing Franz diffusion cells. These investigations are designed to quantify penetration kinetics, determine the extent to which these metallic nanoparticles can traverse intact skin barriers, and establish comparative absorption profiles across different nanomaterial types. The controlled nature of these studies allows for precise characterization of factors influencing skin penetration while eliminating the confounding variables inherent in workplace exposure scenarios.

Ultimately, this research endeavors to generate data that directly informs the development of material-specific occupational exposure guidelines, enhances risk assessment frameworks for emerging nanomaterials, and strengthens the scientific foundation for protecting workers engaged in nanotechnology research while enabling continued innovation in this rapidly advancing field.

2. EXPOSURE TO GALLIUM ARSENIDE NANOPARTICLES IN A RESEARCH FACILITY: A CASE STUDY USING MOLECULAR BEAM EPITAXY

2.1 GALLIUM ARSENIDE NANOMATERIALS

Gallium arsenide (GaAs) is a III-V compound semiconductor distinguished by its direct bandgap, rendering it suitable for devices that emit and absorb both visible and infrared light. GaAs exhibits a low reverse saturation current, which mitigates noise and leakage current, thereby enhancing performance and reliability. Additionally, it possesses high electron mobility, approximately five times greater than that of silicon (Sze et al. 2021). GaAs devices demonstrate superior stability and precision due to their exceptional temperature sensitivity, resulting in less volatility in electrical properties with temperature fluctuations compared to silicon devices. Furthermore, GaAs has a high breakdown voltage, enabling devices to endure higher biases in reverse-biased unipolar and bipolar configurations (Sze et al. 2021). This contributes to increased efficiency and power handling capabilities.

These attributes render GaAs devices ideal for a wide range of applications, including microwave frequency integrated circuits, monolithic microwave integrated circuits, infrared LEDs, laser diodes, and solar cells (Fang et al. 1990). Gallium arsenide (GaAs) is synthesized in thin films using Molecular Beam Epitaxy (MBE) technique. Molecular beam epitaxy (MBE) is an ultra-high vacuum technique employed to produce high-quality epitaxial structures of semiconductors, metals, insulators, and superconductors with monolayer precision. This method facilitates precise control over material properties, such as composition and doping levels, at the sub-nanometer scale (Biasiol G. 2001).

The Molecular Beam Epitaxy (MBE) system is designed to epitaxially grow III-V compound semiconductors on a heated crystalline substrate under ultrahigh vacuum conditions (10^{-11} mbar). This high vacuum is crucial to prevent contamination and ensure the purity of the grown films. The process

involves ultra-pure elements, such as gallium and arsenic, which are placed in separate effusion cells or electron-beam evaporators. Group-III elements (such as gallium, indium, and aluminum) and the Group-V element (arsenic) are placed in four effusion cells, which are heated to temperatures up to 1400°C to produce molecular beams of the elements. The high temperature and extremely low pressure cause the metals to evaporate. These evaporated metals then deposit onto the heated crystalline substrate. Precise control of the partial pressures of the metals is crucial: the partial pressure of the Group-III elements must be maintained at 10^{-7} mbar, while the Group-V element's partial pressure should be kept at 10^{-5} mbar. If the pressure drops below these levels, the deposited compounds may re-evaporate, thereby slowing the growth of the thin film.

In high-frequency electronics, GaAs thin films are extensively used in devices such as microwave frequency integrated circuits and monolithic microwave integrated circuits (MMICs). The high electron mobility of GaAs allows for faster signal processing and higher efficiency compared to silicon-based devices. This makes GaAs ideal for applications in radar systems, satellite communications, and wireless networks.

GaAs thin films are also crucial in the fabrication of optoelectronic devices, including infrared LEDs, laser diodes, and photodetectors. The direct bandgap of GaAs enables efficient light emission and absorption, making it suitable for devices that operate in the visible and infrared spectrum. These devices are used in various applications, such as fiber-optic communications, medical diagnostics, and environmental monitoring.

In the field of solar energy, GaAs thin films are used in high-efficiency solar cells. The material's ability to absorb a wide range of wavelengths and convert them into electrical energy makes GaAs solar cells highly efficient. These cells are particularly valuable in space applications, where high power-to-weight ratios are essential.

GaAs thin films can also be used in advanced quantum computing and quantum communication systems. These devices leverage the unique quantum properties of GaAs to perform complex computations and secure communications.

The precise control over thickness and composition provided by MBE allows for the fabrication of complex photonic structures. These structures are used in applications such as optical modulators and switches, which are essential components in modern telecommunication networks.

Additionally, GaAs thin films are used to manufacture high-speed transistors, including metal-oxide-semiconductor field-effect transistors (MOSFETs) and heterojunction bipolar transistors (HBTs). These transistors are critical for high-speed digital circuits and RF amplifiers.

2.2 GALLIUM ARSENIDE TOXICITY

Studies conducted in mice have demonstrated that gallium arsenide (GaAs) is highly immunotoxic and carcinogenic (Hartmann et al. 2005). In vitro experiments revealed that blood arsenic (As) levels increased with dosage after administration of GaAs particles, while gallium (Ga) was not detected (Webb et al. 1984). Bulk GaAs can dissolve in the presence of an immune reaction due to reactive oxygen species (ROS) released by macrophages, leading to carcinogenic effects on the lungs, skin, and bladder and is associated with cardiovascular (Khairul et al. 2017; Moon et al. 2018). GaAs can dissolve into As and Ga, causing systemic toxicity (Carter et al. 2003). Acute toxicity data for GaAs administered orally, topically, or intraperitoneally in animals showed low toxicity (Repetto et al. 2023). Male F344 rats intratracheally instilled with GaAs particle suspensions (100 mg/kg body weight = equimolar Ga dose) exhibited increased lipid content, lymphoid hyperplasia, multifocal macrophages in the alveoli, pneumocyte hyperplasia, proliferative pneumonia, necrotic cells in the alveoli, and perivascular cuffing (Webb et al. 1984; 1986). Persistent pulmonary alveolar proteinosis and alveolar histiocytic infiltrates were observed in rats and mice during subchronic inhalation experiments at the lowest tested concentrations (Bomhard et al. 2013; Bomhard 2020). Smaller-sized GaAs particles caused more severe acute pulmonary lesions, mild pulmonary fibrosis, and significant inflammatory responses upon intratracheal administration.

Ga oxide deposits in the lungs were detected without inflammation and minimal absorption in the blood; As acid increased levels of 4-hydroxyproline, indicating a fibrotic process. As oxide showed acute lung toxicity and systemic damage due to rapid absorption. Toxicity mechanisms include oxidative and mitochondrial damage, potentially leading to cancers, atherosclerosis, diabetes mellitus (Nurchi et al. 2020), cardiovascular events, high blood pressure, and arrhythmias (Ratnaike 2003). In the lungs, As can cause cancer [Wei et al., 2019] and non-neoplastic lesions such as non-malignant pulmonary nodules, emphysema, and interstitial diseases (Ergün et al. 2017). The sensory part of the nervous system is primarily affected, with symptoms including glove and stocking anesthesia, paresthesia, fatigue, headache, fear and anxiety, vertigo, irritability, confusion, memory loss, behavioral changes, and cognitive impairment in some cases (Ratnaike 2003).

Exposure to GaAs nanoparticles in animals interferes with the immune system (Gondre-Lewis et al. 2003), can cause tumors (Borm et al. 2006), and toxicity to the lungs, kidneys, and reproductive organs (Tanaka 2004). Cytotoxicity assessments using human epithelial cells (16HBE14o-a) revealed that GaAs nanoparticles dissolved quickly in the bioassay medium, releasing large amounts of toxic soluble As, while soluble Ga concentrations were very low. The molar ratio of dissolved As to Ga in corrosion experiments on day seven exceeded 8,000. Speciation studies indicated that As (III) is primarily responsible for the cytotoxicity of GaAs nanoparticles. Intratracheal instillation of GaAs (mean volume diameter 5.8 microns) in male Syrian golden hamsters showed that after four days, the ratio of the two major urinary metabolites (dimethylarsinic acid/total inorganic As species) was 1.41, with over half of the dosage eliminated via urine due to the rapid excretion of arsenite and arsenate (Rosner and Carter 1987). After oral or pulmonary doses of GaAs, significant quantities of As were detected in blood and urine samples, but no Ga was found (Carter et al. 2003).

For what concerns dermal exposure, experiments on Rhesus monkeys (Wester et al. 1993; Lowney et al. 2005; 2007) indicated that arsenic absorption through the skin from soil is minimal. Similarly, Villegas et al. (Marin Villegas and Zagury 2023) conducted tests on arsenic skin permeation using synthetic skin and two synthetic sweat formulations (pH 6.5 and pH 4.7). They found that arsenic was

primarily present as arsenate (As(V)) in both sweat types, concluding that arsenic cannot permeate the skin since arsenate's ionic nature, low lipid solubility, and lack of transformation into more permeable species make it highly unlikely to penetrate the skin.

Ouypornkochagorn and Feldmann (Ouypornkochagorn and Feldmann 2010) demonstrated that arsenic penetration and accumulation depend significantly on its speciation, with arsenite, an inorganic form of arsenic, being particularly well-absorbed through the skin. Li et al. (Li et al. 2024) examined the skin bioaccessibility of arsenic from contaminated road dust using an artificial sweat simulation method (pH 6.5), finding potential for skin absorption.

Due to the high toxicity of As, the use of GaAs could pose adverse effects to exposed workers if As is released. Therefore, exposure to As and Ga in a research facility involved in the production of GaAs nanofilms was investigated.

2.3 OCCUPATIONAL EXPOSURE ASSESSMENT

In a recent systematic review by Galey et al. (Galey et al. 2023) were analyzed 23 international strategies aimed at evaluating workplace exposure to airborne nanoparticles (NPs).

A significant portion of these strategies (two-thirds of reviewed documents) employed tiered approaches, typically beginning with a preliminary situation study using simpler tools, followed by more in-depth field studies with complex instrumentation.

This methodology is characterized by starting with preliminary studies that employ simpler, less complex tools, and then progressing to more extensive field studies that involve multiple instruments. The fundamental objective of such an approach is to provide increasingly refined information regarding exposure as the complexity of the field study increases.

Over time, several harmonized tiered strategies have emerged, including EN 17058 ('UNI EN 17058:2019 - UNI Ente Italiano Di Normazione', n.d.), NIOSH (*NIOSH Risk Assessment of Engineered*

Nanomaterials | Blogs | CDC 2024), and OECD (OECD, n.d.), which specifically highlight the operational nature of these strategies.

The recommended approach for evaluating exposure to airborne nanoparticles (NPs) involves a structured, tiered strategy. This strategy is divided into two main operational stages: an initial (preliminary) assessment followed by a more detailed (in-depth) evaluation.

The preliminary assessment phase aims to gather initial information to formulate hypotheses about potential exposure situations that warrant further investigation during the in-depth assessment. This involves collecting data on aspects such as potential exposure, types of activities, materials and processes used, existing risk assessments and work procedures, company operations, the work environment, organizational structure, ventilation systems, and specific work-related and preventive equipment. Alongside this, directed interviews with company stakeholders, including management, occupational health professionals, and workers, are crucial for identifying potential exposure scenarios and perspectives.

Simple observations of work situations that could lead to exposure are combined with real-time measurements of both number and mass concentrations at nanoscale (or submicron scale) and microscale, performed both within the workplace and outdoors, to map out particle sources.

Airborne exposure represents the main route of exposure to nanoparticles and involves the inhalation of extremely small particles—typically less than 100 nanometers in diameter—that are suspended in the air.

Because of their nanoscale size, these particles exhibit unique behavior in the respiratory system. Unlike larger particles that are often trapped in the upper airways, nanoparticles can bypass the body's natural filtration mechanisms. They are capable of penetrating deep into the lungs, reaching the alveolar region where gas exchange occurs. From there, some nanoparticles may translocate across the alveolar-capillary barrier and enter the bloodstream, potentially distributing to other organs such as the liver, spleen, heart, and even the brain.

This deep penetration and systemic distribution raise concerns about potential health effects, including respiratory inflammation, oxidative stress, cardiovascular issues, and long-term chronic conditions. The small size and high surface area of nanoparticles also mean they can carry adsorbed toxic substances, further increasing their potential biological reactivity.

Real-time monitoring of airborne nanoparticles is crucial for assessing exposure in both environmental and occupational settings. The most widely used instruments for this purpose are the Scanning Mobility Particle Sizer (SMPS) , the Condensation Particle Counter (CPC) and the DiSCmini (Liu et al. 2014; Bau et al. 2015; Ham et al. 2016).

Crucially, information on the work activity itself is also gathered, often through recordings of the work tasks and activities performed.

NP chemical characterization can be performed through airborne sampling using techniques such as IOM sampler and Sioutas Cascade Impactor (PCIS).

After personal airborne sampling, laboratory-based methods such as Transmission Electron Microscopy (TEM) and Scanning Electron Microscopy (SEM) can be implemented for the detailed characterization of nanoparticles after they have been collected from the air.

Personal airborne samples can be also chemically analyzed to determine the concentration and composition of metal nanoparticles. This is typically done using Inductively Coupled Plasma Mass Spectrometry (ICP-MS), a highly sensitive technique capable of detecting trace levels of metals in complex matrices.

Another route of occupational possible exposure is related to dermal contamination.

Dermal exposure is an important but often under-recognized route of nanoparticle exposure, especially in occupational settings where workers handle nanomaterials directly or indirectly. Unlike inhalation, which has been more extensively studied, dermal exposure involves the contact of nanoparticles with the skin, potentially leading to local or systemic effects depending on the particle properties and skin condition.

The primary objective of assessing dermal exposure to nanoparticles is to comprehensively understand the mechanisms of occupational exposure, evaluate the practicality and effectiveness of various preventive measures, and establish a conceptual framework for screening, prioritization, and assessment of preventive actions in occupational exposure scenarios (Brouwer et al. 2016; Larese Filon, Bello, et al. 2016).

Skin contamination can primarily occur through several key pathways. Direct contact involves the immediate transfer of nanoparticles from a bulk source to the skin or clothing without the material becoming airborne. This scenario, often involving hands, can happen through touching powders or liquid dispersions containing nanoparticles, or as a result of spills, splashes, or direct immersion. In these instances, the state and composition of the nanoparticles are presumed to remain consistent with their original source.

Another pathway is deposition from the air, where particles settle onto the skin or other surfaces from an air flow. While factors like air velocity relative to the skin, particle size, surface temperature (thermophoresis), and electrophoresis play a role, the deposition of nanoparticles from the air onto the skin is generally considered to be of marginal significance in terms of the mass deposited.

A particularly noteworthy route is transfer from contaminated surfaces, where contact with contaminated surfaces or objects leads to their transfer to the skin.

Finally, inadvertent ingestion can occur when contaminated hands or other body parts transfer nanoparticles to the peri-oral region, resulting in oral intake.

The potential for nanoparticles to penetrate the skin is influenced by several factors, including their primary size, surface properties, and dissolution biokinetics, as well as the health of the skin. For rigid nanoparticles, size is a crucial determinant of skin permeation and penetration. Generally, nanoparticles greater than 45 nm (primary or agglomerate size) are not expected to penetrate or permeate healthy, intact skin, but this can occur in severely damaged skin. Particles between 21 and 45 nm typically penetrate only damaged skin, while those between 4 and 20 nm may permeate through hair follicles. Very small nanoparticles, less than 4 nm, have demonstrated skin penetration even

through intact skin. Notably, non-rigid or flexible nanoparticles, such as liposomes and micelles, can penetrate intact skin even at sizes greater than 4 nm due to their deformability.

Nanoparticles surface properties like charge and functional groups can influence penetration, but their exact role needs to be evaluated case-by-case. The dissolution of nanoparticles in sweat and skin-associated water is critically important, particularly for metal nanoparticles (e.g., Ni^{2+}) which can cause skin sensitization and allergic dermatitis. Nanoparticles are expected to have higher dissolution rates than their micron-sized counterparts due to their significantly larger surface-to-mass ratio. Nanoparticles can reside in hair follicles for extended periods, continuously releasing ions and increasing the risk of allergic contact dermatitis from sensitizing metals like nickel, palladium, or cobalt. Impurities in nanoparticles, such as transition metals used as catalysts or polyaromatic hydrocarbons (PAHs), can also be carried through the skin and then released, potentially leading to localized or systemic adverse effects.

Compromised skin integrity is a significant factor in nanoparticles skin penetration and permeation. Occupational irritant contact dermatitis (OCD), which indicates a disrupted skin barrier, is a good indicator of enhanced potential for nanoparticles uptake. In these scenarios, skin exposure to nanoparticles becomes a greater concern, especially if the nanoparticles contain sensitizing metals.

A structured, step-by-step methodology has been recommended for evaluating dermal exposure to nano-objects and their aggregates and agglomerates (NOAA) in workplace environments. This approach is formalized in the ISO/TS 21623:2017 standard, titled "Workplace exposure — Assessment of dermal exposure to nano-objects and their aggregates and agglomerates (NOAA)", which provides a comprehensive framework for systematically identifying, observing, and quantifying potential skin contact with nanomaterials in occupational settings ('ISO/TS 21623:2017(En), Workplace Exposure — Assessment of Dermal Exposure to Nano-Objects and Their Aggregates and Agglomerates (NOAA)', n.d.).

This approach begins with evaluating potential exposure scenarios, followed by observing worker tasks to identify contact points with nanomaterials. It includes quantifying nanoparticles on skin or

protective clothing using methods like surface wipe sampling, carbon adhesive tabs, and tape stripping. These techniques collect particles for analysis via ICP-MS, SEM, TEM, and EDS to determine metal content, morphology, and composition. The final step assesses the effectiveness of existing exposure controls in occupational and laboratory environments.

2.4 MATERIALS AND METHODS

2.4.1 THE LABORATORY

The chosen facility was a laboratory committed to the synthesis of GaAs thin films, destined to external industries for various applications. The synthesis of these films is assigned to a synthesizer (Molecular-Beam Epitaxy system), and to one worker, who has to extract the thin films from the Molecular-Beam Epitaxy (MBE) system, remove the samples from the substrates and cut the samples in pieces.

The MBE system is a machine that epitaxially grows III-V compound semiconductors on a heated crystalline substrate in ultrahigh vacuum conditions (10^{-11} mbar). The Group-III compounds (Ga, In, Al) and the Group-V compound (As) are put inside 4 effusion cells. These effusion cells get heated up to 1400°C. Due to the heat and to the extremely low pressure of the system, the metals start to evaporate. The evaporated metals deposit on the heated crystalline substrate. The partial pressure of the metals has to be extremely precise. To allow the precipitation of the metals the partial pressure of the group-III compounds has to be 10^{-7} mbar, and the one of the group-V compounds has to be maintained to 10^{-5} mbar. If the pressures get lower the precipitated compounds could evaporate again, slowing the growth of the thin film. The mean speed of deposition is 1 μm/h.

As visible in Figure 1, the MBE system was located in the middle of the laboratory, and it was surrounded by the workstations (computer desk, microscope desk, processing desk and main writing desk). Above the processing desk was installed a hood, in order to blow air downwards to clean the

table (the table has holes in it so that air can pass through it). Due to this, the micro- and nanocomponents on the table were blown down to the floor. So, a higher concentration was expected on the floor.

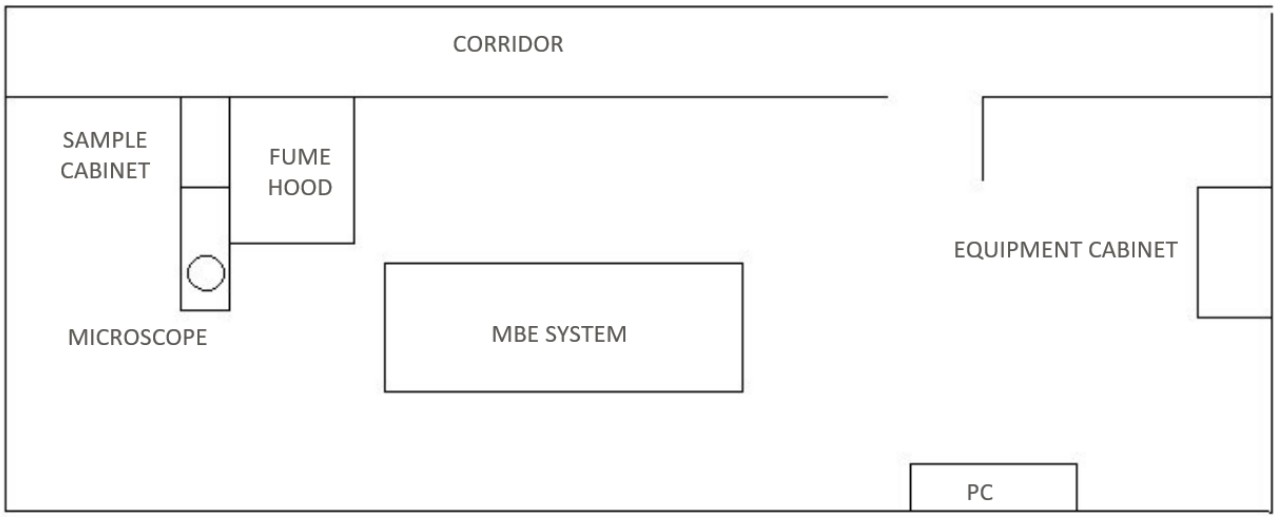

Figure 1: MBE laboratory layout

Before starting the sampling, a preventive inspection of the workplaces was performed in order to gather the data needed for the assessment and to choose the sampling sites.

2.4.2 PLANNING OF MONITORING ACTIVITIES

Monitoring activities were carried out over a two-year investigation period. The first phase consisted of an intensive measurement campaign involving the only worker responsible for handling gallium arsenide (GaAs) using the Molecular Beam Epitaxy (MBE) system. This initial session focused on collecting detailed environmental and personal exposure data to assess potential contamination risks associated with GaAs manipulation.

Following the results of the first monitoring session, which revealed notable contamination levels, a series of improvement actions were implemented. These included targeted training for personnel on proper hygiene practices and the correct use of personal protective equipment (PPE). The goal was to reduce exposure risks and enhance workplace safety protocols.

After these corrective measures were put in place, a second monitoring phase was launched. This phase involved three operators and extended over a period of three months. It included both environmental and personal exposure assessments, followed by a one-month biomonitoring campaign focused on analyzing urinary arsenic levels in the involved personnel. This comprehensive approach allowed for a comparative evaluation of exposure before and after the implementation of safety improvements.

2.4.3 AIR AND SURFACE MONITORING AND PERSONAL SAMPLING

To evaluate potential GaAs contamination in the laboratory environment and to determine both dermal and airborne exposure levels, a sampling campaign was conducted. The initial monitoring involved one researcher and took place over a five-day period, from Monday to Friday, in June 2023. A more comprehensive monitoring campaign was subsequently carried out between April and June 2024.

2.4.4 AIR SAMPLING

Personal airborne exposure assessment (figure 2) was performed by using:

- a miniature diffusion size classifier (DiSCMini, Matter Aerosol) (Fierz et al. 2011) clipped near the worker's breathing zone in order to measure the number concentration , mean diameter of particles and LDSA (lung deposited surface area) in the range 10-300 nm. The flow rate and the sampling time interval were 1 L/min and 1 second, respectively;
- a IOM sampler mounting a 0,8 µm MCE filter, attached to a personal sampling pump operating at 2 L/min and clipped near the worker's breathing zone (Hanlon et al. 2021). The IOM sampler houses a reusable 25 mm filter cassette that holds a specified filter for the collection of GaAs inhalable particles.

The samplings were carried out both within the MBE laboratory and in the offices of the facility, which were considered as a blank-comparison. Additional background measurements were conducted in the laboratory during a downtime of the MBE system.

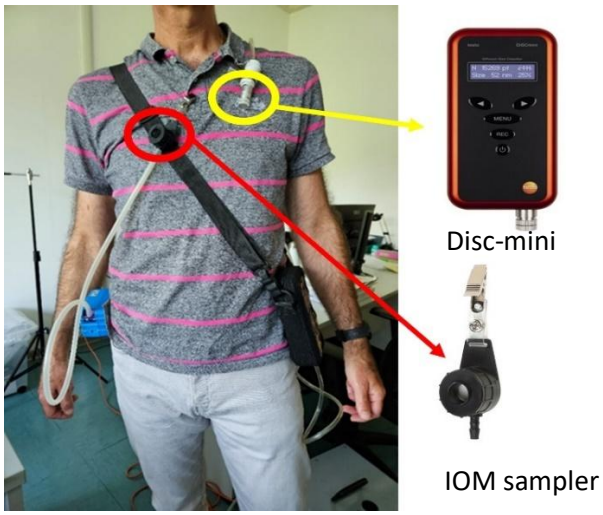

Figure 2: sampler placement on the worker

During the working session, a sampling station with an SKC Sioutas Cascade Impactor sampler (model no. 225-370) (Misra et al. 2002) was placed on a tripod at a height of 170 cm and positioned near the MBE system. The sampler was connected to a pump capable of maintaining a constant flow rate of 9 L/min and the sampling was carried out during the entire duration of the work shift. The SKC Sioutas Cascade Impactor consists of four impactor stages (A, B, C and D) and an after filter that allows the separation and collection of airborne particles in five size ranges according to aerodynamic diameter: >2.5µm (stage A); 2.5-1.0µm (stage B); 1.0-0.5µm (stage C); 0.5-0.25µm (stage D); < 0.25µm (after filter). Particles above each cut-off point are collected on a 25mm filter in the appropriate stage. Particles below the 0.25 µm cut-off point of the last stage are collected on a 37 mm filter. The filters used were of the MCE type (0,8 µm porosity).

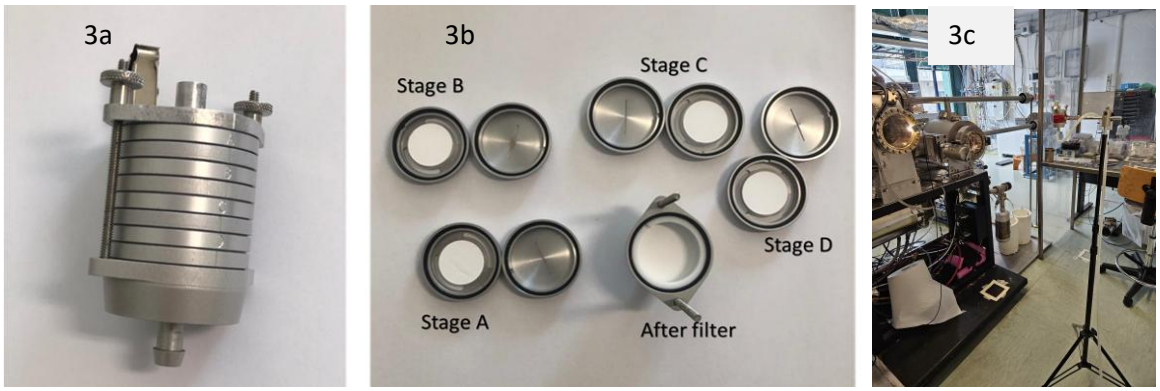

Figure 3: SKC Sioutas Cascade Impactor (3a: sampling head; 3b: sampler disassembled into stages ; 3c: placement of the sampler in the laboratory)

2.4.5 SURFACE SAMPLING

Surface sampling was performed using wipe samples (figure 4) and carbon tabs (figure 5). Wipe samples were taken during first and second monitoring session, while carbon tabs were taken only after implementation of improvement actions. Samples were performed on different surfaces of the laboratory in order to assess any surface contamination. Wiping technique permits to remove contaminants from the surfaces by swiping it through a swab soaked with a solvent ('Sampling and Analytical Methods | Occupational Safety and Health Administration', n.d.). Wipe samples of surfaces were performed by using GhostTM Wipes, on 10cm x 10cm surfaces on 18 points of the laboratory. Samples were performed on Monday morning before starting work and on Monday afternoon at the end of the work shift, in order to determine any daily deposition. Another session of sampling was performed on Friday afternoon in order to assess the cumulative week deposition of GaAs. Nine additional samples were taken on non-standardizable laboratory surfaces (e.g. handles, knobs, etc.). For blank-comparison 18 other points were selected in the offices of the facility.

Carbon tabs, also known as carbon adhesive or conductive tabs, are double-sided, carbon-based adhesive discs specifically designed for sample mounting in Scanning Electron Microscopy (SEM). Carbon tabs were applied to selected surfaces as passive sampling substrates to collect airborne nanoparticle deposits, enabling subsequent morphological and chemical characterization via

techniques such as Scanning Electron Microscopy (SEM) and Energy Dispersive X-ray Spectroscopy (EDS).

Figure 4: wipe samples 10x10 cm frame, ghost wipe and sample vial

Figure 5: carbon tabs

2.4.6 BIOLOGICAL MONITORING

Biomonitoring of GaAs exposure, particularly through urine analysis, is a critical method for assessing internal dose and potential toxicological effects in occupational and environmental settings.

Urinary biomonitoring focuses on detecting arsenic species, as gallium is typically excreted in minimal amounts (Chen 2007). When GaAs is inhaled or absorbed, it can dissociate in the body, releasing arsenic, which is then metabolized and excreted primarily via urine. The presence of inorganic arsenic and its metabolites—monomethylarsonic acid (MMA) and dimethylarsinic acid (DMA)—serves as a biomarker of exposure.

Biological monitoring for arsenic in urine was also carried out during the week of investigation, with samples being taken in the morning before the work shift and in the evening at the end of the working day. A questionnaire was also administered to assess possible non-occupational exposure to arsenic (annex I).

2.4.7 SKIN SAMPLING

To assess potential dermal exposure to gallium arsenide (GaAs) particles, a tape stripping protocol was implemented using D-Squame® adhesive discs (CuDerm, Dallas, TX).

This method is widely recognized for its non-invasive ability to sample the stratum corneum (SC)—the outermost layer of the skin—where contaminants may accumulate following occupational exposure. Sampling was conducted on the volar surface of the right wrist, a site commonly exposed during laboratory activities. The procedure was performed both before and after the work shift, allowing for the evaluation of any increase in surface contamination attributable to work-related tasks.

To ensure consistency and reproducibility, a standardized pressure applicator (D-Squame Pressure Instrument, CuDerm) was used to apply uniform pressure during each tape application. This approach aligns with established guidelines for tape stripping in occupational and dermatological research, as described by Keurentjes, Jakasa, and Kezic (2021)(Keurentjes et al. 2021).

Figure 6: Skin sampling using using D-Squame® adhesive discs (CuDerm, Dallas, TX)

2.4.8 CHEMICAL ANALYSIS

The filters, wipes, and urine samples were acid-digested in a closed microwave system (MultiwavePRO, Anton Paar). The reaction mixtures in the Teflon vessels were: 2.5 mL of HNO3 67-69% (VWR, Normapur) and 1.0 mL of MilliQ water for the filters, and 5 mL of HNO_3 and 1.0 mL of MilliQ water for

the wipes. For urine, 2 mL of the sample was treated with 1 mL of concentrated nitric acid and 1 mL of MilliQ water, and then digested. Three filters and three unexposed wipes were used to prepare the blank samples. The reaction mixture was then heated at 180°C for 45 min. After digestion, the solutions were diluted to a final volume of 25 mL for subsequent analyses.

The tapes were soaked in concentrated nitric acid overnight and then diluted with Milli-Q water.

The solutions obtained from acid digestion, diluted if necessary, were analyzed using a inductively coupled plasma-mass spectrometer (ICP-MS) NexION 350x equipped with an ESI SC Autosampler (Perkin Elmer, Waltham, MA, USA). Instrument calibration was performed using standard solutions (concentration range 0.5-100 µg/L) obtained by diluting a 10 mg/L multi-standard solution for ICP analyses (Periodic Table MIX 1, Sigma-Aldrich). The analysis was carried out in KED mode (Kinetic Energy Discrimination (KED) mode to avoid and minimize cell-formed polyatomic ion interference. The LOD (Limits of Detection) for the two elements were: As (75 a.m.u.) 0.002 µg/L; Ga (69 a.m.u.) 0.002 µg/L. The precision of the analysis, expressed as RSD (%), was < 3%.

Instrument performance and matrix effects were assessed by analyzing laboratory-fortified blanks and laboratory-fortified samples. Depending on the concentration of the elements in the original sample, 1 µg/L and 10 µg/L of As and Ga were added to the original sample. The recoveries of Ga and As were always > 95%, indicating a negligible matrix effect.

2.4.9 DATA ANALYSIS

Data were collected using Excel for Windows and analyzed using STATA-17 (StataCorp College Station, Texas) and the Mann-Whitney test was used to compare data obtained. For statistical comparison, we considered values below the LOD to be LOD/2. Statistical significance was set at p test < 0.05.

2.4.10 ETHICS

The study was approved by the Comitato Etico Unico Regionale (CEUR) Friuli Venezia Giulia and is a part of the periodical medical surveillance for workers exposed to toxic substances for the Italian Law 81/2008. The participating worker signed an informed consent form.

2.5 RESULTS

2.5.1 FIRST SESSION OF MONITORING CAMPAIGN

The initial phase involved a comprehensive measurement campaign focused on the sole operator responsible for handling gallium arsenide (GaAs) within the Molecular Beam Epitaxy (MBE) system. This phase was dedicated to acquiring detailed environmental and personal exposure data to evaluate potential contamination risks associated with GaAs processing activities

2.5.1.1 AIR SAMPLING

Results of air monitoring with DiSCMini are summarize in figures 7 and 8 and detailed in table 1 with distribution of particles (numbers, sizes and LDSA) in offices, in laboratory with active and inactive MBE system. Sampling was conducted from Monday to Friday, with airborne nanoparticle concentrations measured continuously from the beginning to the end of each work shift, for a total monitoring duration of 36 hours and 6 overall IOM samples.

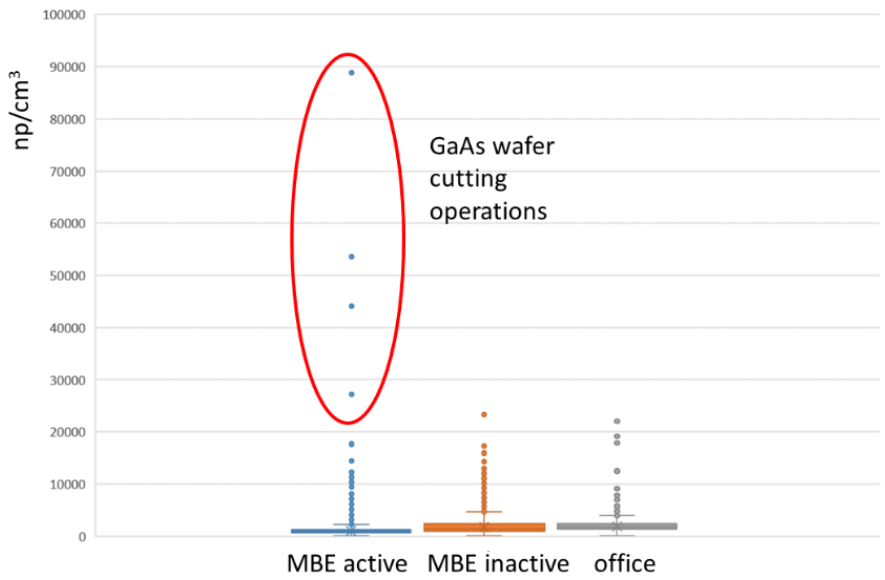

Figure 7: boxplot representing concentration of nanoparticles detected in the laboratory with MBE active, MBE inactive and in the office expressed as number of np/cm³

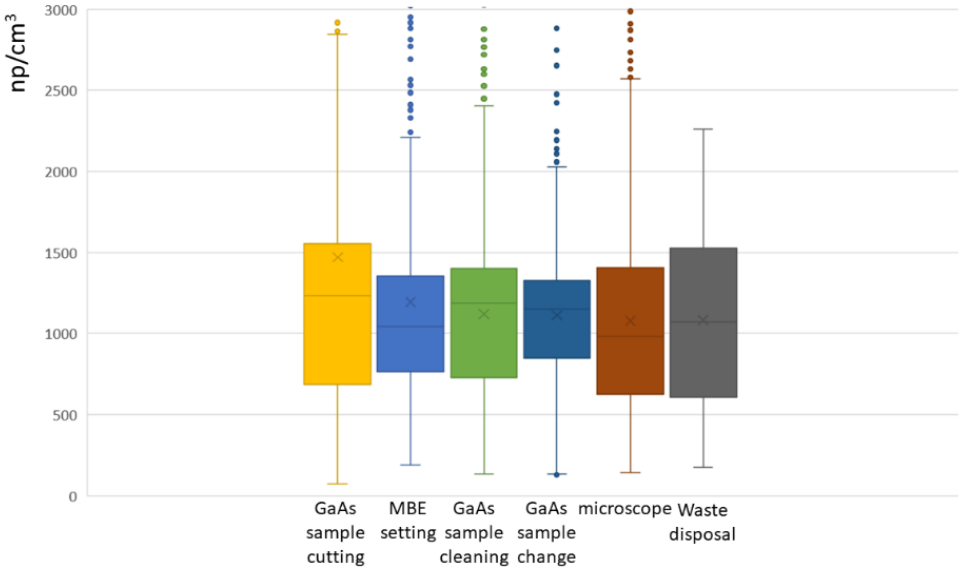

Figure 8: boxplot representing concentration of nanoparticles (np/cm³) detected in MBE laboratory during different operations on GaAs samples

Table 1: concentration (Np/cm^3), size (nm) and LDSA (µm^2/cm^3) of nanoparticles detected with DISCmini personal sampling

	Concentration - np/cm³						
	Mean	**St. dev.**	**Max**	**Min**	**Median**	**I quartile**	**III quartile**
MBE laboratory – overall	1045	889	88883	32	913	653	1310
cutting GaAs samples under a hood	1471	2979	88883	73	1236	686	1554
opening of GaAs sample cabinet	1337	270	2216	776	1316	1164	1507
setting up MBE GaAs system	119	74	10922	190	1042	763	1353
cleaning GaAs samples under a hood	1121	596	8504	134	1187	727	1400
GaAs sample change with load lock open	1114	388	3994	128	1150	849	1325
disposal of waste GaAs	1083	503	2262	176	1073	614	1524
observation of GaAs samples under a microscope	1401	612	6638	1520	1373	1194	1520
desk computer control system MBE	955	582	15233	32	796	595	1227
handling GaAs samples under a hood	818	261	3958	134	783	681	887
MBE laboratory – background measurements with inactive laboratory	1734	1082	23340	121	1450		
Office	1901	678.3	21983	89	1826	1447	2447

	Size - nm						
	Mean	**St. dev.**	**Max**	**Min**	**Median**	**I quartile**	**III quartile**
MBE laboratory – overall	63.2	25.7	300	0	60.1	50.3	76,6
cutting GaAs samples under a hood	54.2	21.5	269.3	0	53.1	47.1	61.9
opening of GaAs sample cabinet	53.2	7	71.2	38.8	52.8	48	57.2
setting up MBE GaAs system	72.4	22.3	300	0	68.5	56.6	84.4
cleaning GaAs samples under a hood	63.8	29.6	220.4	0	54.6	48.8	74
GaAs sample change with load lock open	65.6	23.5	187.5	0	56.3	50.7	76.3
disposal of waste GaAs	64.2	32.2	300	0	55.9	48.5	74.6
observation of GaAs samples under a microscope	52.6	19.5	192	51.5	52.6	44.3	51.5
desk computer control system MBE	65.4	28.7	300	0	63.8	51.4	81.9
handling GaAs samples under a hood	82.3	17.7	172.4	0	81.5	73.2	90.3
MBE laboratory – background measurements with inactive laboratory	74.6	25.8	300	0	68.6		
Office	76.2	13.1	300	0	72.8	68.1	83.8
	LDSA- $\mu m^2/cm^3$						
	Mean	**St. dev.**	**Max**	**Min**	**Median**	**I quartile**	**III quartile**
MBE laboratory – overall	3.6	1.2	40.8	0.4	3.6	3	4.1
cutting GaAs samples under a hood	4	2.5	40.8	1.5	3.9	2.6	4.3
opening of GaAs sample cabinet	4	0.3	4.9	3.3	4	3.72	4.16
setting up MBE GaAs system	4.5	1.9	14	2.6	4.1	3.8	4.4
cleaning GaAs samples under a hood	3.7	0.5	7.4	1.8	3.7	3.37	3.97
GaAs sample change with load lock open	3.8	0.4	7.1	2.7	3.8	3.55	4.05
disposal of waste GaAs	3.5	0.8	6.3	2.1	3.9	2.8	4.2
observation of GaAs samples under a microscope	3.7	0.5	7.4	3.9	3.7	3.4	3.9
desk computer control system MBE	3.4	1	11	0.4	3.5	2.9	4.2
handling GaAs samples under a hood	3.8	0.3	5.7	2.8	3.8	3.7	4
MBE laboratory – background measurements with inactive laboratory	6.8	3.4	28.6	1.2	5		
Office	8.3	2.3	26	0.1	9	6.16	10.4

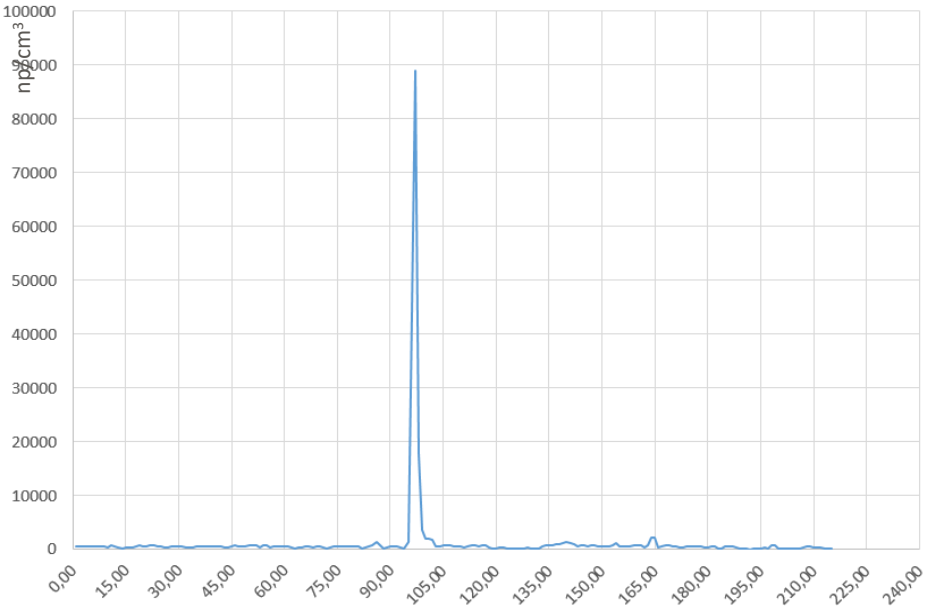

Figure 9: spike in airborne nanoparticle concentration (np/cm^3) detected during GaAs sample cut

Figure 7 and 8 detail nanoparticles levels in areas of the laboratory during different work tasks. In general, the average number of nanoparticles detected during laboratory activities (1045 np/cm^3) was lower than that found during the downtime period (1734 np/cm^3) and the background measurements in the offices (1901 np/cm^3). During laboratory operations, highest values of nanoparticles were detected while cutting of GaAs samples under fume hood (88883 np/cm^3; figure 9). The average nanoparticle size was smaller in the laboratory with MBE active (63.2 nm) than during standstill (74.6 nm) and compared to background office measurements (76.2 nm). Similarly, the LDSA values measured with the MBE system running were lower (3.6 µm^2/cm^3) than with the MBE off (6.8 µm^2/cm^3) or in the offices (8.3 µm^2/cm^3) (table 1).

Personal daily monitoring using an IOM sampler from Monday to Friday (table 2) showed average values of Ga (118.1 ng/m^3) and As (44.6 ng/m^3) that were higher than the comparative measurements carried out in the office, where the values were below the instrumental detection threshold ($p < 0.05$). Moreover, we found different concentration of Ga and As during the week, according to different procedures performed, higher when samples cutting were performed.

Environmental monitoring using SKCSioutas Cascade Impactor permitted to evaluate metal particles distribution according different sizes (table 2) showing very low levels of Ga while As concentrations were often below the instrumental detection threshold limits. Considering only nanoparticles sizes (after filter) Ga was detectable on 4 days per week while As was detectable only on Tuesday, when personal monitoring were higher. To note that Ga concentrations are higher than As because it is used for the adhesion of GaAs wafers in the sample holders.

Table 2: Ga and As concentration (ng/m^3) detected with IOM personal samples and environmental monitoring with Sioutsas Impactor

	IOM personal samples		Environmental monitoring									
			Gallium (ng/m^3)					Arsenic (ng/m^3)				
	Gallium (ng/m^3)	Arsenic (ng/m^3)	Stage A >2.5µm	Stage B 2.5-1.0 µm	Stage C 1.0-0.5 µm	Stage D 0.5-0.25 µm	After filter	Stage A >2.5µm	Stage B 2.5-1.0 µm	Stage C 1.0-0.5 µm	Stage D 0.5-0.25 µm	After filter
Background office	2.54	<0.01	0.11	0.11	0.33	0.11	<0.01	<0.01	<0.01	<0.01	<0.01	<0.01
MBE inactive			0.08	0.07	0.02	0.03	0.05	<0.01	<0.01	<0.01	<0.01	0.07
Monday	4.36	<0.01	0.38	0.21	0.17	0.19	<0.01	0.57	0.24	<0.01	<0.01	<0.01
Tuesday	373.95	147.57	0.49	0.36	0.54	0.28	0.82	<0.01	<0.01	<0.01	<0.01	0.18
Wednesday	18.97	<0.01	0.25	0.31	0.09	0.31	1.25	<0.01	<0.01	<0.01	<0.01	<0.01
Thursday	80.48	37.97	1.56	0.23	0.47	0.47	1.31	<0.01	<0.01	<0.01	<0.01	<0.01
Friday	112.59	37.35	0.31	1.40	0.48	0.29	0.44	0.27	<0.01	<0.01	<0.01	<0.01
Weekly average	118.07	44.58	0.60	0.50	0.35	0.31	0.76	0.19	0.05	<0.01	<0.01	0.04

2.5.1.2 SURFACE SAMPLING

Wipe samples of surfaces were performed by using GhostTM Wipes, on 10cm x 10cm surfaces on 18 points of the laboratory (figure 10).

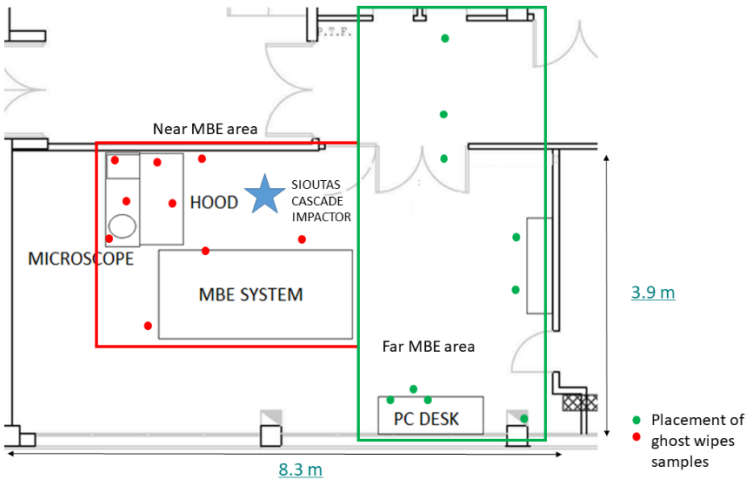

Figure 10: sites of ghost wipe samplings

Table 3: reports Ga and As concentration on surfaces in the MBE laboratory and in the office and figure 11 summarizes data as box-plot in different lab areas.

	Sampling site	**Ga Monday morning**	**Ga Monday afternoon**	**Ga Friday afternoon**	**As Monday morning**	**As Monday afternoon**	**As Friday afternoon**
Mean ± standard deviation (ng/cm²)	FFP3 mask			208			57.8
	MBE surfaces	5.27	85.1	52.9 ± (40.2)	2.38	43.0	21.5 ± (15.3)
	external corridor	27.2 ± (38.0)	4.96 ± (5.94)	6.56 ± (2.62)	46.7 ± (66.0)	2.97 ± (3.71)	1.63 ± (1.33)
	Hood	388 ± (538)	1246 ± (1459)	728 ± (484)	175 ± (212)	682 ± (768)	239 ± (295)
	laboratory cabinets	2.97 ± (3.90)	15.4 ± (17.6)	91.1 ± (205)	0.341 ± (0.236)	1.21 ± (0.543)	27.9 ± (64.5)
	laboratory floor	138 ± (280)	687 ± (1306)	135 ± (229)	31.3 ± (42.0)	118 ± (114)	60.5 ± (108)
	laboratory pc workstation	0.177	1.73	29.7 ± (37.1)	0.173	0.963	4.84 ± (5.87)
	microscope	49.8	135	136 ± (154)	81.5	115	27.3 ± (0.06)
	background office	1,36 ± (1,23)			0,51 ± (0,39)		

Maximum (ng/cm²)	FFP3 mask			208			57.8
	MBE surfaces	5.27	85.1	103	2.38	43.0	44.2
	external corridor	54.1	9.16	8.42	93.3	5.59	2.57
	Hood	1172	3308	1171	433	1418	627
	laboratory cabinets	8.55	39.2	553	0.693	1.93	174
	laboratory floor	638	3014	536	100	241	251
	laboratory pc workstation	0.177	1.73	55.9	0.173	0.963	8.99
	microscope	49.8	135	244	81.5	115	27.4
	background office	3,74			1,44		
Minimum (ng/cm²)	FFP3 mask			208			57.8
	MBE surfaces	5.27	85.1	10.5	2.38	43.0	12.3
	external corridor	0.34	0.76	4.71	0.04	0.35	0.69
	Hood	5.01	94.6	247	1.62	11.8	3.83
	laboratory cabinets	0.11	1.90	0.18	0.19	0.64	0.27
	laboratory floor	0.30	1.77	1.66	0.44	1.93	0.16
	laboratory pc workstation	0.18	1.73	3.52	0.17	0.96	0.69
	microscope	49.8	135	26.9	81.5	115	27.3
	background office	0.04			0.04		

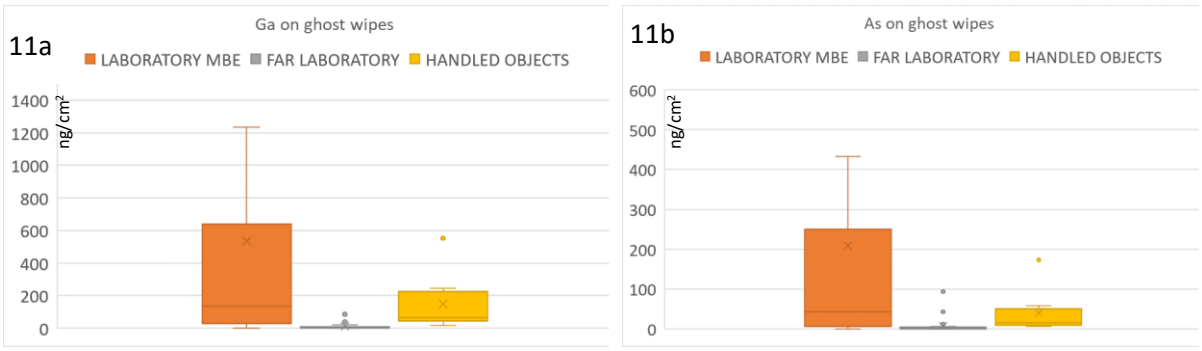

Figure 11: boxplot representing Ga (11a) and As (11b) concentration (ng/cm²) on ghost wipes collected on different areas of the laboratory (n. 81 samples)

The highest contamination values were found on the inner surfaces of the hood (Ga max = 3308 ng/cm²; As max = 1418 ng/cm²) and on the laboratory floor (Ga max = 3014 ng/cm²; As max = 251 ng/cm²). In particular, the highest floor contaminations were located under the hood and in correspondence with the load lock of the MBE system. On the MBE system surfaces, the highest contamination levels were found on Friday afternoon (Ga max = 103 ng/cm²; As max=44.2 ng/cm²) on the system knobs. Similarly, on the laboratory cabinets surfaces, the highest concentration of Ga (553 ng/cm²) and As (174 ng/cm²) were found on Friday afternoon inside of the cabinet handles. Also on the pc workstation the highest contamination levels were found on Friday afternoon (Ga max = 55.9 ng/cm²; As max = 8.9 ng/cm²). On the microscope the highest concentration of Ga was found on Friday afternoon (244 ng/cm²) whereas the maximum contamination of As was assessed on Monday afternoon (135 ng/cm²). At the end of the week, a sample was taken on the surfaces of the FFP3 mask, detecting 208 ng/cm² of Ga and 57.8 ng/cm² of As. Significantly lower ($p < 0.01$) levels of Ga (average 1.36 ng/cm²) and As (average 0.51 ng/cm²) were found in offices located in another area of the building. A contamination of Ga (3.63 ng/cm²) and As (1.44 ng/cm²) was detected also on the floor under the desk used by the MBE operator outside the lab, showing a possible shoes contamination, despite the adhesive mat used to avoid diffusion of particles outside the lab.

2.5.1.3 SKIN SAMPLING

Skin samples were collected from the volar surface of the worker's wrist at the beginning and end of each work cycle, from Monday to Friday, for a total of 10 samples collected. The skin samples collected with the tape stripping technique showed concentrations of Ga and As (table 4) which were on average higher at the end of the shift than in the morning ($p < 0.05$).

*Table 4: Ga and As concentration (ng/cm²) on tape stripping collected in the morning and after work shift everyday *p < 0.05 Mann-Whitney test between morning and afternoon*

	Group	Mean	Afternoon/ morning	Median	25° percentiles	75° percentiles	Minimum	Maximum
Ga (ng/cm²)	afternoon	119.02*	12.1	69.81	42	130	20.2	333.2
	morning	9.83		6.17	5.2	11.4	4.2	22.2
	daily overall	64.4		21.2	7.5	62.9	4.2	333.2
As (ng/cm²)	afternoon	3.36*	14.6	2.25	2.22	3.48	0.07	8.8
	morning	0.23		0.165	0.04	0.36	0.02	0.6
	daily overall	1.8		0.5	0.1	2.2	0.02	8.8

In particular, the average afternoon concentrations of Ga (119.02 ng/cm²) were found to be twelve times higher than the morning values, while the average afternoon levels of As (3.36 ng/cm²) were found to be more than fourteen times higher than those before the start of the work shift (figure 12).

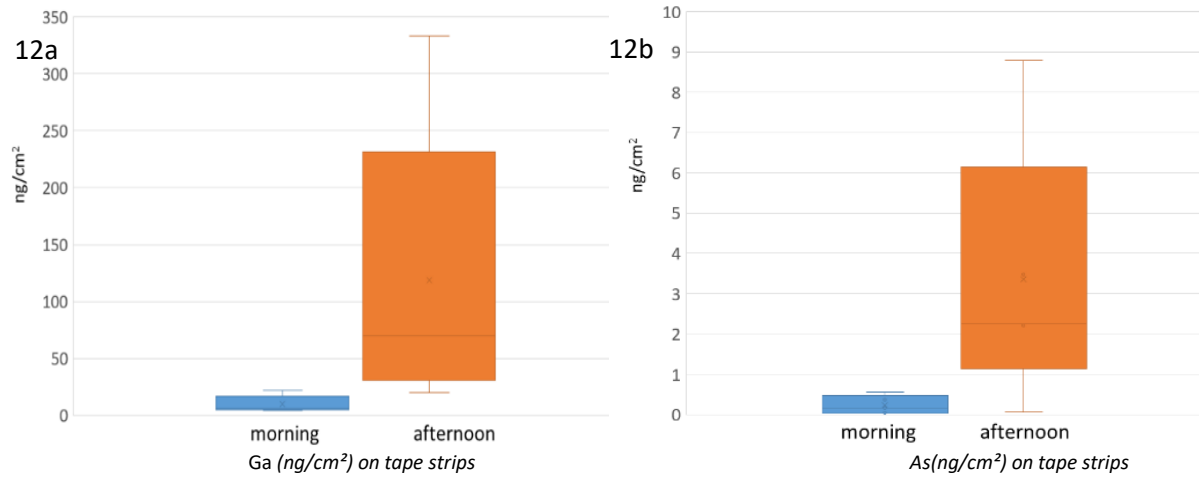

Figure 12: boxplot representing Ga (12a) and As (12b) concentration (ng/cm²) on tape stripping collected on the volar part of the right wrist of the worker in the morning, before work-shift, and in the afternoon, at the end of the work-shift (n. 10 samples)

2.5.1.4 BIOLOGICAL MONITORING

During a five-day monitoring campaign (Monday–Friday), pre-shift and post-shift urine samples were systematically collected from the exposed worker to assess occupational exposure. The concentration of Ga and As content in urine of operator is reported in figure n. 13, showing very low level of Ga and significant amount of As. The weekly average of Ga and As was 0.49 µg/L and 19.5 µg/L, respectively. As average concentration was above the SIVR (Società Italiana Valori di Riferimento) reference limit for non-occupational population (2.0 – 15 µg/L), but below the limit for occupational exposure to As (ACGIH - Biological Exposure Index 30 µg/L).

The worker was a non-smoker and in the period prior to the investigation had not consumed significant quantities of foods considered a source of As. His kidney function resulted normal (creatinine, urea, uric acid in blood and urine analysis) as well as blood pressure and medical examination).

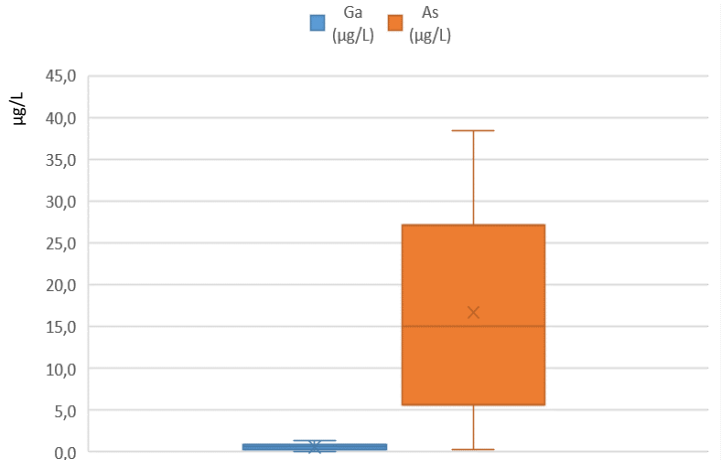

Figure 13: boxplot of Ga and As concentration expressed as µg/L in urine

2.6 DISCUSSION OF THE FIRST PART OF MONITORING ACTIVITIES

During the synthesis of nanostructured gallium arsenide (GaAs) using the Molecular Beam Epitaxy (MBE) system, a comprehensive occupational exposure assessment was conducted to evaluate potential risks associated with airborne nanoparticles, surface contamination, and biological uptake. Real-time monitoring with the DISCmini instrument revealed that the average particle number concentration (PNC) during laboratory operations was 1045.3 particles/cm³, notably lower than the values recorded during system downtime (1734.4 particles/cm³) and in the office environment (1901 particles/cm³). This suggests that the laboratory's general and local ventilation systems, including fume hoods and HEPA filtration, are effective in maintaining low background nanoparticle levels during routine activities. However, significant transient peaks in PNC were observed during the mechanical cutting of GaAs wafers, with concentrations reaching up to 88883 particles/cm³. These peaks are attributed to the generation of ultrafine particles through mechanical abrasion. Despite being performed under a ventilated fume hood, which effectively confined and rapidly reduced airborne concentrations, these operations represent a critical moment of potential inhalation exposure.

Environmental sampling using an IOM sampler confirmed the presence of GaAs-derived particles in the air, with weekly average concentrations of gallium at 118.07 ng/m³ and arsenic at 44.58 ng/m³. These levels were above the detection threshold, unlike the comparative office samples, which remained below instrumental limits.

Occupational exposure to inorganic arsenic was evaluated following the statistical strategy outlined in UNI EN 689:2019. The personal sampling data exhibited a right-skewed lognormal distribution characteristic of industrial hygiene measurements, with concentrations ranging from <0.01 ng/m³ to a maximum of 147.57 ng/m³. Descriptive statistics indicated a mean concentration of 44.78 ng/m³ and a standard deviation of 50.36 ng/m³, reflecting substantial daily variability. However, all measured values remained negligible relative to the Occupational Exposure Limit (OEL) of 0.01 mg/m³ (10,000

ng/m³). Notably, the 95th percentile (147.57 ng/m³), which serves as the primary compliance metric under the standard, corresponded to less than 1.5% of the OEL.

Surface contamination was assessed using ghost wipe sampling, which revealed localized deposition of gallium and arsenic on various laboratory surfaces. The highest contamination levels were found inside the fume hood (Ga: 3308 ng/cm²; As: 1418 ng/cm²) and on the floor beneath the hood and near the MBE load lock (Ga: 3014 ng/cm²; As: 251 ng/cm²). Additional contamination was detected on the MBE system knobs (Ga: 103 ng/cm²; As: 44.2 ng/cm²), cabinet handles (Ga: 553 ng/cm²; As: 174 ng/cm²), and microscope surfaces, with gallium peaking on Friday (244 ng/cm²) and arsenic on Monday (135 ng/cm²). These results indicate accumulation of contaminants throughout the week, likely due to repeated handling and insufficient cleaning protocols. The presence of gallium (208 ng/cm²) and arsenic (57.8 ng/cm²) on the surface of the FFP3 mask at the end of the week further confirms external deposition and highlights the importance of proper PPE management and disposal.

Dermal exposure was evaluated using the tape stripping technique, which showed that gallium and arsenic concentrations on the skin were significantly higher at the end of the work shift compared to the beginning. Afternoon gallium levels averaged 119.02 ng/cm²—twelve times higher than morning values—while arsenic levels averaged 3.36 ng/cm², more than fourteen times higher than pre-shift levels. These findings suggest that despite the use of nitrile gloves and protective clothing, there is a measurable risk of skin contamination, likely due to contact with contaminated surfaces or particle resuspension.

Biological monitoring further supported the environmental findings. Weekly urinary analysis showed average gallium concentrations of 0.49 µg/L, below the detection threshold, while arsenic levels averaged 19.5 µg/L. This arsenic concentration exceeded the SIVR reference range for the general population (2.0–15 µg/L) but remained below the ACGIH Biological Exposure Index (30 µg/L) for occupational settings.

Overall, the synthesis of nano-GaAs via MBE was associated with measurable occupational exposure risks, particularly during cutting operations. The data confirmed the potential for inhalation exposure

to GaAs nanoparticles, surface contamination in key laboratory areas, and dermal absorption by the worker. Although arsenic levels detected in urine were below the ACGIH Biological Exposure Index, the findings nonetheless highlighted the need to implement enhanced protective measures.

2.7 IMPLEMENTATION OF IMPROVEMENT ACTIONS

Following the initial environmental and personal exposure monitoring campaign, a comprehensive set of corrective and preventive actions was implemented to strengthen occupational safety protocols related to the handling of gallium arsenide (GaAs) nanoparticles. These actions included targeted awareness and training sessions aimed at reinforcing the understanding and correct application of preventive and protective measures among laboratory personnel. The sessions involved the operator initially monitored, as well as two newly recruited researchers who joined the project team.

A revised and rigorously enforced protocol was implemented to guarantee the systematic use of personal protective equipment (PPE) during all procedures involving GaAs. This includes the use of disposable polypropylene lab coats, head covers, nitrile gloves, and FFP3-class filtering facepiece respirators. The consistent and correct use of PPE is critical in minimizing dermal and respiratory exposure to GaAs.

To ensure the integrity and hygiene of protective equipment, all PPE were stored in sealed cabinets located outside the laboratory environment. This measure prevents cross-contamination and ensures that clean equipment is used at the beginning of each shift. Furthermore, access to and exit from the laboratory were controlled through adhesive decontamination mats, which serve to capture particulate matter from footwear and reduce the risk of nanoparticle dispersion beyond the controlled area.

During GaAs manipulation—particularly cutting operations conducted under a certified fume hood—disposable absorbent sheets were employed to contain particulate emissions at the source. This localized containment strategy is essential in preventing the spread of GaAs dust to surrounding

surfaces and equipment. The cleaning protocol was also significantly reinforced. Systematic surface decontamination was carried out at the end of each work shift using appropriate cleaning agents and procedures designed for nanoparticle removal. In addition, a deep-cleaning operation was scheduled weekly, typically over the weekend, to ensure the thorough removal of any residual contaminants. These cleaning activities are vital in maintaining a safe working environment and in preventing the accumulation of hazardous materials over time.

The combination of strict PPE usage, controlled laboratory access, localized containment measures, and rigorous cleaning protocols represents a multi-barrier approach to risk mitigation. This integrated strategy is essential for ensuring the health and safety of personnel working with nanomaterials such as GaAs, and for maintaining compliance with best practices in occupational hygiene and nanomaterial safety.

2.7.1 SECOND SESSION OF MONITORING CAMPAIGN

The second measurement campaign involved three laboratory operators and was conducted with the primary objective of evaluating the effectiveness of the improvement measures previously implemented. This phase aimed to verify whether the enhanced safety protocols—particularly those related to personal protective equipment (PPE) usage, contamination control, and environmental hygiene—resulted in a measurable reduction in potential exposure to gallium arsenide (GaAs) nanoparticles during routine handling and processing activities.

2.7.1.1 AIR SAMPLING

The outcomes of the airborne particle monitoring conducted using the DiSCMini device are presented in Table 5 and in figure 14. These results include the distribution of particles in terms of number concentration, size range, and lung-deposited surface area (LDSA).

Table 5: concentration (Np/cm^3), size (nm) and LDSA (µm^2/cm^3) of nanoparticles detected with DISCmini personal sampling

	Concentration - Np/cm³						
	Mean	**St. dev.**	**Max**	**Min**	**Median**	**I quartile**	**III quartile**
MBE laboratory – overall	1085	716	19019	52	846	593	1464
cutting GaAs samples under a hood	1377	761	10578	84	1153	754	1978
GaAs sample handling	787	456	9649	37	696	511	977
In soldering	6586	45484	801696	89	675	521	1191
external corridor	2616	1620	5867	436	2194	915	4282
magnetotransport laboratory	2212	486	6327	1302	2165	1918	2388
microscope observation	1340	268	1917	885	1364	1201	1457
Office	1258	180	2062	645	1237	1155	1353
other laboratory	466	284	5054	130	431	347	524
	Size - nm						
	Mean	**St. dev.**	**Max**	**Min**	**Median**	**I quartile**	**III quartile**
MBE laboratory – overall	59.6	24.7	268	0.00	56.5	49.6	66.6
cutting GaAs samples under a hood	63.9	19.9	264	0.00	60.4	52.1	73.1
GaAs sample handling	57.7	26.2	300	0.00	62.7	53.6	72.6
In soldering	45.6	24.6	300	0.00	51.1	37.4	58.9
external corridor	52.1	6.19	90.9	37.6	52.0	48.3	54.7
magnetotransport laboratory	42.4	5.13	68.5	23.5	42.2	39.6	45.0
microscope observation	59.4	8.81	76.6	45.0	56.5	54.5	64.8
Office	88.7	10.4	152	59.5	88.1	82.5	93.5
other laboratory	114	40.5	300	0.00	114	97.5	135
	LDSA- µm²/cm³						
	Mean	**St. dev.**	**Max**	**Min**	**Median**	**I quartile**	**III quartile**
MBE laboratory – overall	3.58	1.66	8.72	1.13	3.07	2.20	4.64
cutting GaAs samples under a hood	4.64	1.54	9.52	1.65	4.42	3.37	6.02
GaAs sample handling	3.00	1.10	10.4	0.810	2.63	2.20	3.80
In soldering	6.54	25.3	368	1.57	1.95	1.83	4.17
external corridor	7.66	4.83	14.9	2.15	5.90	2.60	12.9

magnetotransport laboratory	5.06	0.382	7.72	3.96	5.05	4.78	5.25
microscope observation	4.47	0.237	4.81	4.05	4.49	4.37	4.63
Office	6.69	0.297	8.38	5.93	6.65	6.48	6.83
other laboratory	3.23	0.313	8.57	2.47	3.18	3.06	3.34

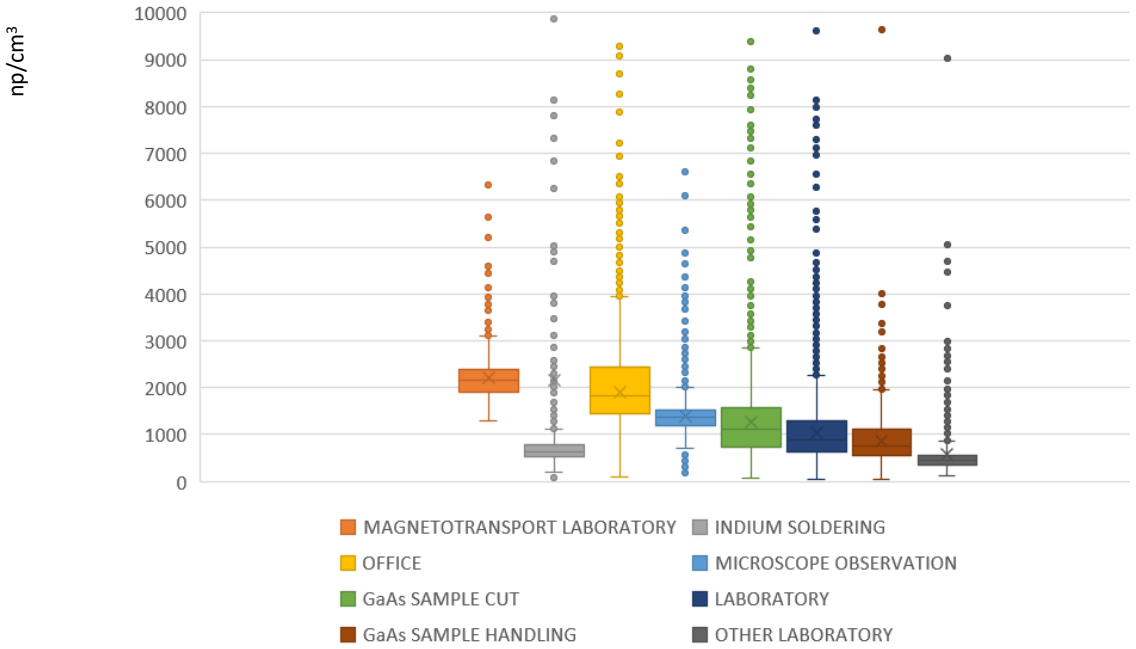

Figure 14: boxplot representing concentration of nanoparticles (np/cm³) detected in MBE laboratory during different operations on GaAs samples after implementation of improvement actions

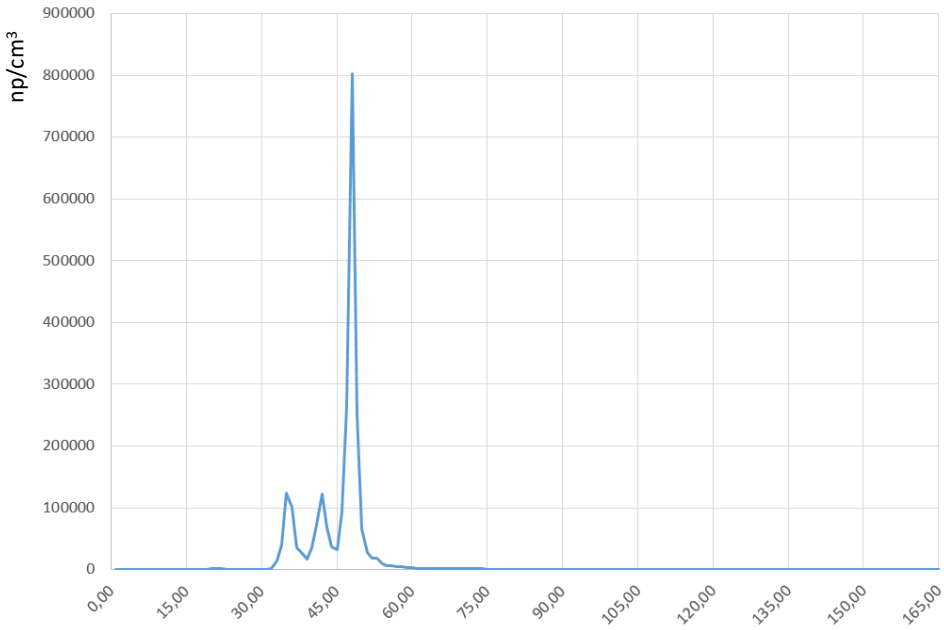

Figure 15: spike in airborne nanoparticle concentration (np/cm3) detected during gallium-based soldering activities

The results of real-time air monitoring using the DISCmini personal sampler confirmed the findings of the previous measurement session, which had indicated generally low average nanoparticle concentrations. In this context, the average concentration of nanoparticles was found to be 1085 Np/cm³. However, additional concentration peaks were observed, some of which were associated with gallium-based soldering activities.

The soldering activity stands out with an exceptionally high mean concentration of 6586 Np/cm³ and a maximum value reaching 801696 Np/cm³ (figure 15). This indicates sporadic but intense particle emissions, with a very high standard deviation suggesting considerable variability and the potential for peak exposure events. In contrast, activities such as microscope observation, office work, and operations in other laboratories show relatively low mean concentrations, ranging from 466 to 1340 Np/cm³, and narrow interquartile ranges, reflecting stable and low exposure levels.

Within the MBE laboratory, the overall mean concentration is moderate at 1085 Np/cm³, but the maximum value of 19019 Np/cm³ suggests occasional spikes, likely during active GaAs manipulation. Cutting GaAs samples under a hood shows elevated mean values and a higher third quartile, confirming that mechanical operations are significant sources of airborne particles. Handling GaAs samples, on the other hand, presents a lower mean concentration and a relatively narrow quartile range, indicating that containment and PPE protocols are effectively reducing exposure during these tasks.

IOM airborne samples were collected during three months of gallium arsenide (GaAs) handling activities performed by three designated operators, amounting to an overall monitoring period of 126 hours, corresponding to 21 samples performed. The concentrations of arsenic (As) and gallium (Ga) detected in the collected samples are summarized in table 6 and figure 16. The average airborne concentration of arsenic was 197.96 ng/m³, with a maximum value of 724.29 ng/m³. For gallium, the average concentration was 177.08 ng/m³, with a peak value of 376.37 ng/m³. Despite some variability, the measured arsenic concentrations remained well below the ACGIH Threshold Limit Value – Time Weighted Average (TLV-TWA) for arsenic, which is set at 0.01 mg/m³ (equivalent to 10000 ng/m³).

Table 6: Ga and As concentrations (ng/mc) detected with IOM personal samples

	As	Ga
	(ng/mc)	(ng/mc)
Average	197.96	177.08
Standard deviation	304.69	124.88
median	71.76	176.48
I quartile	0	100.92
III quartile	193.72	184.22
Max	724.29	376.37

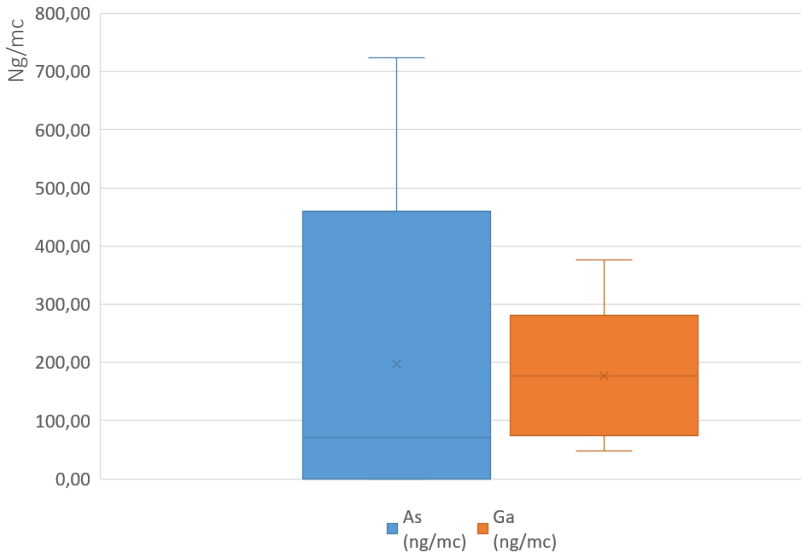

Figure 16: Ga and As concentration (ng/mc) detected with IOM personal samples

SURFACE SAMPLING

Surface wipe sampling was conducted using Ghost™ Wipes on 10 cm × 10 cm areas across four critical zones within the laboratory. These samples were collected over a three-month period during active laboratory operations, for a total of 40 samples collected.

Results are reported in table 7 and in figure 17.

Table 7. Ga and As concentration (ng/cm²) on surfaces in the MBE laboratory comparison before and after improvement actions

	Internal hood worktop			
	As (ng/cm²)		Ga (ng/cm²)	
	Before improvement actions	After improvement actions	Before improvement actions	After improvement actions
average	720.3	636.7	1384.62	619.83
standard deviation	502.23	1177.29	1004.88	1103.71
median	530.31	103.39	1171.22	109.19
I quartile	338.96	100.87	1131.64	91.57
III quartile	1110.83	166.06	1218.86	252.34
	Floor under hood			
	As (ng/cm²)		Ga (ng/cm²)	
	Before improvement actions	After improvement actions	Before improvement actions	After improvement actions
average	194.93	114.72	1395.89	1114.72
standard deviation	82.58	217.13	1401.98	2170.13
median	233.85	171.69	638.12	171.69
I quartile	166.97	73.79	587	73.79
III quartile	242.36	277.78	1825.9	277.78
	Microscope worktop			
	As (ng/cm²)		Ga (ng/cm²)	
	Before improvement actions	After improvement actions	Before improvement actions	After improvement actions
average	74.52	32.05	70.47	30.36
standard deviation	44.08	41.55	56.8	33.7
median	81.47	14.4	49.77	10.16
I quartile	54.42	4.38	38.35	6.13
III quartile	98.09	54.55	92.25	57.09

	Laboratory entrance floor			
	As (ng/cm²)		Ga (ng/cm²)	
	Before improvement actions	After improvement actions	Before improvement actions	After improvement actions
average	9.68	2.89	10	4.47
standard deviation	8.68	1.31	8.73	3.75
median	5.65	2.55	8.13	2.86
I quartile	4.7	2.28	5.24	1.4
III quartile	12.64	2.7	13.82	6.97
	FFP3 Mask			
	As (ng/cm²)		Ga (ng/cm²)	
	Before improvement actions	After improvement actions	Before improvement actions	After improvement actions
average	57.76	1.73	280.07	0.85
standard deviation		1.09		0.7
median		1.24		0.53
I quartile		1.11		0.45
III quartile		2.11		1.09

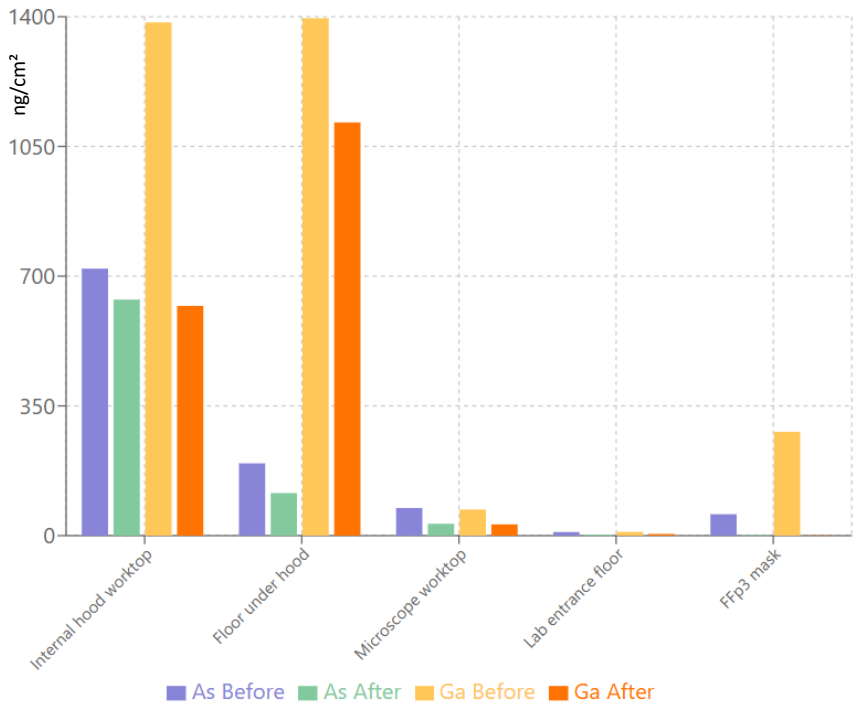

Figure 17: Ga and As surface contamination levels (ng/cm²) detected on different laboratory surfaces before and after implementation of improvement actions

The surface contamination data collected before and after the implementation of improvement actions demonstrates a clear trend in the reduction of arsenic and gallium residues across most critical laboratory areas.

The comparative analysis of surface contamination data between before and after improvement actions reveals a general trend of reduced arsenic and gallium concentrations across most monitored areas, indicating the effectiveness of the implemented improvement measures.

On the internal hood worktop, the median arsenic concentration decreased from 530.31 ng/cm² in 2023 to 103.39 ng/cm² in 2024, while gallium levels dropped more significantly from 1171.22 ng/cm² to 109.19 ng/cm². This reduction, particularly in gallium, suggests that the enhanced cleaning protocols and containment strategies have been effective in minimizing particle deposition on this critical surface.

The floor under the hood also showed a decrease in median arsenic concentration from 233.85 ng/cm² to 171.69 ng/cm² and a decrease in gallium from 638.12 ng/cm² to 171.69 ng/cm². Although the reduction is less pronounced than in other areas, it still reflects a positive impact of the interventions. However, the high variability in the data, as indicated by the standard deviation, suggests that occasional contamination events may still occur and warrant further attention. At the microscope worktop, the median arsenic concentration dropped from 81.47 ng/cm² to 14.4 ng/cm², and gallium from 49.77 ng/cm² to 10.16 ng/cm². These reductions are consistent and substantial, confirming that the area is now better protected from cross-contamination, likely due to improved handling practices and localized cleaning. The lab entrance floor exhibited contamination reduction, with arsenic levels decreasing from 5.65 ng/cm² to 2.55 ng/cm² and gallium from 8.13 ng/cm² to 2.86 ng/cm².

These results highlight the effectiveness of access control measures, such as adhesive mats, in preventing the spread of contaminants beyond the primary work zones.

The FFP3 masks showed the most dramatic reduction in contamination. Arsenic levels dropped from 57.76 ng/cm² to 1.24 ng/cm², and gallium from 280.07 ng/cm² to just 0.53 ng/cm². These values

confirm that the revised PPE protocols and handling procedures have been highly effective in preventing direct exposure to hazardous particles.

During the second monitoring session, surface sampling was also conducted using carbon tab interception samplers.

Inside the laboratory, carbon tabs (PELCO Tabs™ Carbon Conductive Tabs, 6 mm) were applied to the working surfaces, one on the main computer, one on each side of the processing workstation, and one on the microscope desk. The carbon tabs remained in these positions for the total duration of one month of monitoring for a total of 10 carbon tabs. After exposure they were evaluated using Scanning Electron Microscopy (SEM) to detect the presence of particles and nanoparticles of GaAs. All images were acquired using a GEMINI 300 ZEISS high-resolution Field Emission Gun (FEG) SEM equipped with Energy Dispersive X-ray Spectroscopy (EDS) system for compositional analysis.

The SEM-EDS analysis (figure 18) showed the presence of gallium (Ga) and arsenic (As) peaks, confirming the deposition of GaAs nanoparticles on the sampled surfaces. These elements were often accompanied by signals from other materials such as oxygen (O), carbon (C), copper (Cu), and occasionally silver (Ag), zinc (Zn), and lead (Pb), which may originate from the laboratory environment, sample holders, or background contamination.

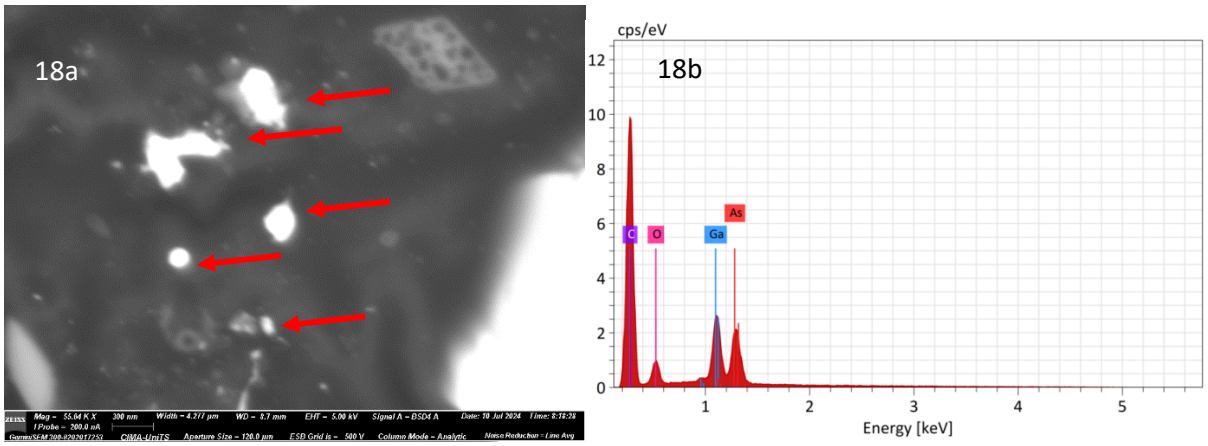

Figure 18: SEM image (18a) (300 nm scale) and chemical composition obtained with EDS analysis (18b) on carbon tabs taken under the hood

2.7.1.2 SKIN SAMPLING

After the implementation of improvement actions, skin sampling was performed on three workers' volar part of right wrist during three months of monitoring campaign, taking samples at the beginning and at the end of the workshift, for a total of 24 samples collected.

After the implementation of improvement actions, both As and Ga concentrations dropped sharply (table 8 and figure 19), particularly after GaAs manipulation, indicating the effectiveness of the control measures.

Quantitatively, the average concentration of arsenic decreased from 3.36 ng/cm² before improvement actions to 0.16 ng/cm² after, representing a reduction of approximately 95%. Similarly, gallium concentrations dropped from 119.02 ng/cm² to 0.21 ng/cm², corresponding to a reduction of over 99.8%.

The statistical distribution supports these findings. Before improvements, arsenic showed a median value of 2.25 ng/cm² and a 75th percentile of 3.48 ng/cm², while gallium had a median of 69.81 ng/cm² and a 75th percentile of 129.79 ng/cm². After improvements, both elements recorded median and interquartile values of 0.00 ng/cm², indicating not only a reduction in average contamination but also a consistent elimination of detectable residues across all sampled surfaces.

These results confirm the effectiveness of the implemented control measures in mitigating nanoparticle contamination during GaAs handling operations.

*Table 8: Ga and As concentration (ng/cm²) on tape stripping collected before and after implementation of improvement actions *p < 0.05 Mann-Whitney test between before and after improvement actions*

	before GaAs manipulation				after GaAs manipulation			
	before improvement actions		after improvement actions		before improvement actions		after improvement actions	
	As (ng/cm²)	Ga (ng/cm²)	As (ng/cm²)	Ga (ng/cm²)	As (ng/cm²)	Ga (ng/cm²)	As (ng/cm²)	Ga (ng/cm²)
average	0.23	9.83	0.21	0.28	3.36*	119.02*	0.16*	0.21*
standard deviation	0.23	7.45	0.57	0.49	3.27	126.61	0.48	0.51
median	0.17	6.17	0	0	2.25	69.81	0	0
I quartile	0.04	5.17	0	0	2.22	42.03	0	0
III quartile	0.37	11.42	0	0.41	3.48	129.79	0	0

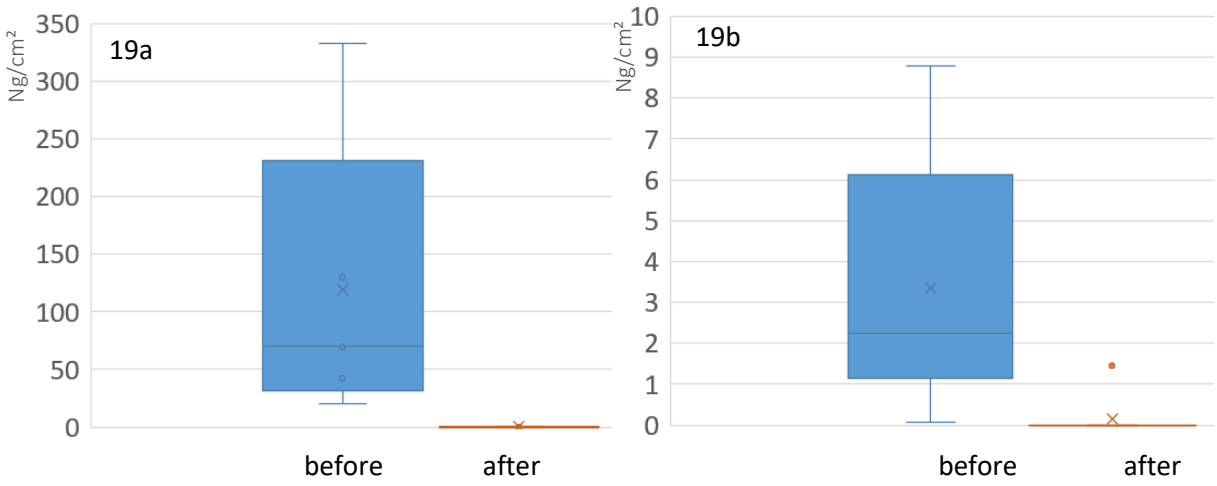

Figure 19: boxplot representing Ga (19a) and As (19b) concentration (ng/cm²) on tape stripping before and after improvement actions

2.8 DISCUSSION OF THE SECOND PART OF MONITORING ACTIVITIES

The implementation of improvement actions in the laboratory setting yielded measurable and technically significant outcomes in terms of contamination control and occupational exposure reduction.

Firstly, the observed general reduction in contamination levels across various laboratory surfaces—including the worktop of the hood and microscope, the floor under the hood, the microscope worktop, and the laboratory entrance floor—indicates that the mitigation strategies were effective in minimizing the spread and deposition of hazardous materials. This is particularly relevant in environments where gallium arsenide (GaAs) is handled, as both gallium (Ga) and arsenic (As) pose health risks through dermal contact and inhalation.

The reduction in Ga and As concentrations on FFP3 masks further supports the effectiveness of the preventive interventions. The significant decrease in skin contamination levels at the end of laboratory activities is a strong indicator of improved personal protective equipment (PPE) protocols and better hygiene practices.

This is crucial, as dermal absorption can be a secondary route of exposure, especially in the presence of nanoparticles. Personal air sampling confirmed the presence of Ga and As during GaAs handling under the hood, but the highest arsenic concentration detected (724.29 ng/m^3) remained well below the threshold limit value-time weighted average (TLV-TWA) of 10,000 ng/m^3. This suggests that while exposure exists, it is currently within acceptable occupational safety limits.

2.9 CONCLUSION

The significant decline in surface and skin contamination levels following the implementation of updated safety protocols highlights the critical importance of a comprehensive and multilayered approach to occupational health management.

This integrated strategy combines engineering controls—such as localized ventilation and containment systems—with administrative measures, including standardized operating protocols, targeted training programs, and systematic exposure monitoring.

In addition to the effectiveness of collective preventive measures—such as chemical fume hoods and hygienic practices—the proper use of personal protective equipment (PPE), specifically tailored to the hazards associated with handling gallium arsenide (GaAs) nanomaterials, represents a crucial element of occupational safety strategies.

Together, these elements form an integrated safety framework that not only meets regulatory requirements but actively reduces risk and promotes a culture of safety within the facility.

The data collected during this period enables the identification of trends, the assessment of protocol efficacy, and the timely adjustment of control measures in response to evolving operational conditions.

Given the potential risks posed by GaAs nanoparticles, maintaining rigorous safety standards is very important.

To this end, continuous real-time monitoring of airborne nanoparticle concentrations is essential for detecting fluctuations and preventing acute and chronic exposures. In parallel, routine assessments of surface contamination and skin exposure should be conducted to ensure that indirect contact pathways are effectively managed.

These monitoring efforts not only safeguard the health of personnel but also contribute to the development of best practices for facilities engaged in the synthesis and handling of GaAs nanomaterials.

3. TRANSDERMAL ABSORPTION OF GALLIUM AND ARSENIC FOLLOWING EXPOSURE TO GAAS PARTICLES: AN EX-VIVO INVESTIGATION USING FRANZ DIFFUSION CELLS

3.1 INTRODUCTION

In order to evaluate the cutaneous permeation of GaAs particles we carried out a research using an ex-vivo model with Franz diffusion cells.

At physiological pH, GaAs separates into Ga and As moieties (Webb et al. 1986b; Flora 2000; Flora et al. 2009) which may penetrate skin.

Skin may absorb metal ions, and sweat's ability to oxidize metals is strongly correlated with the amount of metals absorbed via the skin (Larese et al. 2007; Crosera et al. 2009; Larese Filon et al. 2015; Labouta and Schneider 2013).

Toxicokinetic studies indicate that arsenic can be absorbed through human and animal skin (e.g., 6.4% and 2.0% of applied dose absorbed in Rhesus monkeys, 1.9% absorbed in human skin in vitro), however, the available data are insufficient to adequately evaluate its potential to cause systemic effects following dermal exposure (Dutkiewicz 1977; Wester et al. 1993; Turkall et al. 2003; Lowney et al. 2005; 2007; Marin Villegas and Zagury 2023).

Villegas et al. (Marin Villegas and Zagury 2023) tested As skin permeation from contaminated soil using synthetic skin finding that arsenic was almost exclusively detected as arsenate (As(V)) that cannot permeate the skin.

Ouypornkochagorn et al. (Ouypornkochagorn and Feldmann 2010) showed that penetration and accumulation of arsenic is strongly dependent on its speciation, demonstrating that arsenite, a form of inorganic arsenic, is particularly well-absorbed through the skin.

Li et al. (Li et al. 2024) analyzed skin bioaccessibility of As released by contaminated road dust treated with artificial sweat simulation method (pH=6.5) finding a potential for skin absorption.

The release of As from GaAs is a crucial point to evaluate potential exposure of workers and it is related to the size of GaAs particles.

As the size of particles decreases, particularly reaching the nanoscale, the release of arsenic and its absorption through the skin both increase, with the highest absorption occurring at the nanoparticle level (Larese Filon, Bello, et al. 2016; Brouwer et al. 2016). GaAs NPs with a higher surface area have more contact with the surrounding environment (e.g., fluids, tissues), leading to an increased rate of dissolution in sweat and greater availability for absorption if deposited on the skin (Crosera et al. 2009; Larese Filon, Bello, et al. 2016). Nguyen et al. (Nguyen et al. 2020) demonstrated that arsenic was completely leached from GaAs nanoparticles, according to dissolution tests conducted over a 7-day period and cytotoxicity of GaAs was largely due to the dissolution of toxic arsenic species.

Other factors influencing skin absorption are damaged or compromised skin (e.g., cuts, abrasions, dermatitis) which significantly increases the risk of metals absorption; as well as prolonged or repeated exposure (Larese et al. 2009; Larese Filon et al. 2015).

There are no data on Ga and As skin penetration after contact with GaAs powders.

To fill this knowledge gap, the present investigation focuses on the evaluation of the skin absorption of GaAs derived from cutting operation waste using an in vitro procedure (Franz 1975).

Franz diffusion cell represents a reliable method to estimate skin absorption of metal powders (Larese et al. 2007; Filon et al. 2009), metal compounds in nanoform (Mauro et al. 2015; Crosera et al. 2016; Larese Filon et al. 2015; Magnano et al. 2024) and metals released from heterogeneous environmental powders (Magnano et al. 2022; Larese Filon et al. 2025).

Experiments were conducted accordingly with EDETOX protocols (Williams 2004) and following OECD guidelines (2004).

In order to evaluate the impact of skin conditions, tests were conducted using both damaged, decontaminated and intact skin.

3.2 MATERIALS AND METHODS

3.2.1 GALLIUM ARSENIDE CHARACTERIZATION

Samples were obtained from processing waste of GaAs thin films grown by molecular beam epitaxy (MBE) and were examined by scanning electron microscopy (Gemini300 Scanning Electron Microscope (Zeiss, Oberkochen, Germany) and energy dispersive spectroscopy (Bruker, Billerica, MA, USA).

3.2.2 CHEMICALS

All the reagents were analytical graded chemicals: urea, sodium chloride, sodium hydrogenphosphate, potassium dihydrogenphosphate, ammonium hydroxide (25 w/v) lactic acid (90% v/v), and nitric acid (67-69% v/v). Using a Millipore purification pack system, water reagent grade was produced (MilliQ water).

2.38 g of Na2HPO4, 0.19 g of KH2PO4, and 9 g of NaCl were dissolved in 1 L of MilliQ water to create the physiological solution that was utilized as the receptor fluid (final pH = 7.35). The donor fluid, a synthetic sweat solution, was made up of 0.5% w/v sodium chloride, 0.1% w/v urea, and 0.1% w/v lactic acid in MilliQ water. The pH was raised to 4.5 and 6.5 using ammonium hydroxide.

3.2.3 DISSOLUTION TESTS

GaAs was dissolved in synthetic sweat solution at two different pH (4.5 and 6.5).

Notably, 100 mg of GaAs were dissolved in 10 mL of synthetic sweat at pH 4.5 and pH 6.5 using sonication for ten minutes. The dissolution rate was evaluated at 0, 1, 4, 8 and 24 hours by sampling and filtering 500 µL of the dispersion. Three repetitions were performed for each dissolution test.

For the subsequent ICP-MS analysis, the samples were diluted 1:50 with MilliQ water.

3.2.4 SKIN MEMBRANES PREPARATION

Full thickness human abdominal skin was collected as surgical waste from patients aged 45 -65 year after the donors informed consent with respect to the privacy rights for human subjects.

All procedures were performed in compliance with relevant laws and institutional guidelines and have been approved by the Trieste Hospital Ethical Committee n° 236/2007.

The study was carried out in accordance with the World Medical Association Declaration of Helsinki Following skin excision, hair from the epidermal layer was shaved and subcutaneous fat was removed with a scalpel blade.

Skin samples were then kept at −25 °C for a maximum of four months. It has been shown that this process doesn't compromise the skin's protective layers (Franz 1975). On the day of the experiment, skin samples were first defrosted in physiological solution at room temperature for 30 minutes. Afterward, each skin specimen was cut into 2 × 2 cm^2 pieces, which were then mounted individually on the diffusion cells. Before and after each experiment, skin integrity was assessed using a conductometer operating at 300Hz (Metrohm, 660 Conductometer, AG Oberdorfstr. 68 CH-9100 Herisau) connected to two stainless steel electrodes to measure electrical conductivity (Fasano et al. 2002).

Skin damage was induced following the method described by Bronaugh and Steward (Bronaugh and Stewart 1985) where the surface of the skin samples was abraded using the tip of a 19-gauge hypodermic needle, creating six linear marks in one direction and six perpendicular to them.

Damaged cells presented a resistance lower than 3.95 ± 0.27 $K\Omega\ cm^{-2}$ (Davies et al. 2004). For the decontaminated skin procedure, 15 minutes after the test began, the donor solutions from the relevant cells were removed. The skin was then cleansed three times using 1 mL of synthetic sweat. Any remaining particulate matter was eliminated with a cotton swab soaked in detergent. After cleaning, the donor compartments were replenished with 1 mL of fresh synthetic sweat at pH 4.5.(Larese Filon et al. 2025). Skin integrity was assessed by measuring transepidermal water loss

(TEWL) using a Delfin Vapometer (Delfin Technologies, Sweden) (Magnano et al. 2022). The average TEWL values recorded for the skin samples were below 10 $g \cdot m^{-2} \cdot h^{-1}$, consistent with findings by Guth et al. (Guth et al. 2015).

3.2.5 IN VITRO PERCUTANEOUS ABSORPTION TESTS

Static diffusion cells were used in accordance with the Franz Method (Franz 1975).

Using a thermostated water circulation system, the receptor compartment, with a mean volume of 4.5 mL, was kept at 32°C. This temperature was selected to replicate the hand's physiological temperature in a typical environment. The physiological solution used as the receptor phase was prepared by dissolving Na2HPO4, KH2PO4, and NaCl into 1 L of Milli-Q water to obtain a final solution with pH 4.5. The amount of salt present in the receiving fluid was roughly equivalent to the amount in blood. Using a PTFE magnetic stir bar, the physiological solution utilized as the receiving phase was continuously stirred. The donor and receptor compartments of each skin segment were clamped together. The average thickness of the membrane was 1 mm, and the average exposed skin area measured 0.95 cm^2. We repeated the experiment thrice using different donors for each intact, injured and decontaminated skin test. At time 0, the donor chambers of the Franz diffusion cells were filled with sonicated suspension of GaAs at a concentration of 1.0 g/L dispersed in synthetic sweat at pH 4.5 to reproduce the in vivo condition. Three blank cells were added for comparison. The blank cells were treated the same as the other cells, with the exception of the donor compartment, where only synthetic sweat was used. 1.5 mL of the receptor solution samples were taken for GaAs analysis at determined intervals of 0, 1, 4, 8 and 24 hours. Fresh physiological solution in an equivalent volume was promptly added to each receptor sample. A total of 12 independent cells were studied for 60 samples in receiving phases. These samples were previously diluted 1:10 in MilliQ water acidified with 1% nitric acid before ICP-MS analysis

3.2.6 SKIN TREATMENT AFTER THE EXPERIMENT

The skin pieces were cleaned with Milli-Q water three times following the experiment in order to eliminate any remaining GaAs trace on the skin's surface. Once taken out of the diffusion cells, skin pieces underwent heat shock, which involved freezing at -25 °C for a minute after submerging in water at 60 °C. This allowed them to be divided into the epidermis and dermis. In a closed microwave system (Multiwave PRO, Anton Paar), the skin membranes were acid-digested at 180°C for 25 minutes using a reaction mixture of 3 mL of HNO3 and 2 mL of H2O. Prior to ICP-MS analysis, the solutions derived from the mineralization process were diluted up to a volume of 20 mL using Milli-Q water. For the ICP-MS analysis, the solutions were further diluted 1:10 in MilliQ water. A total of 6 epidermis, 6 dermis and 9 full skin were studied.

3.2.7 QUANTITATIVE ANALYTICAL MEASUREMENTS

The concentrations of gallium (Ga) and arsenic (As) in the samples were determined using an Inductively Coupled Plasma-Mass Spectrometer (ICP-MS, model NexION 350X, PerkinElmer, USA), which was equipped with an ESI SC autosampler to ensure consistent and automated sample introduction. The instrument operated in Kinetic Energy Discrimination (KED) mode, utilizing ultra-high purity helium (He) as the collision gas. This mode was specifically chosen to effectively reduce spectral interferences caused by polyatomic ions, which can form in the plasma and interfere with the accurate detection of target analytes, particularly in complex matrices.

For calibration purposes, a series of five standard solutions with concentrations ranging from 0 to 100 µg/L were prepared by serial dilution from a certified 10 mg/L multistandard solution (Periodic Table MIX 1, TraceCERT®, Sigma-Aldrich). These standards were used to construct calibration curves for both Ga and As, ensuring linearity across the concentration range of interest.

The limits of quantification (LOQ) were 0.05 µg/L for both Ga (69 a.m.u.) and As (75 a.m.u.). Analytical precision, expressed as relative standard deviation (RSD), was below 3%.

All measurements were conducted under rigorously controlled laboratory conditions to minimize contamination and ensure data quality. Instrument performance was routinely verified using quality control samples and internal standards, and all data were processed using the instrument's proprietary software.

3.2.8 STATISTICAL ANALYSIS

Statistical analysis was performed using STATA-17 (StataCorp College Station, Texas) and the Mann-Whitney test was used to compare data obtained. The significance level was set below $p = 0.05$.

3.3 RESULTS

3.3.1 SAMPLE CHARACTERIZATION

Table 9 reports the dimensional composition of GaAs powders ranging between micrometric-sized particulates and nanometric-sized particles. To characterize the particle size distribution, a random sample of 100 particles was performed. Dimensional characterization showed that 12.1% of the GaAs particulate had dimensions less than 100 nm, 30% had dimensions less than 250 nm and 68.6% were inferior to 1 µm. Figure 20 reports SEM images with As and Ga chemical maps at 70 and 1 µm scales. Figure 21 reports a magnification that permit to detect particles with a size below 100 nm (red arrows).

Table 9: dimensional characterization of GaAs powders

	nm
Mean	1558
Median	567
Standard deviation	3678
Minimum	22.4
Maximum	33729
I quartile	220
III quartile	1233
	%
Particles < 100 nm	12.1
Particles <250 nm	30
Particles <1 µm	68.6

SEM image	70 µm scale	1 µm scale
GaAs sample standard SEM image	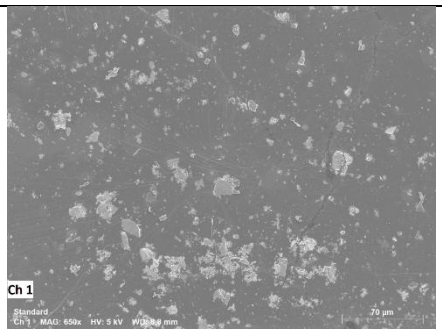	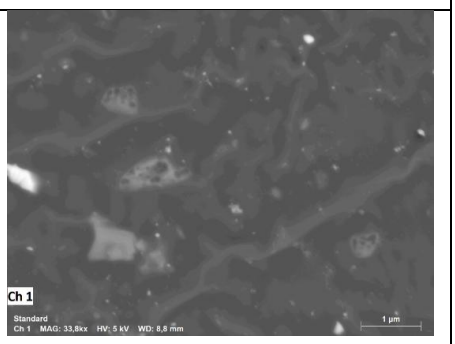
As chemical map	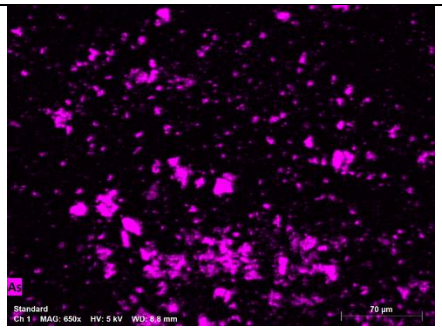	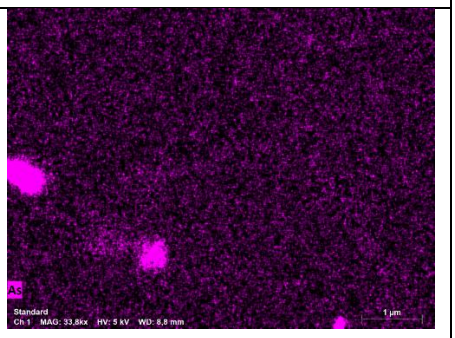
Ga chemical map	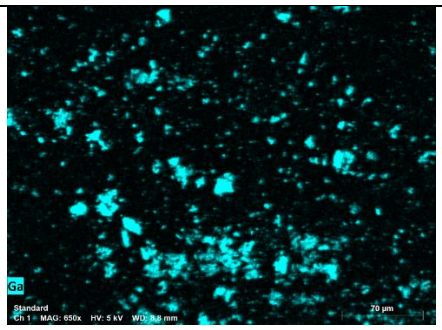	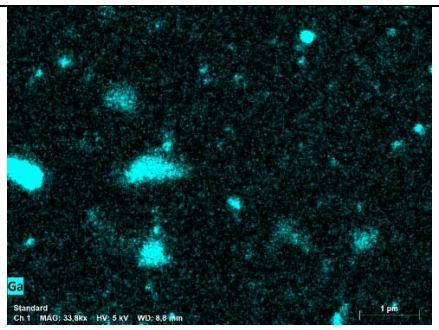

Figure 20: SEM image of GaAs sample with chemical map.

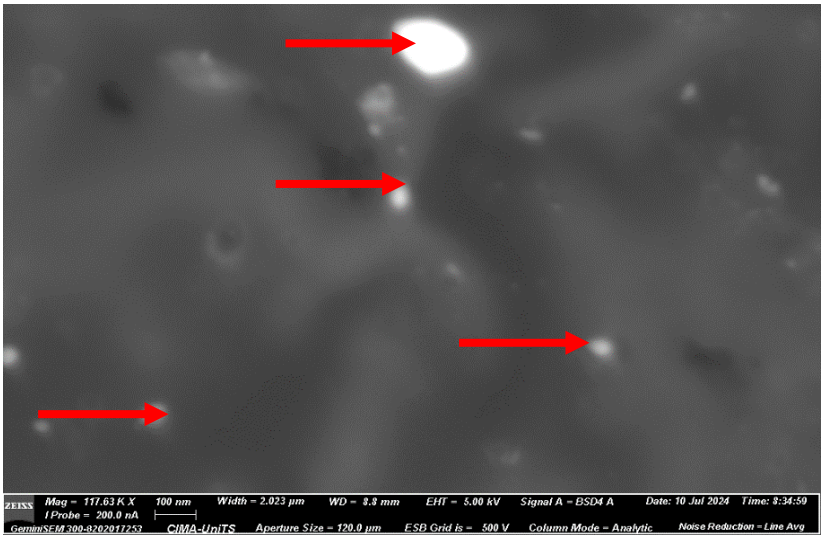

Figure 21: SEM detailed image of nanometric GaAs particles (marked with red arrows).

3.3.2 DISSOLUTION TEST

Dissolution experiments conducted in synthetic sweat demonstrated consistently higher gallium (Ga) dissolution compared to arsenic (As) after 24 h at both pH 4.5 and pH 6.5 (Table 10; Figures 22 and 23). When expressed as a percentage of the GaAs total, Ga concentrations exceeded those of As at all time points and at both pH conditions. At pH 4.5, Ga/GaAs tot was 0.09% after 1 h, compared to 0.07% for As/GaAs tot, corresponding to a difference of 0.02 percentage points. This difference increased to 0.05 points after 4 h (0.14% vs 0.09%), to 0.17 points after 8 h (0.30% vs 0.13%), and to 0.34 points after 24 h (0.52% vs 0.18%). At pH 6.5, the same trend was observed, with differences of 0.03 points at 1 h (0.12% vs 0.09%), 0.06 points at 4 h (0.16% vs 0.10%), 0.13 points at 8 h (0.27% vs 0.14%), and 0.22 points at 24 h (0.41% vs 0.19%).

When expressed as a percentage of their respective elemental totals, the magnitude of the differences was greater. At pH 4.5, Ga/Ga tot exceeded As/As tot by 0.34 points at 1 h (0.81% vs 0.47%), 0.59 points at 4 h (1.17% vs 0.58%), 1.69 points at 8 h (2.56% vs 0.87%), and 3.28 points at 24 h (4.45% vs 1.17%). At pH 6.5, the differences were 0.47 points at 1 h (1.02% vs 0.55%), 0.75 points at 4 h (1.41% vs 0.66%), 1.43 points at 8 h (2.33% vs 0.90%), and 2.36 points at 24 h (3.55% vs 1.19%).

Overall, Ga dissolution was greater at pH 4.5 than at pH 6.5, with the disparity increasing over time. After 24 h, Ga exhibited a 25% higher dissociation level at pH 4.5 compared to pH 6.5. In contrast, As presented a consistently lower dissolution profile under both conditions. Although dissolution rates at pH 6.5 were generally reduced, they remained appreciable, particularly for Ga. Notably, the relative difference in dissolution rates between Ga and As was more pronounced under the higher pH condition.

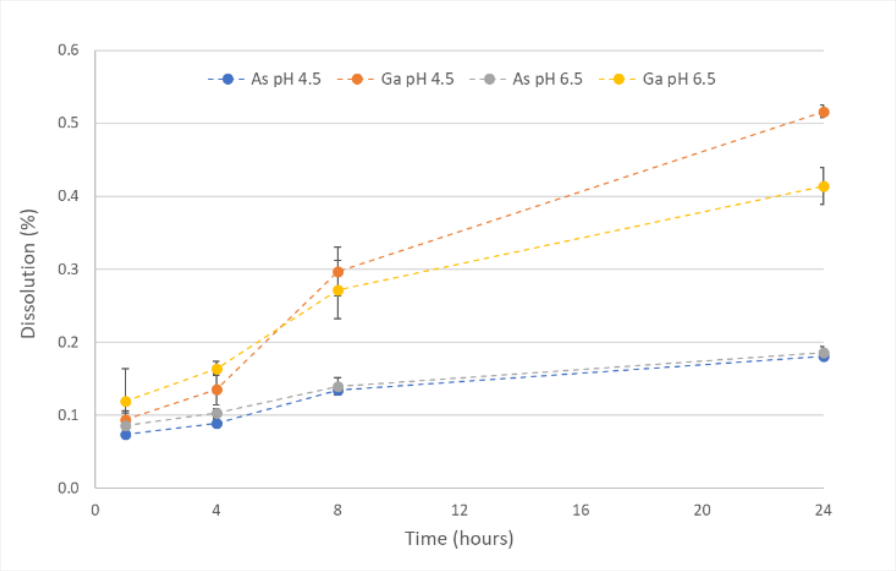

Figure 22: dissolution percentage of Ga and As compared to total GaAs in synthetic sweat at pH 4.5 and 6.5 at 1, 4, 8 and 24 h.

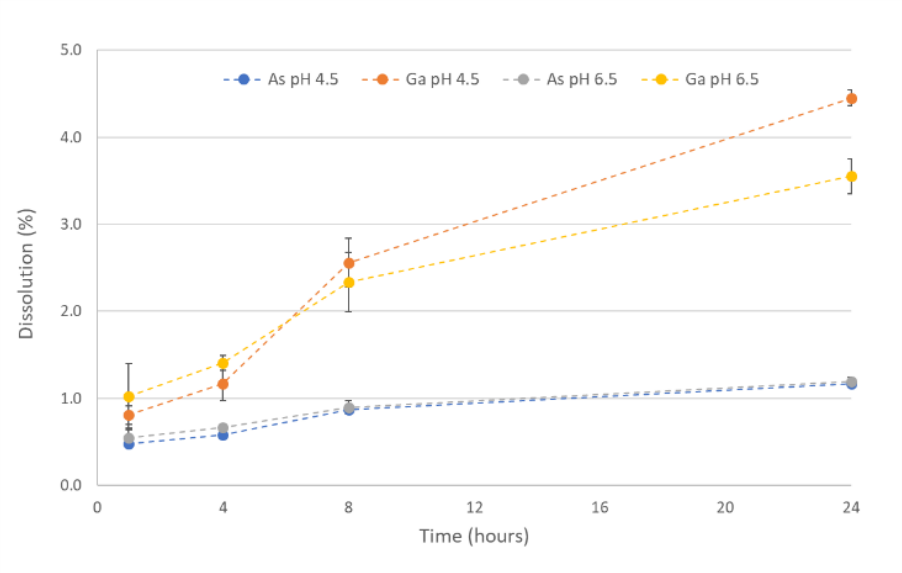

Figure 23: dissolution percentage of Ga and As compared to total Ga and total As respectively in synthetic sweat at pH 4.5 and 6.5 at 1, 4, 8 and 24 h.

Table 10: Dissolution percentage of Ga and As compared to GaAs tot/As tot/Ga tot in synthetic sweat at pH 4.5 and 6.5 after 1, 4, 8 and 24 h experiment (SD=standard deviation).

pH	Time (hours)	Mean As/GaAs tot %	SD	Mean Ga/GaAs tot %	SD	Mean As/As tot %	SD	Mean Ga/Ga tot %	SD
pH 4.5	1	0.07	0.00	0.09	0.01	0.47	0.03	0.81	0.11
	4	0.09	0.01	0.14	0.02	0.58	0.04	1.17	0.19
	8	0.13	0.00	0.30	0.03	0.87	0.03	2.56	0.28
	24	0.18	0.00	0.52	0.01	1.17	0.01	4.45	0.09
pH 6.5	1	0.09	0.02	0.12	0.04	0.55	0.11	1.02	0.38
	4	0.10	0.01	0.16	0.01	0.66	0.04	1.41	0.08
	8	0.14	0.01	0.27	0.04	0.90	0.08	2.33	0.34
	24	0.19	0.01	0.41	0.03	1.19	0.05	3.55	0.20

3.3.3 FRANZ DIFFUSION CELLS EXPERIMENT

Time-dependent trend was observed in As and Ga permeation test in receiving compartment both for damaged and decontaminated skin. After 24h of exposure, As concentration in recipient compartment was three times higher in damaged skin (1558 ± 546 ng/cm²) than in decontaminated skin (466 ± 144 ng/cm²) ($p < 0.05$) (Figure 24). After 24 h test, Ga concentration was lower compared to As, and Ga concentration detected in damaged skin (244 ± 5.29 ng/cm²) was six times higher than decontaminated skin (37.1 ± 11. 9 ng/cm²) ($p < 0.05$) (Figure 24). Moreover, Table 11 reported detailed results for Ga and As. Ga and As permeation in intact skin was very low, even though a weak yet detectable presence of arsenic (As) was observed in the receptor compartment of intact skin after 24 hours of exposure. Specifically, concentrations reached up to 41.0 ± 33.4 ng/cm² resulting higher than in blank cells (18.0 ± 7.80 ng/cm²).

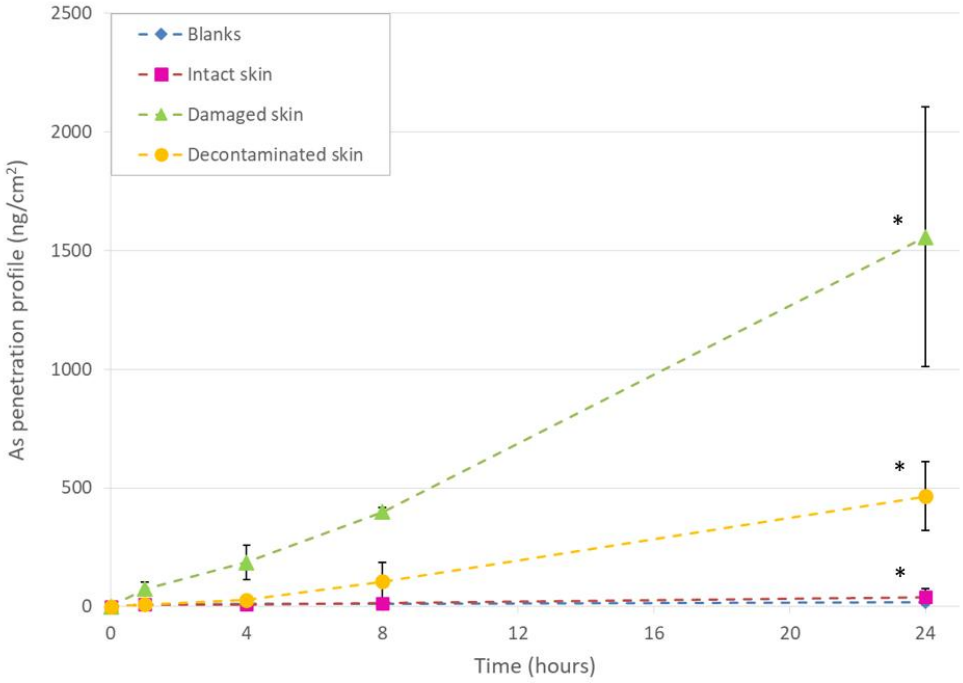

Figure 24: As permeation (ng/cm²) in recipient compartment through intact, damaged and decontaminated skin after 1, 4, 8 and 24 h.

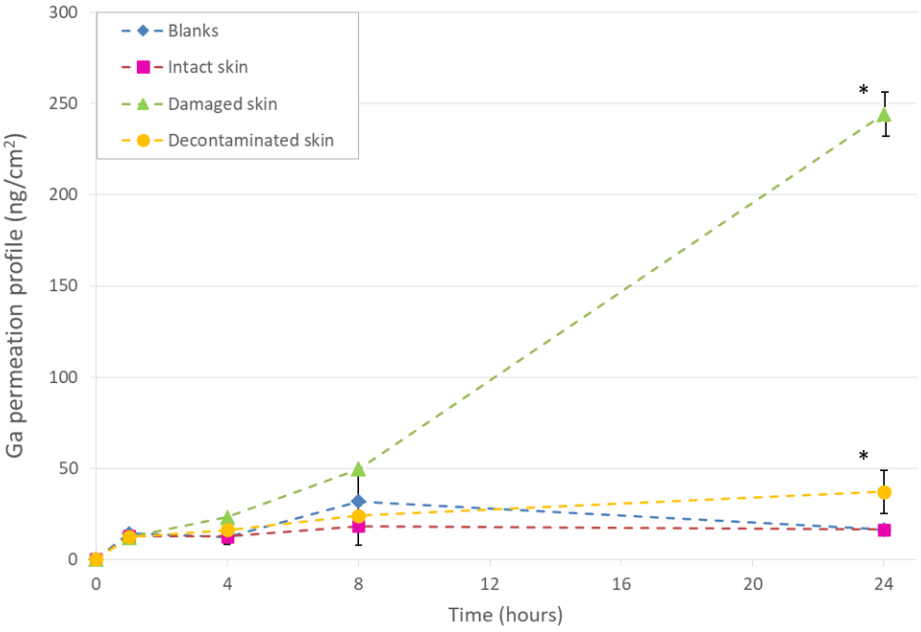

Figure 25: Ga permeation (ng/cm²) in recipient compartment through intact, damaged and decontaminated skin after 1, 4, 8 and 24 h.

*Table 11: As and Ga permeation in recipient compartment through intact, damaged and decontaminated skin after 1, 4, 8 and 24 h * p < 0.05 Mann-Whitney Test with blanks*

		As		Ga	
	Time (hours)	Mean (ng/cm²)	SD	Mean (ng/cm²)	SD
Blank cells	0	0.00	0.00	0.00	0.00
	1	7.98	0.16	14.2	5.77
	4	10.1	0.46	12.3	0.44
	8	13.4	2.95	31.8	25.2
	24	18.0	7.80	16.3	4.08
Intact skin	0	0.00	0.00	0.00	0.00
	1	9.34	0.25	12.7	0.39
	4	9.45	0.88	12.6	0.46
	8	15.1	2.78	18.2	4.49
	24	41.0*	33.4	16.3	1.56
Damaged skin	0	0.00	0.00	0.00	0.00
	1	75.5	28.1	12.0	0.08
	4	187	73.4	23.1	1.48
	8	400	17.1	49.7	4.20
	24	1558*	546	244*	5.29
Decontaminated skin	0	0.00	0.00	0.00	0.00
	1	9.85	3.68	12.4	2.17
	4	28.1	15.2	16.2	2.93
	8	106	80.1	23.9	1.84
	24	466*	144	37.1*	11.9

As and Ga concentration in different skin layers are reported in table 12 and figure 26 (As) and 27 (Ga). In intact skin samples, the mean As dermal content was 29.1 ± 9.1 µg/cm², notably higher than the 20.5 ± 4.4 µg/cm² found in the epidermis. When the skin was decontaminated, the dermal values for As remained higher at 9.57 ± 1.72 µg/cm², compared to 6.46 ± 2.13 µg/cm² in the epidermis. The average total As concentration in intact whole thickness skin was 49.6 ± 4.7 µg/cm², decreasing to 16.0 ± 0.4 µg/cm² in decontaminated whole thickness skin. For damaged whole thickness skin, the average total As amount was 91.7 ± 48.4 µg/cm². In blank cells, As penetration was minimal, averaging 1.59 ± 1.81 µg/cm² in total skin, with 0.90 ± 1.24 µg/cm² in the epidermal layer and 0.69 ± 0.57 µg/cm² in the dermal layer.

Similarly for Gallium, in intact skin, the dermal layer contained a mean of 20.9 ± 6.5 µg/cm², exceeding the 14.6 ± 1.5 µg/cm² in the epidermis. For decontaminated skin, Ga concentrations were 7.46 ± 1.31

µg/cm² in the dermis and 5.75 ± 1.75 µg/cm² in the epidermis. The average total Ga concentration in intact whole thickness skin was 35.5 ± 5.0 µg/cm², reducing to 13.2 ± 0.4 µg/cm² in decontaminated whole thickness skin. Damaged whole thickness skin showed a total gallium concentration of 63.5 ± 43.7 µg/cm². In blank cells, gallium concentration was also very low, totaling 1.17 ± 1.34 µg/cm², with 0.68 ± 0.93 µg/cm² in the epidermal layer and 0.50 ± 0.41 µg/cm² in the dermal layer. These statistically significant differences ($p < 0.05$) relative to blanks highlight the actual penetration and accumulation.

Arsenic concentrations resulted consistently higher than those of gallium across all skin conditions and layers examined. In intact skin, for example, arsenic reached a total of 49.6 µg/cm², while gallium measured 35.5 µg/cm². This trend continues in decontaminated skin, where arsenic levels were 16.0 µg/cm² versus gallium's 13.2 µg/cm². Even in damaged skin, despite the absence of individual layer data, arsenic showed a notably elevated value of 91.7 µg/cm² compared to gallium's 63.5 µg/cm². Under intact skin conditions, arsenic reached 20.5 µg/cm² in the epidermis compared to gallium at 14.6 µg/cm². Similarly, in the dermis, arsenic measured 29.1 µg/cm² while gallium was lower at 20.9 µg/cm². Following decontamination, arsenic was 6.46 µg/cm² in the epidermis versus gallium at 5.75 µg/cm²; and in the dermis, arsenic reached 9.57 µg/cm² while gallium registered 7.46 µg/cm².

Table 12: Ga and As penetration (µg/cm²) in epidermis, dermis and total skin (SD=standard deviation). p < 0.05 Mann-Whitney Test with blanks*

Arsenic						
µg/cm²	Epidermis	SD	Dermis	SD	Total	SD
Blank	0.90	1.24	0.69	0.57	1.59	1.81
Intact skin	20.5*	4.42	29.1*	9.14	49.6*	4.72
Damaged skin	/		/		91.7*	48.4
Decontaminated skin	6.46*	2.13	9.57*	1.72	16.0*	0.41
Gallium						
µg/cm²	Epidermis	SD	Dermis	SD	Total	SD
Blank	0.68	0.93	0.50	0.41	1.17	1.34
Intact skin	14.6*	1.51	20.9*	6.52	35.5*	5.00
Damaged skin	/		/		63.5*	43.7
Decontaminated skin	5.75*	1.75	7.46*	1.31	13.2*	0.43

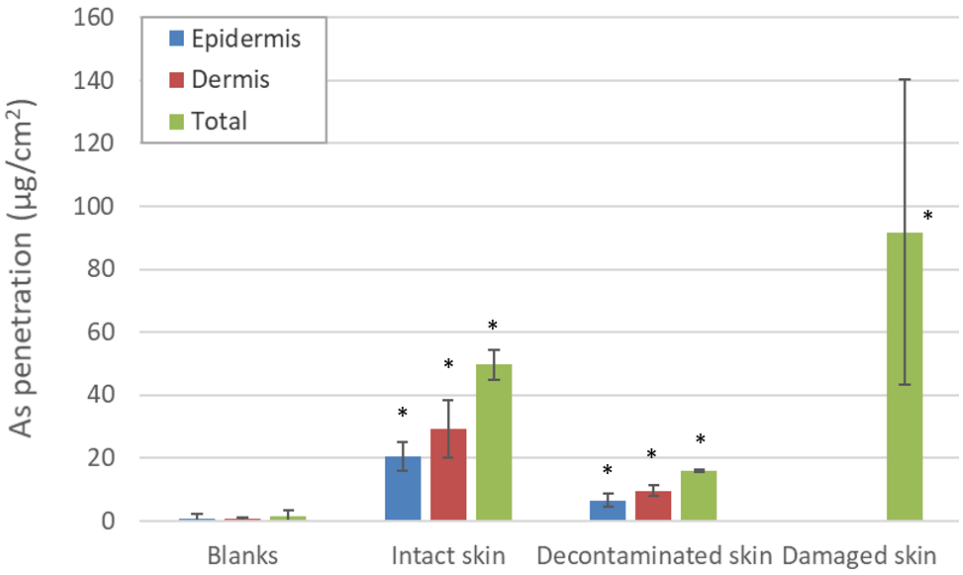

Figure 26: As penetration (µg/cm²) in epidermis, dermis and total skin.

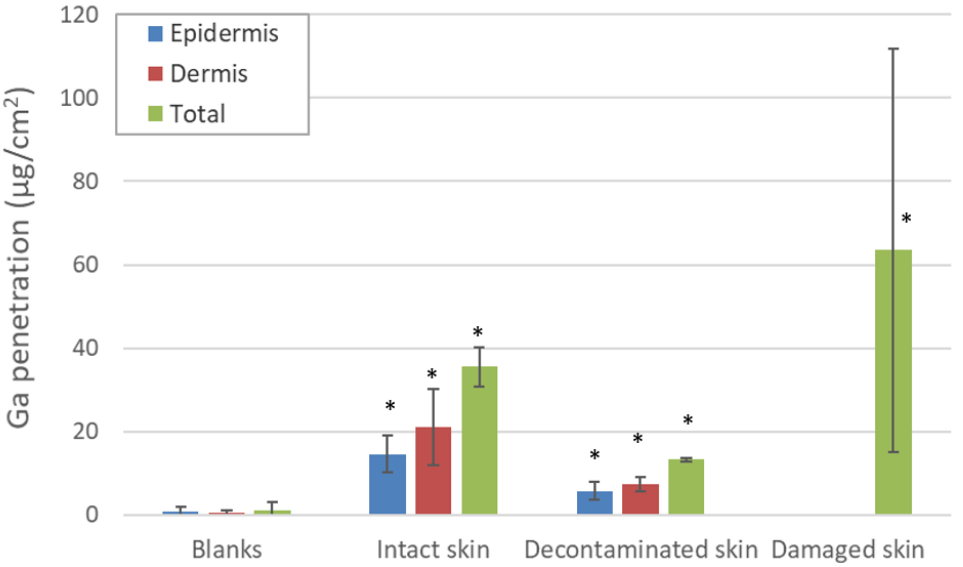

Figure 27: Ga penetration (µg/cm²) in epidermis, dermis and total skin.

3.4 DISCUSSION

This study investigated the cutaneous permeation of As and Ga after exposure to GaAs powders using the Franz diffusion cell method, aiming to address existing knowledge gaps regarding GaAs skin exposure. The research focused on both intact and damaged skin conditions, which are relevant for occupational exposure scenarios.

Exposure to synthetic sweat conditions revealed divergent dissociation profiles for gallium and arsenic, indicating element-specific solubility and release mechanisms under simulated physiological environments.

Analysis of the dissolution kinetics of GaAs in synthetic sweat reveals that gallium is significantly more prone to solubilization than arsenic under both acidic and near-neutral conditions. At pH 4.5, gallium release increases from 0.09 % of the initial GaAs mass after one hour to 0.52 % after twenty-four hours, whereas arsenic dissolution rises more modestly from 0.07 % to 0.18 % over the same interval. When each element's release is expressed relative to its own bulk content, the discrepancy becomes even more pronounced: after twenty-four hours at pH 4.5, 4.45 % of gallium has dissolved compared to only 1.17 % of arsenic. Under the milder pH 6.5 condition, gallium continues to outpace arsenic by more than two percentage points at twenty-four hours (3.55 % vs. 1.19 %), underscoring its greater chemical lability in sweat-like media.

In solution, gallium tends to form stable, soluble hydroxide complexes such as $Ga(OH)_4^-$, which enhances its dissolution rate (Diakonov et al. 1997). Arsenic, on the other hand, may form oxyanions like arsenate (AsO_4^{3-}) or arsenite (AsO_3^{3-}), but these species do not always dissolve as readily or may even precipitate depending on the redox conditions and the presence of other ions (Robins 1981).

This disparity means that gallium dissolves more efficiently than arsenic, leading to a greater difference in their respective dissolution rates.

Dissolution rates increased over time; however a notable decline in this rate was observed. This reduction might be attributed to the formation of a protective layer on the GaAs surface, composed

of gallium oxides like Ga_2O_3 and $Ga(OH)_3$, acting as a barrier, hindering further corrosion and subsequent arsenic release (Ramos-Ruiz et al. 2018).

Permeation experiments revealed a contrasting trend: arsenic exhibited significantly higher skin permeability than gallium, particularly under damaged skin conditions. After 24 hours of exposure, arsenic concentrations in the receptor fluid were consistently higher than those of gallium, indicating a greater risk of systemic exposure to arsenic through dermal contact.

The difference in skin permeation between arsenic and gallium can be explained by their physicochemical properties, particularly ionic size, solubility, and chemical speciation.

Arsenic, when released from GaAs, typically exists in aqueous environments as arsenite (As^{3+}) or arsenate (As^{5+}) ions (Flora et al. 2009). These species are small, highly soluble, and chemically mobile, which allows them to interact more easily with the skin's outer layers. Their small ionic radii and ability to form stable, water-soluble complexes enable them to diffuse through the stratum corneum (the outermost layer of the skin) and reach deeper layers, especially when the skin is damaged or hydrated (e.g., by sweat).

In contrast, gallium tends to form larger, less mobile complexes, such as Ga^{3+}, $Ga(OH)_3$, or Ga_2O_3, which are less soluble and more likely to precipitate or bind to proteins and lipids in the skin. These properties reduce gallium's ability to penetrate the skin barrier effectively.

Moreover, arsenic affinity for thiol groups (–SH) in skin proteins may facilitate its transport across cellular membranes, further enhancing its permeation(Chen et al. 2013). This is particularly relevant in damaged skin, where the barrier function is compromised, allowing easier passage of small, reactive ions like arsenic.

Consequently, arsenic in its ionic forms is more likely to penetrate the skin barrier, especially when the skin is compromised, as damage significantly enhances its permeability , which is consistent with studies showing that skin can absorb metal ions, especially when facilitated by sweat (Larese et al. 2007; Crosera et al. 2009; Larese Filon et al. 2015; Larese Filon, Crosera, et al. 2016).

Across all skin conditions, arsenic permeation in the receptor compartment followed a clear barrier-dependent trend. After 24 hours, arsenic in damaged skin reached 1558 ± 546 ng/cm², more than three times the 466 ± 144 ng/cm² observed in decontaminated skin, and markedly higher than the 41.0 ± 33.4 ng/cm² measured beneath intact skin ($p < 0.05$). Gallium displayed a similar pattern but at lower absolute levels, rising to 244 ± 5.29 ng/cm² in damaged skin, 37.1 ± 11.9 ng/cm² following decontamination, and only 16.3 ± 1.56 ng/cm² under intact conditions ($p < 0.05$). The progressive increase from 1 to 24 hours confirms sustained diffusion under sink conditions.

Within the skin itself, intact samples retained far more mass than appeared in the receptor compartment, underscoring the skin's role as a reservoir. For intact skin, arsenic accumulated to 49.6 ± 4.7 µg/cm² total, with 29.1 ± 9.1 µg/cm² in the dermis and 20.5 ± 4.4 µg/cm² in the epidermis. After decontamination, total arsenic fell to 16.0 ± 0.4 µg/cm², yet dermal levels (9.57 ± 1.72 µg/cm²) still exceeded those in the epidermis (6.46 ± 2.13 µg/cm²). Minimal penetration observed in blank controls (1–2 µg/cm²) confirms that the measured tissue burdens represent genuine uptake rather than artifacts introduced by the experimental procedure.

Decontamination processes, often involving surfactants or solvents, remove surface lipids and modifies the structure of the stratum corneum, enhancing the concentration gradient across viable skin layers. This explains the elevated receptor concentrations of arsenic and gallium, despite a reduction in overall tissue retention.

Mechanical damage to the stratum corneum further compromises barrier integrity and tight junction cohesion. This disruption elevates both uptake and permeation, producing the highest tissue concentrations for arsenic (91.7 ± 48.4 µg/cm²) and for gallium (63.5 ± 43.7 µg/cm²) as well as highest concentrations in recipient compartment (after 24 hours: As = 1558 ± 546 ng/cm^2; Ga = 244 ± 5.29 ng/cm^2).

3.5 CONCLUSION

Permeation tests conducted in this study are consistent with the findings of Ouypornkochagorn et al. who demonstrated that inorganic As species, particularly arsenite (As^{3+}) and arsenate (As^{5+}), can penetrate the skin layers and accumulate, forming a dermal reservoir capable of releasing arsenic into the bloodstream over time (Ouypornkochagorn and Feldmann 2010). These results challenge earlier assumptions that dermal absorption of As from GaAs waste is negligible, as proposed by previous studies (Wester et al. 1993; Lowney et al. 2007; 2005; Marin Villegas and Zagury 2023).

In contrast, Ga showed limited skin permeability, aligning with the findings of Fujihara et al., who reported that Ga species such as Ga^{3+} and $Ga(OH)_3$ exhibit low solubility and mobility, reducing their ability to cross the skin barrier(Fujihara and Nishimoto 2021).

Importantly, permeation tests confirmed that intact skin serves as a highly effective barrier against the transdermal absorption of both Ga and As. This finding aligns with the well-established role of the stratum corneum, the outermost layer of the skin, as a primary defense mechanism against chemical penetration (Larese Filon et al. 2015; Brouwer et al. 2016). The dense lipid matrix and tightly packed corneocytes in this layer significantly limit the diffusion of most ionic and polar substances under normal conditions.

However, the situation changes markedly in the presence of skin lesions or microabrasions, which compromise the structural integrity of the stratum corneum (Larese et al. 2009). Under these conditions, the permeation of both As and Ga increases significantly, as the disrupted barrier allows easier access to the underlying viable epidermis and dermis.

Moreover, the decontamination process, which typically involves the use of surfactants, solvents, or alcohol-based agents, was found to alter the lipid architecture of the stratum corneum. These agents can extract lipids and denature proteins, thereby increasing skin permeability even in the absence of visible damage. This effect was evidenced by the higher concentrations of both Ga and As detected in

the dermal layer compared to the epidermis, suggesting that these elements are capable of penetrating deep into the skin once the barrier is compromised.

This is particularly concerning in occupational settings where workers may handle GaAs thin film waste, as even minor skin damage—often unnoticed—can lead to enhanced dermal absorption of toxic elements.

This observation has critical implications for workplace safety. It highlights the need for protective measures, such as gloves, especially during decontamination procedures or when handling GaAs materials in environments where skin exposure is possible. Furthermore, the accumulation of these elements in the dermis raises concerns about possible systemic exposure, particularly given the potential for nanoparticles or dissolved ions to enter the bloodstream and distribute to internal organs (Nguyen et al. 2020; Brouwer et al. 2016; Larese Filon, Bello, et al. 2016).

4. TRANSDERMAL ABSORPTION OF CdS QUANTUM DOTS (QDs) QUANTUM DOTS: AN EX-VIVO INVESTIGATION USING FRANZ DIFFUSION CELLS

4.1 INTRODUCTION

Cadmium sulphide (CdS) quantum dots (QDs) are semiconductor nanocrystals composed of cadmium and sulphide, belonging to the II–VI group of materials having dimensions ranging from 2 to 10 nanometers in diameter. CdS QDs are classified as zero-dimension nanomaterials because quantum confinement occurs in all three dimensions (length, width, and thickness), leading to a specific optical, electronic, and magnetic properties, which are much different compared to bulk materials (Lahariya et al. 2023).

CdS quantum dots are remarkable nanomaterials that display unique properties distinct from bulk cadmium sulfide. Their nanoscale size results in a high surface-to-volume ratio, meaning a significant number of their atoms are exposed on the surface, which enhances their reactivity and influences both optical and electronic behaviors. One of the main characteristics is their enlarged band gap—an effect of quantum confinement—which allows for the tuning of optical properties such as emission wavelength. This tunability is highly valuable in fields like bio-imaging, LED technology, and laser development. Furthermore, the alteration in electronic properties leads to improved charge carrier dynamics and higher photoluminescence quantum yields, making CdS quantum dots exceptionally useful in optoelectronic devices, solar cells, and chemical sensing applications. The band gap of the semiconductor material is inversely proportional to the square of the particle's radius, meaning smaller quantum dots have larger band gaps. This confinement also causes the band structure to become discrete for both the conduction and valence bands, and the generation of trap levels between these

bands can further tune electronic properties such as conductivity and resistivity. The absorption peak also shifts due to these changes in the band structure.

CdS QDs exhibit high luminescence efficiency, narrow emission spectra, broad absorption bands, and excellent photostability. Their direct band gap and high quantum yield make them ideal for optoelectronic applications. The emission color of CdS QDs can be tuned across the visible spectrum by controlling the particle size, which is a direct consequence of quantum confinement. These properties are influenced by synthesis methods, surface passivation, and the surrounding environment.

Cd-based QDs may be synthetized in a large variety of chemical compounds depending on differences in core and shell formulation, geometric parameters (e.g., diameter, aspect ratio) (Liu et al. 2019), and surface functionalization (Chena et al. 2012).

Cadmium-based quantum dots (Cd-based QDs) have gained significant attention for their versatile applications in biomedical imaging, biosensing, light-emitting diodes (LEDs), solar energy conversion, photocatalysis, and optical sensors. Their remarkable optical properties—such as strong, stable fluorescence—enable precise tracking of biological processes. Functionalization with biomolecules allows for targeted imaging and drug delivery, enhancing their biomedical utility (El-Hamidy 2021; Ebrahim et al. 2023; Baytar et al. 2025).

4.1.1 CdS QUANTUM DOTS TOXICITY

CdS is classified by the International Agency for Research on Cancer (IARC) as a Group 1 carcinogen for lung cancer, but this classification applies specifically to cadmium and cadmium compounds as a group (GF et al. 2025).

In vitro studies consistently demonstrate that CdS QDs can be cytotoxic. The cytotoxicity of CdS QDs is primarily attributed to the release of cadmium ions (Cd^{2+}) (Mancini et al. 2008; Navarro et al. 2010; Mo et al. 2017).

Cadmium is a persistent heavy metal with a long biological half-life in humans—ranging from approximately 10 to 35 years, depending on the organ and individual factors (Vijiyakumar and Prince 2025). Once absorbed, Cd bioaccumulates in the body, particularly in the kidneys and liver, which are recognized as primary target organs for its toxic effects.

Following systemic distribution, Cd binds to metallothionein and is transported throughout the body, where its slow excretion contributes to long-term retention and cumulative toxicity. Cd is excreted through urine causing nephrotoxic. Cruz et al. demonstrated that CdS QDs coated with dextrin (CdS-dex QDs) exhibit cytotoxic effects on human tumor cells that cannot be considered harmless since these nanoparticles are capable of penetrating subcellular compartments, and their biological activity may induce pathophysiological changes in a manner dependent on concentration (Cruz et al. 2024)

The physicochemical properties of CdS QDs—such as size, shape, surface charge, and functionalization—play a pivotal role in modulating their toxicity (Tsoi et al. 2013). Smaller QDs, due to their higher surface area-to-volume ratio, are potentially more reactive and prone to releasing Cd^{2+} ions and tend to exhibit greater reactivity and cellular uptake, thereby enhancing their toxic potential. They may also exhibit different cellular uptake and biodistribution patterns. Surface coatings, including polyethylene glycol (PEG), thiol ligands, and peptides, have been employed to improve colloidal stability and reduce nonspecific interactions with cellular membranes. However, these modifications can also alter biodistribution and clearance profiles, complicating the assessment of long-term toxicity (Lu et al. 2024).

Xu et al. (Xu et al. 2012) investigates the toxicokinetics and tissue distribution of cadmium based quantum dots (QDs) in male Sprague-Dawley rats. Researchers administered different sizes and solubility forms of Cd-based QDs via tail vein injection and monitored cadmium concentrations in blood and organs over time. Blood samples were collected at multiple time points post-injection, and organs such as liver, kidney, brain, and testes were analyzed for cadmium content. The results showed that cadmium levels in the blood decreased gradually after exposure, with smaller and less soluble QDs exhibiting slower elimination rates. Soluble Cd-based QDs were cleared more rapidly from the body,

and their metabolism followed a first-order two-compartment model. Tissue distribution revealed that Cd accumulated primarily in the liver, kidney, and testes, with variations depending on particle size and solubility.

Cadmium-based QDs can disrupt the cell's redox balance, leading to oxidative stress (Li et al. 2009; Yong et al. 2013). This stress results from the overproduction of reactive oxygen species (ROS), including superoxide, hydroxyl radicals, peroxide radicals, hydrogen peroxide, and singlet oxygen. These ROS can interfere with normal cellular processes. If ROS levels become too high, the cell's antioxidant defenses may be overwhelmed, potentially causing mitochondrial dysfunction and triggering apoptosis (Paesano et al. 2016). Moreover, elevated ROS can damage DNA, leading to fragmentation, double-strand breaks, and impaired replication and transcription, all of which contribute to genotoxicity.

Within the respiratory system, pulmonary exposure to Cd-based QDs in rats caused robust inflammatory responses, characterized by the influx of immune cells and the release of pro-inflammatory cytokines, leading to lung injury and potentially impairing the critical phagocytic function of alveolar macrophages and causing local neutrophil inflammation in the lungs (Ma-Hock et al. 2012; Roberts et al. 2013; Wang et al. 2015).

The liver, a primary organ for detoxification and QDs accumulation following systemic exposure, is particularly vulnerable, with Cd-based QDs causing hepatotoxicity evidenced by oxidative stress, lipid peroxidation, and alterations in liver enzyme activities, ultimately leading to cellular damage and potential tissue pathology (Nguyen et al. 2015; Zhang et al. 2015).

Furthermore, the immune system exhibits sensitivity to Cd-based QDs, which can induce immunomodulation by directly affecting the viability and function of lymphocytes and macrophages, and by promoting the release of pro-inflammatory cytokines such as IL-6 and TNF-α, thereby contributing to systemic inflammation and potentially compromising both innate and adaptive immune responses (Wang et al. 2016).

There is also concern about neurotoxicity, as studies have shown that Cd-based QDs can induce cell death and trigger apoptosis in primary hippocampal neurons derived from rats (Wu et al. 2015). These effects have been observed to vary depending on the concentration of the quantum dots, the duration of exposure, and the size of the nanoparticles.

Animal studies investigating the dermal permeation of Cd-based QDs have highlighted the potential for skin penetration and subsequent systemic distribution, particularly when the epidermal barrier is compromised. Research, employing models such as porcine (Ryman-Rasmussen et al. 2006) and murine skin (Gopee et al. 2009), has demonstrated that while intact stratum corneum generally presents a robust impediment to Cd-based QD translocation, damage to this protective layer (e.g., through abrasion) significantly enhances percutaneous absorption. Quantitative analyses to detect Cd presence in sentinel organs (e.g., draining lymph nodes, liver, and spleen), have confirmed the uptake and systemic bioavailability of Cd-based QDs following intradermal injection (Gopee et al. 2007).

Gratieri et al. investigated the penetration of fluorescent QDs (including Cd-based QD) through human skin using Saarbrücken penetration model (SB-M) (Gratieri et al. 2010). Experiment highlighted that, while mechanical actions could affect Cd-based QDs distribution on the skin surface, there was generally no evidence of penetration into deeper skin layers in all cases tested on intact human skin. Penetration was only observed after massaging of damaged skin.

This study addresses a gap in current knowledge by investigating the dermal absorption of cadmium sulfide quantum dots (CdS QDs) using a well-established in vitro Franz diffusion cell system (Franz 1975). This particular method has proven reliable for evaluating the skin uptake of various metal based nanoparticles (Larese et al. 2007; Crosera et al. 2009; Mauro et al. 2015; Crosera et al. 2016).

All experimental steps adhered to the EDETOX project protocols (Williams, 2004) and conformed to the OECD guidelines for skin absorption testing (2004). To understand how skin integrity affects CdS QD penetration, experiments were conducted on intact and damaged skin.

4.2 MATERIALS AND METHODS

4.2.1 CDS QDS PREPARATION AND CHARACTERIZATION

For the investigation, NAC-capped CdS QDs (N-acetylcysteine Cadmium Sulfide quantum dots) were used.

These quantum dots consist of cadmium sulfide (CdS) as the semiconductor core, which exhibits size-dependent optical characteristics such as tunable photoluminescence. The surface of the nanoparticles is passivated with N-acetylcysteine (NAC), a small molecule bearing both thiol and carboxyl functional groups. This dual functionality facilitates strong binding to the CdS surface while concurrently enhancing colloidal stability in aqueous environments. The capping of CdS quantum dots with NAC significantly improves the water solubility of the quantum dots, which is essential for their integration into biological systems.

These functionalized quantum dots have demonstrated efficacy in a range of applications. In biosensing, NAC-capped Cd-based QDs can be used to detect specific biomolecules via fluorescence quenching or enhancement mechanisms, often with high sensitivity and selectivity (Fadhil et al. 2024). In cellular imaging, their photostability and biocompatibility make them suitable as fluorescent probes for tracking biological processes in real time (Zhao et al. 2010; Xue et al. 2012).

4.2.2 SYNTHESIS OF NAC-CAPPED CdS QUANTUM DOTS

N-acetyl-L-cysteine (NAC)-capped Cadmium Sulfide (CdS) Quantum Dots (QDs) were synthesized directly in aqueous solution following a modified procedure adapted from Yang et al. (Yang et al. 2018). For the preparation, 41.9 mg of Cadmium chloride dihydrate ($CdCl_2 \cdot 2H_2O$) and 34.2 mg of NAC were dissolved in 40 mL of bidistilled water. The pH of this solution was adjusted to 8.0–9.0 by dropwise titration with a 2.0 M NaOH solution under constant stirring. After 30 minutes of stirring, 3.83 mL of a

50 mM sodium sulfide nonahydrate ($Na_2S \cdot 9H_2O$) solution was added drop by drop under the same stirring conditions. The reaction was allowed to proceed for an additional 30 minutes to yield the NAC-capped CdS QDs. To investigate the influence of temperature on QD size, the entire synthesis procedure was performed at three different temperatures: 0°C, 30°C, and 50°C. The final concentration of QDs in the solution was approximately 4.3 mM, based on the initial Sodium sulfide (Na_2S) concentration (corresponding to approximately 490 ppm of Cd).

4.2.3 CHARACTERIZATION OF CdS QUANTUM DOTS

The synthesized CdS QD solutions were characterized using UV-vis spectroscopy and fluorescence spectroscopy. UV-vis absorption spectra were recorded to identify the main absorption peak, which was consistently observed around 320 nm for all three QD species. Fluorescence emission spectra were recorded under 350 nm excitation at room temperature (figure 28). Emission maxima, ranging from 470 nm to 580 nm, were used to infer size differences (table 13).

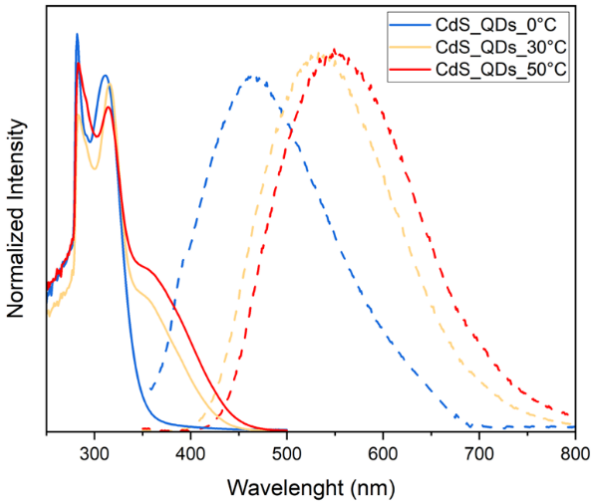

Figure 28: size differences in CdS QDs evident by UV-Vis spectroscopy. The absorption spectra are shown as solid lines, and the emission spectra as dashed lines.

The energy of the emitted photons represents the sum of the bandgap of the material and the additional change in energy due to quantum confinement (ΔE_{qc}) in small crystals. Using emission data, the size can be calculated via eq. 1 and 2:

$$E_{photon}(\lambda_{max}) = \frac{hc}{\lambda_{max}} = E_{band\ gap} + \Delta E_{qc} \quad (1)$$

Here, E_{photon} represents the maximum emitted energy, h is Planck's constant, c is the speed of light, λ_{max} is the maximum wavelength of the emitted photon, and$E_{band\ gap}$is the bulk bandgap energy for macroscopic CdS (~2.42 eV). The energy is determined via of the emission for the CdS QDs. Once this quantum confinement energy is determined, the particle size can be extracted from eq 2:

$$\Delta E_{qc} = \frac{h^2}{8R^2}\left(\frac{1}{m_e^*} + \frac{1}{m_h^*}\right) \quad (2)$$

Here, R is the particle radius, m_e^* is the effective mass of the electron, m_h^* is the effective mass of the hole, and ΔE_{qc} is the quantum confinement energy. Note that, for CdS, m_e^*=0.19$m_e$and m_h^*= 0.80m_e, where m_e is the mass of the electron. The results are reported in Table 13.

Table 13: particle radius in nanometers, calculated using eq. 1 and 2 from emission data

SAMPLE	Temperature (°C)	λ Emission Max (nm)	Size (nm)
CdS_QDs_0	0	478	3.4
CdS_QDs_30	30	527	5.8
CdS_QDs_50	50	548	6.7

4.2.4 HUMAN SKIN PREPARATION

Human abdominal skin, comprising full epidermal and dermal thickness, was obtained as post-surgical biological material from volunteer donors aged between 45 and 65 years.

All donors signed an explicit informed consent, ensuring full adherence to privacy regulations concerning human subjects. The experimental protocols were conducted in strict observance of pertinent legal frameworks and institutional guidelines, receiving specific endorsement from the Trieste Hospital Ethical Committee (Protocol No. 236/2007).

Furthermore, the entire investigation conformed to the ethical principles outlined in the World Medical Association Declaration of Helsinki. Following surgical excision, any hair present on the epidermal surface was meticulously removed by shaving, and subcutaneous adipose tissue was carefully excised using a scalpel blade.

Skin samples were frozen and stored at a temperature of -25 °C.

On the day of experiment, frozen skin samples were thawed by immersion in physiological solution at ambient temperature for 30 minutes and then each skin section was precisely cut into 2×2 cm^2 squares, which were then individually positioned onto the diffusion cells (Franz 1975).

Before and after each experiment, the integrity of the skin barrier was evaluated using a conductometer (Metrohm, 660 Conductometer, AG Oberdorfstr. 68 CH-9100 Herisau) operating at 300 Hz (Fasano et al. 2002).

Skin damage was intentionally induced on selected samples by mechanically abrading the skin, in accordance with the protocol established by Bronaugh and Stewart (Bronaugh and Stewart 1985), creating six parallel linear scratches in one direction and an additional six perpendicular to the first set, using the tip of a 19-gauge hypodermic needle. Damaged skin samples presented electrical resistance below 3.95 ± 0.27 $k\Omega \cdot cm^{-2}$ (Davies et al. 2004).

4.2.5 PERCUTANEOUS ABSORPTION TEST SETUP

Static diffusion cells, configured according to the Franz Method (Franz 1975), were employed for the in vitro percutaneous absorption assessments.

All reagents used were of analytical grade, including sodium chloride (NaCl), sodium hydrogen phosphate (Na_2HPO_4), potassium dihydrogen phosphate (KH_2PO_4), nitric acid (HNO_3, 67–69% v/v) and hydrogen peroxide (H_2O_2, 30% v/v). Reagent-grade water was prepared using a Millipore purification system (MilliQ).

To formulate the receptor fluid (physiological solution), 2.38 g of Na_2HPO_4, 0.19 g of KH_2PO_4, and 9 g of NaCl were dissolved in 1 L of MilliQ water, yielding a final pH of 7.35. The salt concentration in this receiving fluid was designed to approximate that found in human blood. Continuous agitation of the physiological solution in the receiving phase was ensured by a polytetrafluoroethylene (PTFE) magnetic stir bar. The receptor compartment, with an average volume of 4.5 mL, was maintained at a constant temperature of 32°C to simulate the physiological temperature of the human hand under typical environmental conditions. Temperature was maintained using a thermostated water circulation system.

Each segment of skin was securely clamped between the donor and receptor compartments. The average thickness of the skin membrane utilized was 1 mm, and the mean exposed skin area was measured at 0.95 cm^2.

Skin permeation experiment was performed for both 3.4 nm CdS QDs, 5.8 nm CdS QDs and 6.7 nm CdS QDs.

The donor solution used for the skin permeation tests consisted of 0.5 mL of a buffer solution containing 0.8 M Na_2HPO_4/NaH_2PO_4 and 3.5 M NaCl was added to 20 mL of the QD-containing solution. The resulting pH of the CdS QDs solutions ranged between 6.8 and 7.0. At the start of the experiment, the donor chambers of the Franz diffusion cells were loaded with a sonicated suspension of 1 mL of solution.

For comparative purposes, two blank cells were included (one using intact skin and another using damaged skin). These blank cells underwent identical treatment, except their donor compartments contained only physiological solution. Samples of 0.5 mL from the receptor solution were collected at predetermined intervals of 1, 4, 8, and 24 hours for subsequent analysis. An equivalent volume of fresh physiological solution was promptly added to each receptor compartment following sample collection. Prior to Inductively Coupled Plasma-Mass Spectrometry (ICP-MS) analysis, these samples were diluted 1:10 in MilliQ water acidified with 1% nitric acid.

Each experiment was replicated two times, with distinct donors contributing skin samples for each of the intact and abraded skin tests.

4.2.6 SKIN SAMPLE PROCESSING AND ANALYSIS

Following the permeation experiments, skin specimens were thoroughly rinsed three times with Milli-Q water to eliminate any residual CdS QDs from the surface.

Once removed from the diffusion cells, the skin pieces underwent a heat shock treatment: they were submerged in water at 60 °C for one minute, immediately followed by freezing at -25 °C. This thermal shock facilitated the separation of the epidermis from the dermis. The isolated skin membranes (epidermis, dermis, or full thickness, as appropriate) were then subjected to acid digestion in a closed microwave system (Multiwave PRO, Anton Paar) at 180°C for 25 minutes, using a reaction mixture composed of 2 mL of HNO3, 1 mL of H2O and 0.5 mL of H2O2. The solutions resulting from this mineralization process were subsequently diluted to a final volume of 20 mL with Milli-Q water. For the ICP-MS analysis, these solutions were further diluted 1:10 in MilliQ water.

For intact skin samples, Cd concentration was analyzed in both the epidermis and dermis. In contrast, for damaged skin samples, Cd concentration was directly assessed in the full-thickness skin.

4.2.7 QUANTITATIVE ANALYTICAL MEASUREMENTS

Inductively Coupled Plasma-Mass Spectrometer (NexION 350X, PerkinElmer, USA) equipped with an ESI SC autosampler was used to assess cadmium (Cd) concentration in the samples.

In order to mitigate spectral interferences caused by polyatomic ions, ICP-MS was set in Kinetic Energy Discrimination (KED) mode, employing ultra-high purity helium (He) as collision gas.

To build calibration curves, a series of five standard solutions, with concentrations spanning from 0 to 100 µg/L, were prepared via serial dilution from a certified 10 mg/L multistandard solution (Periodic Table MIX 1, TraceCERT®, Sigma-Aldrich).

The limit of quantification (LOQ) for the analytical protocol was determined to be 0.05 µg/L. Method reproducibility, assessed via relative standard deviation (RSD), consistently exhibited values below 3%. All analyses were conducted under controlled laboratory settings to reduce the potential for extraneous contamination and ensure data integrity. Instrumental reliability was routinely monitored through the evaluation of control standards and embedded calibration references. Data acquisition and post-processing were performed using the proprietary software platform associated with the instrumentation.

4.2.8 FLUORESCENT MICROSCOPY VISUALIZATION

The permeation and distribution of the CdS quantum dots within the skin layers were visualized using a ZOE™ Fluorescent Cell Imager (Bio-Rad Laboratories, Hercules, CA, USA). 30-micron thick sections were prepared using a microtome and then placed on a glass slide for subsequent fluorescence microscopy analysis. Brightfield and fluorescence images were captured to observe the integrity of the tissue and the presence of the quantum dots, respectively.

For fluorescence imaging, the samples were excited with the appropriate LED light source to match the fluorescence properties of the CdS quantum dots. The ZOE's integrated software was used to acquire images, which were then saved in a high-resolution format for further analysis. The images provided a qualitative assessment of the quantum dots' penetration depth and distribution within the stratum corneum, epidermis, and dermis.

4.2.9 STATISTICAL ANALYSIS

Statistical analysis was conducted using STATA-17 (StataCorp College Station, Texas). The Mann-Whitney test was employed to facilitate comparisons between the obtained data sets. A significance level of $p < 0.05$ was established for all statistical tests.

4.3 RESULTS

4.3.1 FRANZ DIFFUSION CELLS EXPERIMENT

The percutaneous absorption of three different sizes of N-acetylcysteine (NAC)-capped cadmium sulfide (CdS) quantum dots (QDs)—3.4 nm, 5.8 nm, and 6.7 nm—was investigated using an ex-vivo Franz diffusion cells model with human abdominal skin. Experiments were conducted on both intact and mechanically damaged skin to evaluate the role of the epidermal barrier. The concentration of cadmium (Cd) in the receptor fluid was quantified at various time points (1, 4, 8, and 24 hours) using Inductively Coupled Plasma-Mass Spectrometry (ICP-MS) (table 14).

Our findings indicate that for all three QD sizes, Cd skin permeation was minimal through intact human skin (figure 29, 30 and 31). Cd levels detected in the receptor fluid for the intact skin group remained relatively low across the 24-hour experimental period and were similar to blank cells. For the 3.4 nm QDs, the average cumulative Cd permeation was 4.07 ± 0.20 ng/cm² after 24 hours. The 5.8 nm QDs showed a slightly higher cumulative permeation of 13.67 ± 12.62 ng/cm² at 24 hours, though with a high standard deviation. The 6.7 nm QDs exhibited a similar profile, reaching 4.56 ± 1.05 ng/cm² after 24 hours.

In contrast, experiments conducted on mechanically damaged skin demonstrated a substantial increase in Cd penetration for all QD sizes (figure 29, 30 and 31). The higher increase was observed with the smallest 3.4 nm QDs, which reached an average cumulative Cd permeation in recipient

compartment of 302.87 ± 134.87 ng/cm² after 24 hours. This was a statistically significant result ($p < 0.05$) when compared to the intact skin group and the blank controls. Similarly, the 5.8 nm QDs on damaged skin showed a significant increase in absorption, with a cumulative permeation in recipient compartment of 121.56 ± 64.27 ng/cm² after 24 hours ($p < 0.05$). The largest 6.7 nm QDs also showed an increased, statistically significant penetration through damaged skin, reaching 11.34 ± 0.89 ng/cm² at the 24-hour mark ($p < 0.05$).

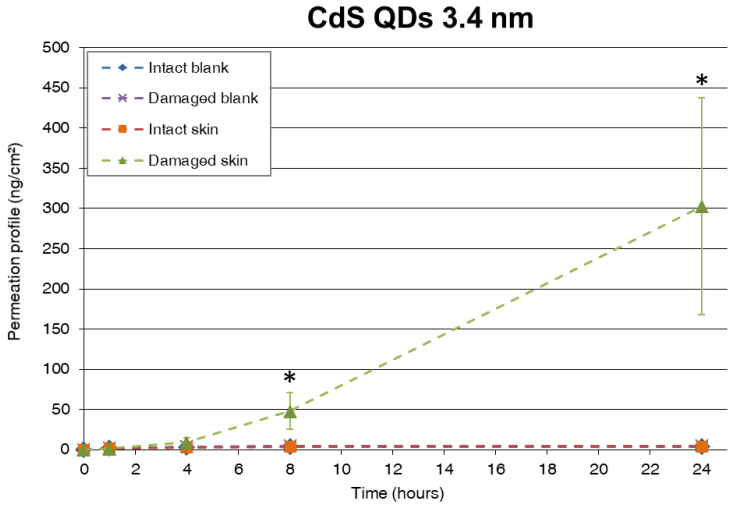

Figure 29: 3.4 nm CdS QDs permeation (ng/cm²) in recipient compartment through intact and damaged skin after 1, 4, 8 and 24 h.

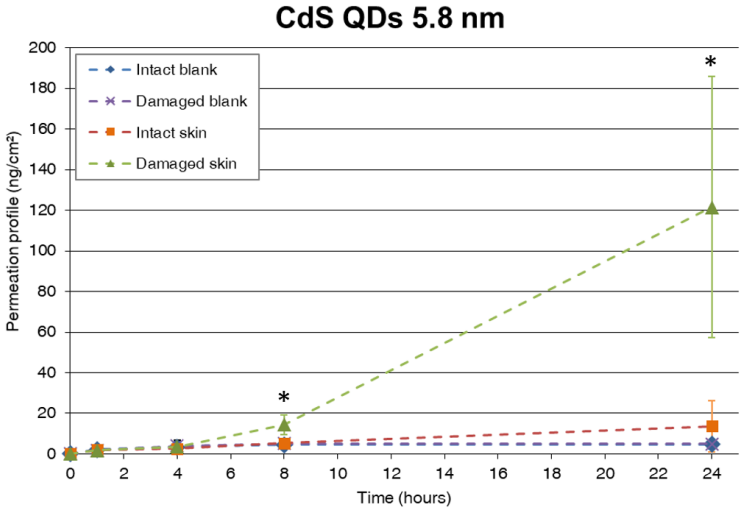

Figure 30: 5.8 nm CdS QDs permeation (ng/cm²) in recipient compartment through intact and damaged skin after 1, 4, 8 and 24 h.

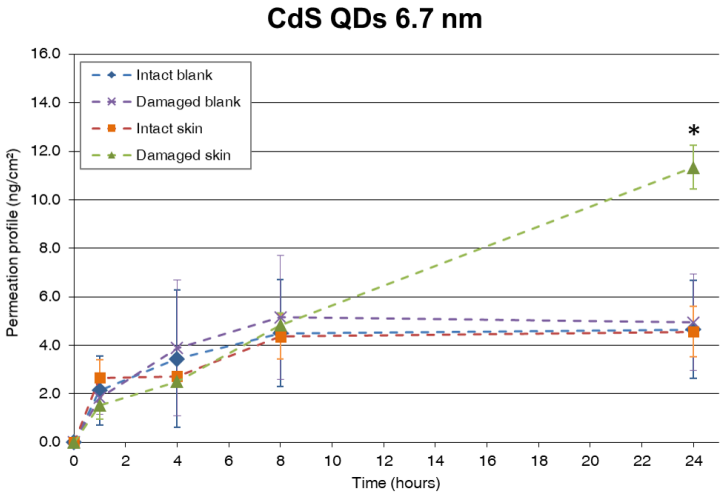

Figure 31 6.7 nm CdS QDs permeation (ng/cm²) in recipient compartment through intact and damaged skin after 1, 4, 8 and 24 h.

Table 14: CdS QDs permeation in recipient compartment through intact and damaged skin after 1, 4, 8 and 24 h. (*) mean p < 0.05 (Mann-Whitney test) with intact skin and blanks.

	Intact skin (ng/cm²)				Damaged skin (ng/cm²)			
Time (h)	Blank cells	3.4 nm	5.8 nm	6.7 nm	Blank cells	3.4 nm	5.8 nm	6.7 nm
1	2.13 ± 1.41	1.93 ± 0.05	1.95 ± 0.29	2.66 ± 0.73	1.83 ± 0.68	1.72 ± 0.64	1.92 ± 0.65	1.53 ± 0.59
4	3.44 ± 2.83	2.76 ± 0.73	2.53 ± 0.12	2.72 ± 0.10	3.89 ± 2.80	9.13 ± 6.02	3.63 ± 0.50	2.51 ± 0.12
8	4.49 ± 2.21	3.83 ± 0.17	5.25 ± 0.47	4.36 ± 0.92	5.15 ± 2.56	48.1 ± 22.6*	14.4 ± 4.9*	4.84 ± 0.50
24	4.65 ± 2.01	4.07 ± 0.20	13.7 ± 12.6	4.56 ± 1.05	4.95 ± 2.00	303 ± 135*	122 ± 64*	11.3 ± 0.9*

A comparison of size-dependent permeation in damaged skin was performed (Figure 32) and emerged a statistically significant difference in dermal permeation between the smallest (3.4 nm) and largest (6.7 nm) CdS quantum dots across damaged human skin at both 8 and 24 hours. At the 8-hour mark, 3.4 nm QDs exhibited cadmium accumulation nearly tenfold that of the 6.7 nm counterparts. This disparity becomes even more pronounced at 24 hours, where the Cd concentration for 3.4 nm particles reached 302.87 µg/cm² compared to only 11.34 µg/cm² for 6.7 nm particles. A significative difference was also observed when comparing 5.8 nm QDs with 6.7 QDs at 8 and 24 hours, indicating that even

relatively small changes in nanoparticle size can influence Cd penetration and accumulation in damaged tissue.

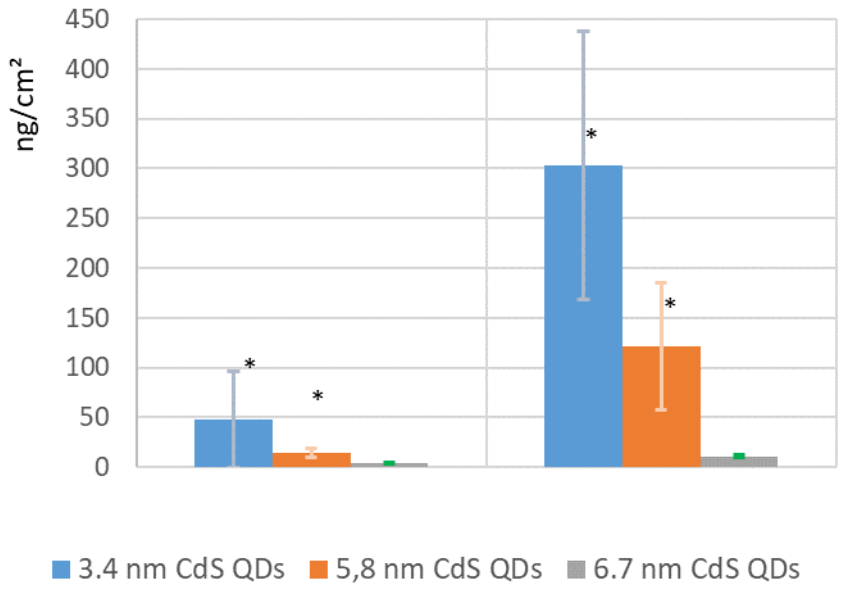

Figure 32: comparison of CdS QD permeation through damaged skin after 8 h and 24 h. (*) indicates p < 0.05 (Mann–Whitney test) between 3.4 nm and 5.8 nm CdS QDs compared with 6.7 nm CdS QDs.

Cd quantification in different skin layers highlighted that in intact skin, there was a modest but discernible accumulation of Cd within the epidermal and dermal layers for all tested QDs (table 15 and figure 33, 34 and 35).

The 3.4 nm CdS QDs exhibited the highest penetration among intact specimens, with a combined total of 0.51 µg/cm², while larger particles such as 6.7 nm QDs yielded significantly lower uptake (0.23 µg/cm²).

In intact skin, the layer-specific distribution of 3.4 nm CdS QDs revealed higher Cd accumulation in the epidermis (0.46 µg/cm²) than in the dermis (0.04 µg/cm²), indicating predominant retention of particles within the skin's outer barrier.

The most pronounced effect was observed under damaged skin conditions (figure 36). Here, the smallest QDs (3.4 nm) demonstrated higher penetration, with a total cadmium concentration of 6.31 µg/cm², significantly exceeding those of 5.8 nm and 6.7 nm QDs (3.06 and 0.59 µg/cm², respectively).

Table 15: Cd concentration (µg/cm²) in epidermis, dermis and full-thickness skin. Asterisks (*) indicate p < 0.05 (Mann-Whitney test) compared with blanks.

	Intact skin (µg/cm²)			Damaged skin (µg/cm²)
	epidermis	dermis	total	total
Blanks	0.004 ± 0.001	0.006 ± 0.001	0.011 ± 0.001	0.006 ± 0.001
3.4 nm	0.46 ± 0.34*	0.05 ± 0.01	0.51 ± 0.34*	6.31 ± 1.08*
5.8 nm	0.08 ± 0.02*	0.06 ± 0.01*	0.14 ± 0.02*	3.06 ± 2.03*
6.7 nm	0.15 ± 0.03*	0.08 ± 0.01*	0.23 ± 0.03*	0.59 ± 0.50

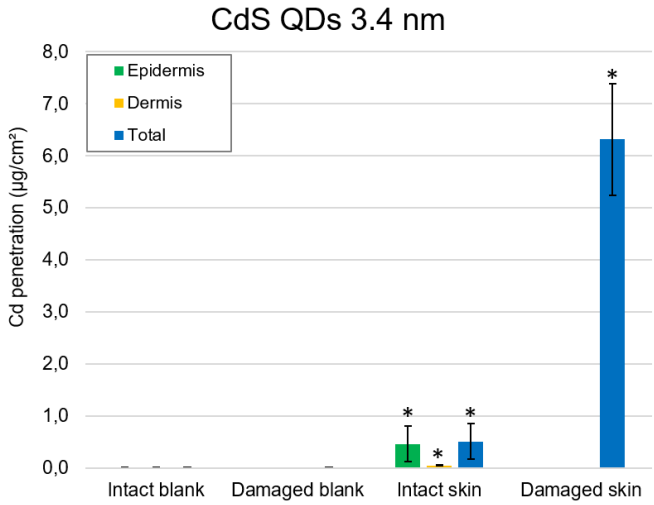

Figure 33: 3.4 nm CdS QDs penetration (µg/cm²) in epidermis, dermis and total skin.

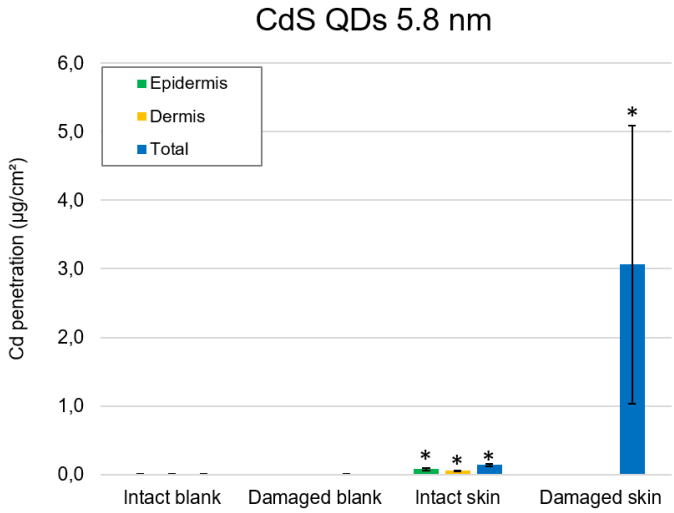

Figure 34: 5.8 nm CdS QDs penetration (µg/cm²) in epidermis, dermis and total skin

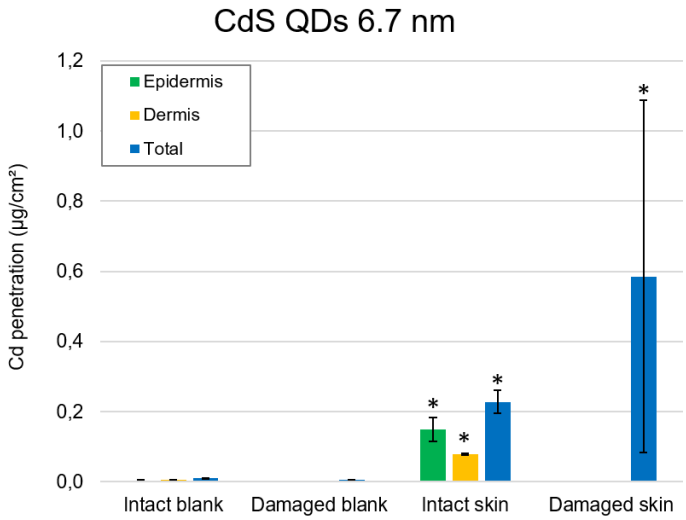

Figure 35: 6.7 nm CdS QDs penetration (µg/cm²) in epidermis, dermis and total skin.

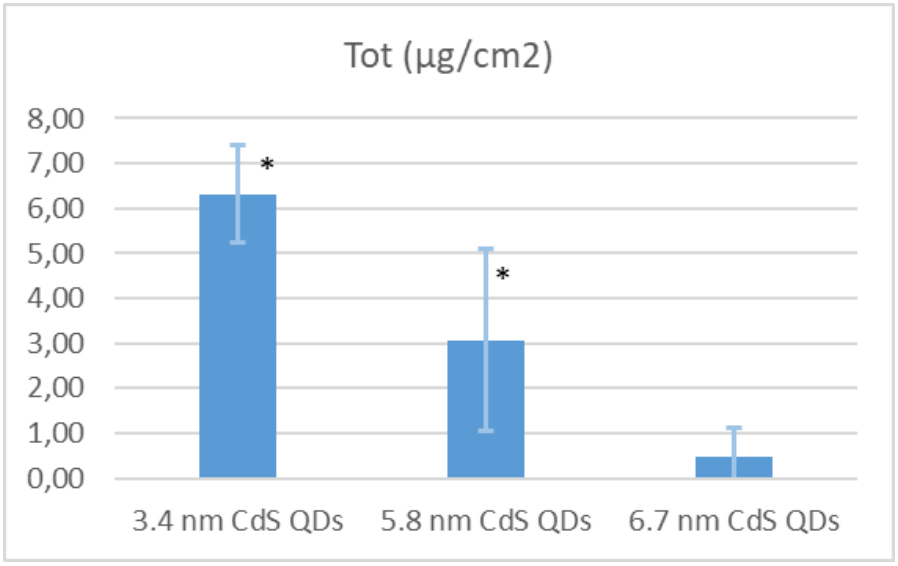

Figure 36: size comparison of CdS QDs concentration in damaged skin
** p < 0.05 Mann-Whitney Test between 3.4 nm and 5.8 CdS QDs with 6.7 nm CdS QDs*

4.3.2 FLUORESCENT SKIN CHARACTERIZATION

Transverse cross-sections of the skin samples following the Franz diffusion cell study were analyzed using the ZOE™ Fluorescent Cell Imager (Bio-Rad) to qualitatively confirm the permeation and localization of the CdS QDs. Distinct fluorescence, characteristic of the CdS core emission, was observed within the viable skin layers. This fluorescence signal was primarily localized in the epidermal

layer. Notably, higher fluorescence was significantly more visible in samples where the skin barrier was damaged (figures 37, 38, 39 and 43). Furthermore, the fluorescence signal was visibly more intense and marked in the samples treated with the 3.4 nm CdS QDs, aligning with the quantitative analysis of higher total accumulation. No signal from CdS QDs was detected in blank samples used as comparison (figure 44 - 45).

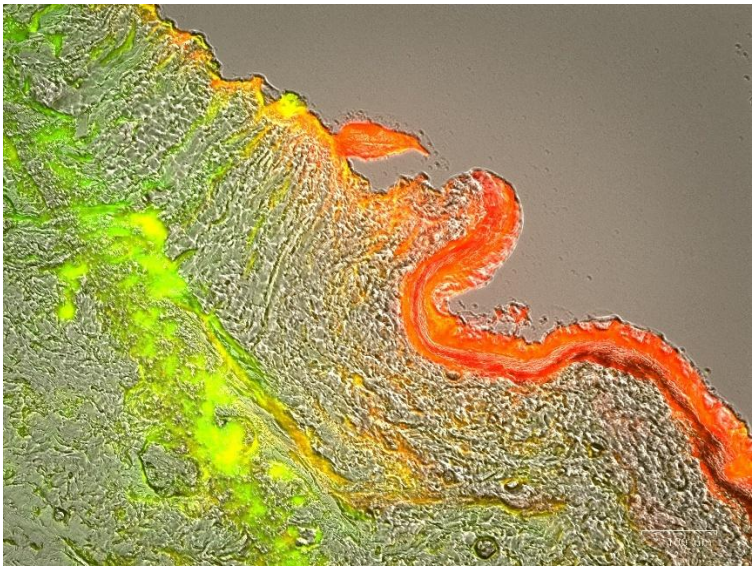

Figure 37: fluorescent skin imaging for 3.4 nm CdS QDs sample in damaged skin–100 µm scale

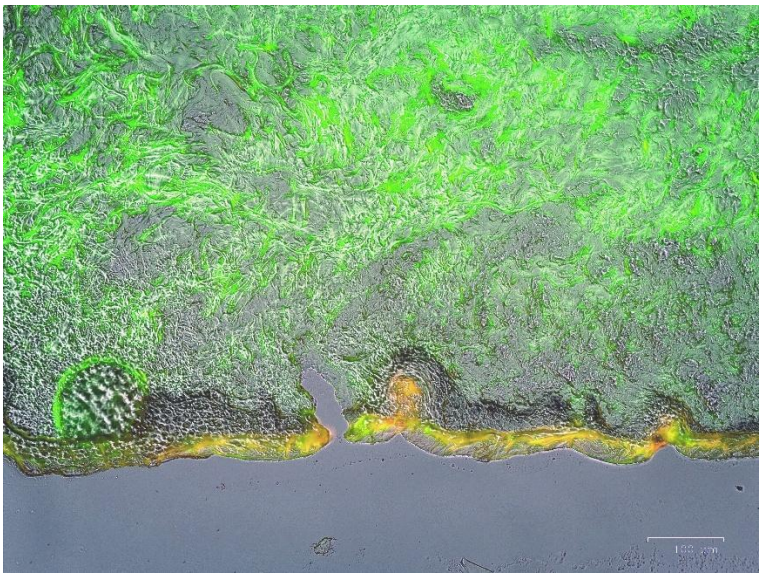

Figure 38: fluorescent skin imaging for 5.8 nm CdS QDs sample in damaged skin –100 µm scale

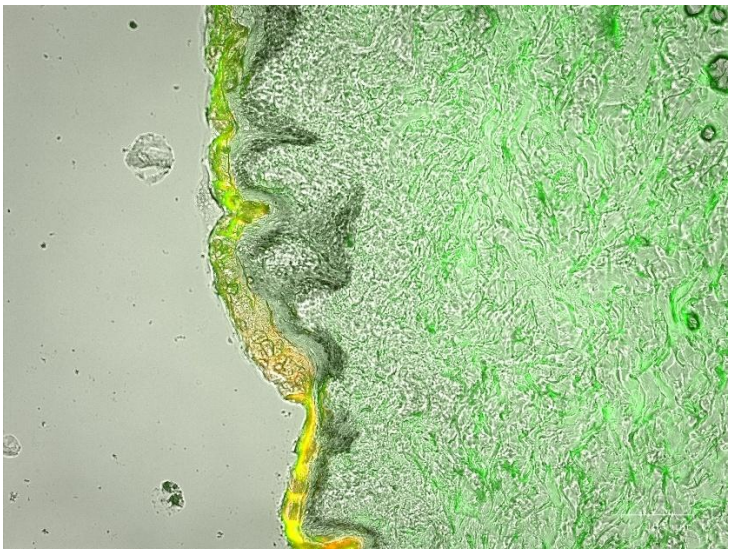

Figure 39: fluorescent skin imaging for 6.7 nm CdS QDs sample in damaged skin –100 µm scale

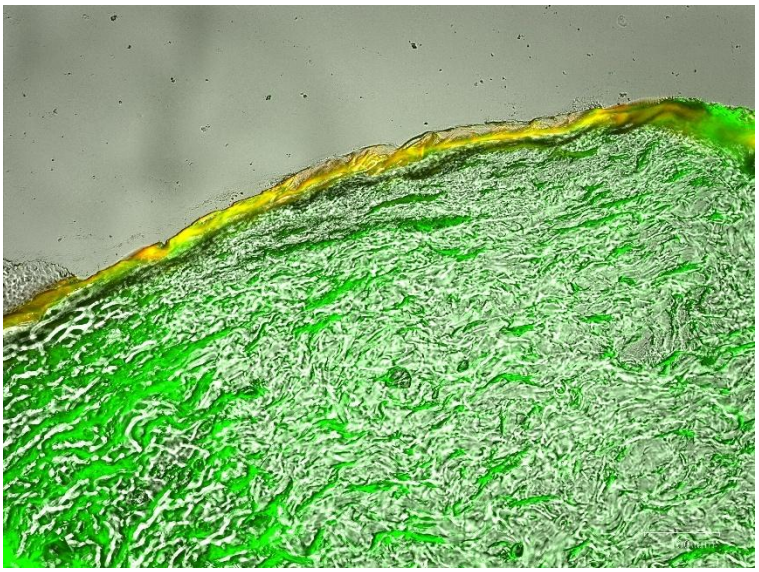

Figure 40: fluorescent skin imaging for 3.4 nm CdS QDs sample in intact skin–100 µm scale

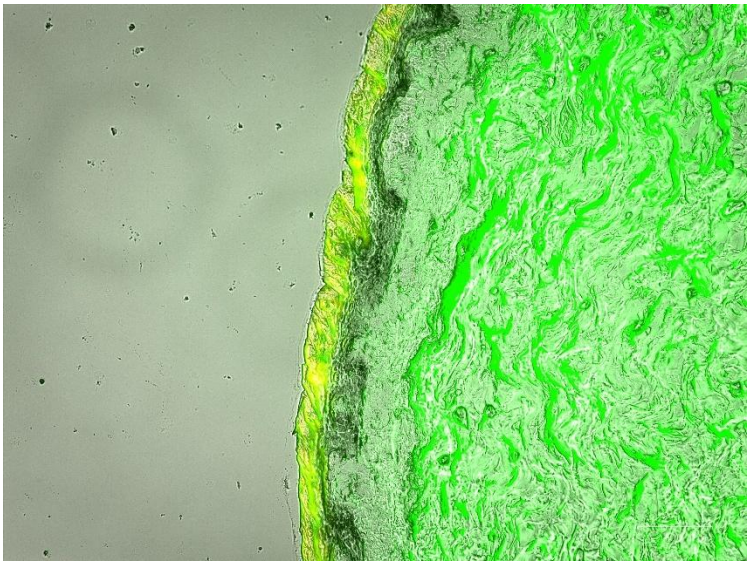

Figure 41: fluorescent skin imaging for 5.8 nm CdS QDs sample in intact skin –100 µm scale

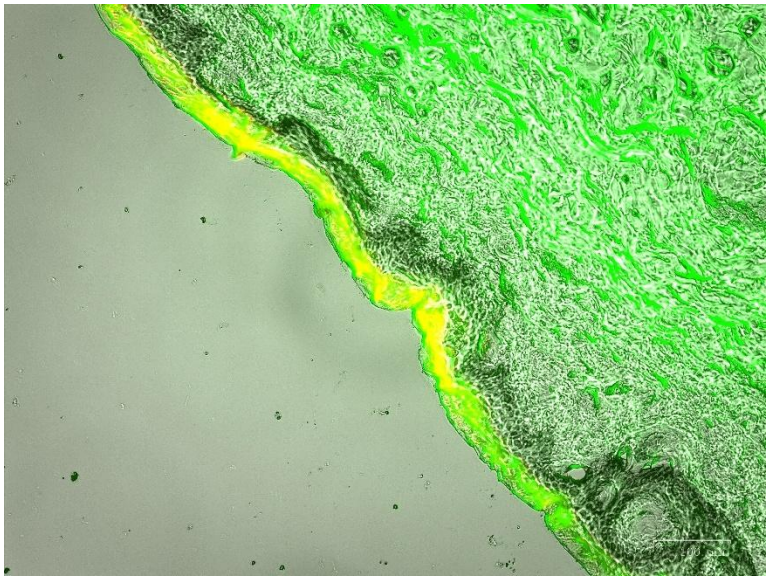

Figure 42: fluorescent skin imaging for 6.7 nm CdS QDs sample in intact skin –100 µm scale

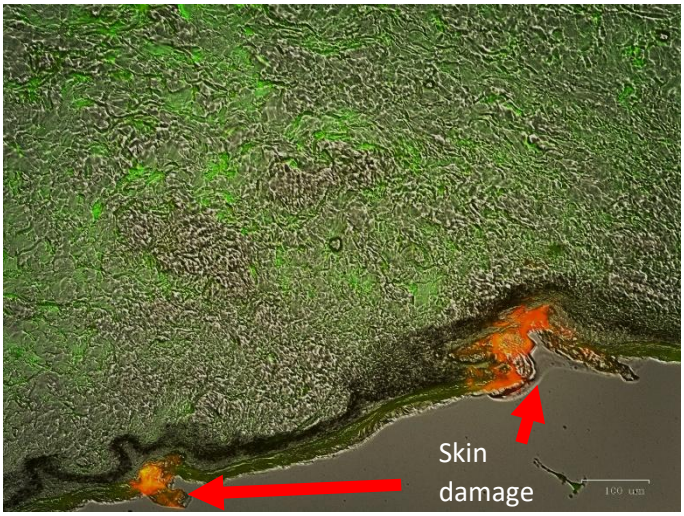

Figure 43: fluorescent skin imaging for 3.4 nm CdS QDs sample in damaged skin –100 µm scale

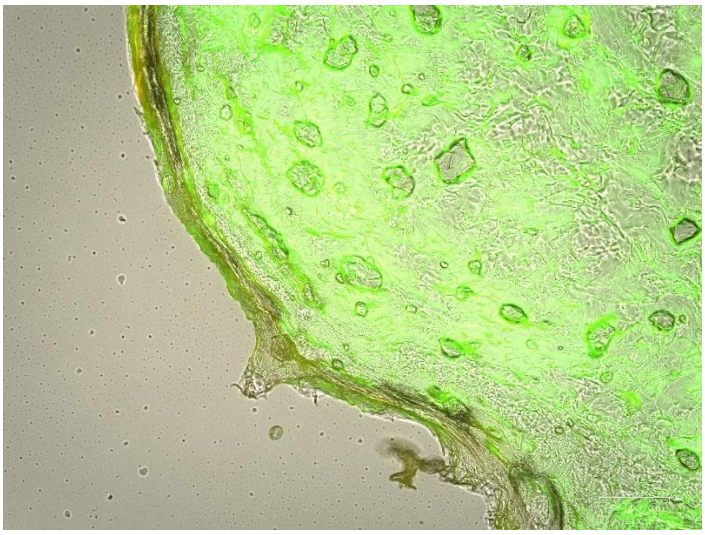

Figure 44: fluorescent skin imaging for blank skin sample - damaged skin– 100 µm scale

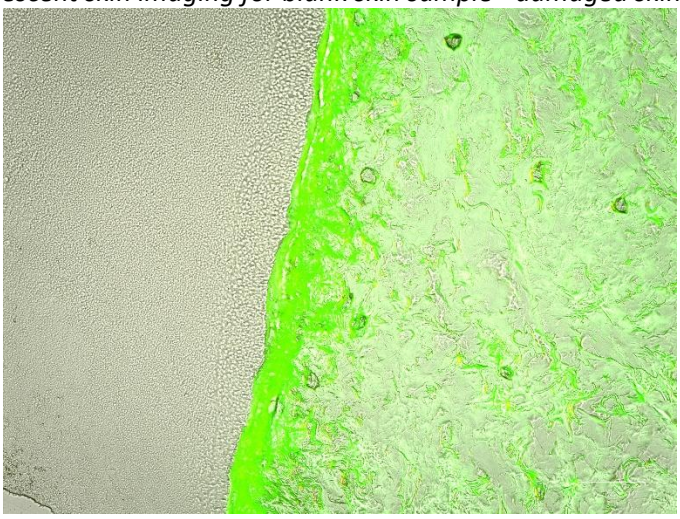

Figure 45: fluorescent skin imaging for blank skin sample - intact skin– 100 µm scale

4.4 DISCUSSION

This study provides a detailed exploration into the transdermal behavior of cadmium sulfide quantum dots (CdS QDs), elucidating the critical influence of particle size and skin barrier integrity on their permeation.

Findings align with the established nanotoxicological principle that intact skin provides a highly effective barrier against the percutaneous penetration of nanoparticles (Larese Filon et al. 2015; Larese Filon, Crosera, et al. 2016), including quantum dots.

CdS QDs showed minimal Cd levels in receptor fluids when applied to intact skin—suggesting a retention within the superficial epidermal layers. This observation is reinforced by quantitative tissue analysis, which revealed trace cadmium accumulation predominantly in the epidermis, and negligible diffusion into the dermis. These findings align with previous literature (Gopee et al. 2009; Gratieri et al. 2010) which reported that QDs tend to accumulate in outer skin layers without deep tissue penetration under normal barrier conditions. The greatest cadmium accumulation within the epidermal layer was observed for the smallest CdS quantum dots (3.4 nm), underscoring their increased tendency to penetrate the outermost skin barrier compared to larger particles. This finding reinforces the notion that reduced nanoparticle dimensions significantly enhance transdermal access. This accumulation within the epidermis, despite limited systemic absorption, still represents a localized exposure scenario that may contribute to dermal toxicity with recurrent or extended contact.

However, when the skin barrier was compromised, a significative increase in Cd permeation was observed, resulting consistent with previous studies (Monteiro-Riviere and Zhang 2009; Gratieri et al. 2010). The physical disruption of the stratum corneum likely created direct pathways for the CdS QDs to bypass the primary diffusion-limiting layer, allowing for enhanced uptake into the viable epidermis and subsequent diffusion into the receptor fluid. While intact skin may offer a robust defense against CdS QDs, any situation that leads to a compromised skin barrier—such as minor abrasions, cuts, or

dermatological disorders—could increase the risk of systemic exposure (Crosera et al. 2009; Larese Filon 2017).

The ZOE™ Fluorescent Cell Imager (Bio-Rad) qualitatively demonstrated the penetration and distribution of CdS quantum dots, showing predominant localization within the epidermal layer. In compromised skin samples, higher penetration was also observed. Fluorescence intensity was notably higher in tissues treated with 3.4 nm CdS QDs, corroborating quantitative findings of increased overall accumulation.

The observed size-dependent trend, where the smallest 3.4 nm QDs demonstrated the highest level of absorption, is consistent with the principles of quantum dot toxicokinetics (Mo et al. 2017). Due to their larger surface-area-to-volume ratio, smaller CdS QDs display enhanced chemical reactivity and an increased propensity for cadmium ion (Cd^{2+}) release—one of the primary mechanisms of toxicity.

These results are consistent with the findings by Prow et al. (Prow et al. 2012), which investigated the penetration behavior of quantum dots in viable human skin, highlighting that quantum dots predominantly accumulated in the stratum corneum and upper epidermis, with limited penetration into the dermis observed only in compromised skin conditions.

A significant disparity in Cd permeation emerged also when comparing 5.8 nm and 6.7 nm QDs at both 8 and 24 hours post-exposure. These results suggest that even subtle variations in nanoparticle size can influence transdermal Cd penetration, with the extent of accumulation further modulated by exposure duration.

This time-dependent behavior indicates that smaller QDs may sustain higher levels of tissue infiltration over prolonged periods, especially under compromised skin conditions This characteristic contributes to their heightened likelihood of penetrating compromised skin barriers, subsequently reaching the underlying dermal layers and diffusing into the receptor fluid, with consequent systemic exposure and potential toxicological outcomes.

4.5 CONCLUSION

In conclusion, our ex-vivo investigation using human skin and Franz diffusion cells demonstrates that the integrity of the epidermal barrier is the most critical factor in controlling the dermal absorption of CdS QDs. While intact skin effectively prevents systemic permeation, it still allows for some localized retention of QDs within the epidermis. However, even minor damage to the skin barrier leads to a significant, size-dependent increase in both permeation into the receptor fluid and accumulation within the skin tissue itself. The smallest (3.4 nm) QDs showed the highest degree of penetration, underscoring the importance of particle size in nanotoxicology. These findings have significant implications for risk assessment, suggesting that individuals with compromised skin may be at a substantially higher risk of systemic exposure to Cd from CdS QDs. Future research should investigate the long-term biological effects of both epidermal retention and systemic permeation, as well as the mechanisms by which these CdS QDs induce toxicity in skin and target organs.

5. CONLUSION OF THE THESIS

This doctoral research investigated occupational exposure to gallium arsenide (GaAs) and cadmium sulfide (CdS) nanoparticles, aiming to assess exposure scenarios encountered during laboratory-based research activities.

The comprehensive occupational exposure assessment conducted in the GaAs research facility utilizing Molecular Beam Epitaxy (MBE) technology revealed a complex exposure setting characterized by generally controlled baseline conditions punctuated by significant transient exposure events. Real-time monitoring using the DiSCMini instrument demonstrated that while modern engineering controls—including local exhaust ventilation, fume hoods, and HEPA filtration systems—effectively maintain low background nanoparticle concentrations during routine laboratory operations, specific

mechanical processes generate substantial exposure risks. Wafer cutting operations, in particular, produced particle number concentration peaks reaching 88883 particles/cm³, representing an increase of nearly two orders of magnitude above baseline levels. Although these peaks were brief and confined by ventilation systems, they represent critical moments of potential inhalation exposure that request specific risk mitigation strategies.

Environmental monitoring using IOM samplers confirmed that weekly average airborne concentrations of gallium (118.07 ng/m³) and arsenic (44.58 ng/m³) remained well below established occupational exposure limits, with the highest arsenic concentration detected being approximately 68-fold lower than the ACGIH TLV-TWA. However, the presence of these elements in air samples, combined with their detection in biological specimens, confirms that GaAs particle generation and worker exposure occur despite protective measures. Surface contamination analysis revealed substantial and progressive accumulation of GaAs-derived particles on laboratory surfaces throughout the workweek, with peak concentrations observed inside fume hoods (Ga: 3308 ng/cm²; As: 1418 ng/cm²) and on laboratory floors (Ga: 3014 ng/cm²; As: 251 ng/cm²). The detection of contamination on personal protective equipment, including FFP3 respirators (Ga: 208 ng/cm²; As: 57.8 ng/cm²), demonstrates that particle dispersion extends beyond the immediate work area and highlights the importance of proper PPE management protocols.

Biological monitoring provided direct evidence of systemic arsenic absorption, with urinary arsenic concentrations averaging 19.5 µg/L—exceeding the reference range for non-occupationally exposed populations (2.0–15 µg/L) but generally remaining below the occupational threshold (30 µg/L). These findings demonstrate that despite engineering controls and PPE, episodic overexposure can occur, underscoring the necessity for continuous biomonitoring programs in facilities handling arsenide-containing nanomaterials.

The implementation of enhanced safety protocols resulted in statistically significant reductions across all exposure metrics. The multi-barrier approach—encompassing mandatory PPE usage (disposable laboratory coats, nitrile gloves, FFP3 respirators), controlled laboratory access with decontamination

mats, localized containment during high-risk operations using disposable absorbent materials, and intensified cleaning protocols (daily surface decontamination plus weekly deep cleaning)—proved highly effective. Surface contamination decreased by over 90% in most monitored areas, with particularly significant reductions on FFP3 masks (As: 97% reduction; Ga: 99.7% reduction) and at laboratory entry points. Dermal exposure, assessed via tape stripping, showed even more impressive reductions, with post-shift skin contamination decreasing by approximately 95% for arsenic and over 99% for gallium. These quantitative results validate the efficacy of systematically applied occupational hygiene measures and provide an evidence-based framework for risk management in nanomaterial handling facilities.

The ex-vivo Franz diffusion cell studies provided insights into the dermal absorption potential of both GaAs particles and CdS quantum dots. Results conclusively demonstrated that intact human skin constitutes an effective barrier against nanoparticle penetration, with minimal cadmium or arsenic detected in receptor fluids under physiological conditions. However, mechanical barrier disruption—simulating occupational scenarios involving microabrasions, cuts, or dermatological conditions—resulted in substantial increases in percutaneous absorption for both materials studied.

For GaAs, differential permeation was observed between constituent elements, with arsenic exhibiting significantly higher skin permeability than gallium, likely reflecting differences in ionic size, solubility, and chemical speciation in the dermal environment.

For CdS QDs, a pronounced size-dependent effect was observed, with 3.4 nm particles demonstrating cumulative cadmium concentrations of 302.87 μg/cm² through damaged skin after 24 hours, compared to 121.56 μg/cm² for 5.8 nm particles and only 11.34 μg/cm² for 6.7 nm particles. This inverse relationship between particle size and absorption underscores the heightened toxicological concern associated with smaller engineered nanomaterials.

These findings carry important implications for occupational health practice and preventive measures. They emphasize the critical importance of maintaining skin integrity through appropriate protective measures and prompt treatment of minor injuries, implementing proper decontamination procedures

that do not compromise the skin barrier, developing size-specific risk assessments that account for enhanced penetration of smaller nanoparticles, and establishing regular biomonitoring programs capable of detecting episodic exposures that may be missed by environmental monitoring alone.

Future research should investigate the chronic health effects of repeated low-dose exposure to metal NPs, establish standardized biomonitoring protocols with appropriate biological exposure indices and examine the long-term fate of dermally absorbed metal NPs and their potential for bioaccumulation.

6. BIBLIOGRAPHY

Abdal Dayem, Ahmed, Mohammed Kawser Hossain, Soo Bin Lee, et al. 2017. 'The Role of Reactive Oxygen Species (ROS) in the Biological Activities of Metallic Nanoparticles'. *International Journal of Molecular Sciences* 18 (1): 1. https://doi.org/10.3390/ijms18010120.

Akter, Mst. Sathi, Mahtab U. Ahmmed, Nilufer Yesmin Tanisa, and Shakib Hossain. 2024. 'Deposition of Nanoparticles through a Cylindrical Tube of Human Respiratory System'. *AIP Advances* 14 (12): 125320. https://doi.org/10.1063/5.0239676.

Angelé-Martínez, Carlos, Khanh Van T. Nguyen, Fathima S. Ameer, Jeffrey N. Anker, and Julia L. Brumaghim. 2017. 'Reactive Oxygen Species Generation by Copper(II) Oxide Nanoparticles Determined by DNA Damage Assays and EPR Spectroscopy'. *Nanotoxicology* 11 (2): 278–88. https://doi.org/10.1080/17435390.2017.1293750.

Attarilar, Shokouh, Jinfan Yang, Mahmoud Ebrahimi, et al. 2020. 'The Toxicity Phenomenon and the Related Occurrence in Metal and Metal Oxide Nanoparticles: A Brief Review From the Biomedical Perspective'. *Frontiers in Bioengineering and Biotechnology* 8 (July). https://doi.org/10.3389/fbioe.2020.00822.

Badir, Amina, Siham Refki, and Zouheir Sekkat. 2025. 'Utilizing Gold Nanoparticles in Plasmonic Photothermal Therapy for Cancer Treatment'. *Heliyon* 11 (4): e42738. https://doi.org/10.1016/j.heliyon.2025.e42738.

Bau, S., B. Zimmermann, R. Payet, and O. Witschger. 2015. 'A Laboratory Study of the Performance of the Handheld Diffusion Size Classifier (DiSCmini) for Various Aerosols in the 15–400 Nm Range'. *Environmental Science: Processes & Impacts* 17 (2): 261–69. https://doi.org/10.1039/C4EM00491D.

Biasiol G., Sorba L. 2001. 'Molecular Beam Epitaxy: Principles and Applications'. In *Crystal Growth of Materials for Energy Production and Energy-Saving Applications*. Edizioni ETS. https://www.academia.edu/7041590/MOLECULAR_BEAM_EPITAXY_PRINCIPLES_AND_APPLICATIONS.

Bomhard, Ernst M. 2020. 'The Toxicology of Gallium Oxide in Comparison with Gallium Arsenide and Indium Oxide'. *Environmental Toxicology and Pharmacology* 80 (November): 103437. https://doi.org/10.1016/j.etap.2020.103437.

Bomhard, Ernst M., Heinz-Peter Gelbke, Hermann Schenk, Gary M. Williams, and Samuel M. Cohen. 2013. 'Evaluation of the Carcinogenicity of Gallium Arsenide'. *Critical Reviews in Toxicology* 43 (5): 436–66. https://doi.org/10.3109/10408444.2013.792329.

Borm, Paul J. A., David Robbins, Stephan Haubold, et al. 2006. 'The Potential Risks of Nanomaterials: A Review Carried out for ECETOC'. *Particle and Fibre Toxicology* 3 (August): 11. https://doi.org/10.1186/1743-8977-3-11.

Braakhuis, Hedwig M., Margriet VDZ Park, Ilse Gosens, Wim H. De Jong, and Flemming R. Cassee. 2014. 'Physicochemical Characteristics of Nanomaterials That Affect Pulmonary Inflammation'. *Particle and Fibre Toxicology* 11 (1): 18. https://doi.org/10.1186/1743-8977-11-18.

Bronaugh, Robert L., and Raymond F. Stewart. 1985. 'Methods for In Vitro Percutaneous Absorption Studies V: Permeation Through Damaged Skin'. *Journal of Pharmaceutical Sciences* 74 (10): 1062–66. https://doi.org/10.1002/jps.2600741008.

Brouwer, Derk H., Suzanne Spaan, Martin Roff, et al. 2016. 'Occupational Dermal Exposure to Nanoparticles and Nano-Enabled Products: Part 2, Exploration of Exposure Processes and Methods of Assessment'. *International Journal of Hygiene and Environmental Health* 219 (6): 503–12. https://doi.org/10.1016/j.ijheh.2016.05.003.

Carter, Dean E., H. Vasken Aposhian, and A. Jay Gandolfi. 2003. 'The Metabolism of Inorganic Arsenic Oxides, Gallium Arsenide, and Arsine: A Toxicochemical Review'. *Toxicology and Applied Pharmacology* 193 (3): 309–34. https://doi.org/10.1016/j.taap.2003.07.009.

Chen, H.-W. 2007. 'Exposure and Health Risk of Gallium, Indium, and Arsenic from Semiconductor Manufacturing Industry Workers'. *Bulletin of Environmental Contamination and Toxicology* 78 (2): 123–27. https://doi.org/10.1007/s00128-007-9079-9.

Chen, Sai-Juan, Xiao-Jing Yan, and Zhu Chen. 2013. 'Arsenic in Tissues, Organs, and Cells'. In *Encyclopedia of Metalloproteins*. Springer, New York, NY. https://doi.org/10.1007/978-1-4614-1533-6_491.

Creutzenberg, Otto, Gerhard Pohlmann, Dirk Schaudien, and Heiko Kock. 2022. 'Toxicokinetics of Nanoparticles Deposited in Lungs Using Occupational Exposure Scenarios'. *Frontiers in Public Health* 10: 909247. https://doi.org/10.3389/fpubh.2022.909247.

Crosera, Matteo, Gianpiero Adami, Marcella Mauro, Massimo Bovenzi, Elena Baracchini, and Francesca Larese Filon. 2016. 'In Vitro Dermal Penetration of Nickel Nanoparticles'. *Chemosphere* 145 (February): 301–6. https://doi.org/10.1016/j.chemosphere.2015.11.076.

Crosera, Matteo, Massimo Bovenzi, Giovanni Maina, et al. 2009. 'Nanoparticle Dermal Absorption and Toxicity: A Review of the Literature'. *International Archives of Occupational and Environmental Health* 82 (9): 1043–55. https://doi.org/10.1007/s00420-009-0458-x.

Cruz, Gerardo González De la, Lourdes Rodríguez-Fragoso, Patricia Rodríguez-Fragoso, et al. 2024. 'Toxicity of Quantum Dots'. In *Toxicity of Nanoparticles - Recent Advances and New Perspectives*. IntechOpen. https://doi.org/10.5772/intechopen.112073.

Davies, D. J., R. J. Ward, and J. R. Heylings. 2004. 'Multi-Species Assessment of Electrical Resistance as a Skin Integrity Marker for in Vitro Percutaneous Absorption Studies'. *Toxicology in Vitro: An International Journal Published in Association with BIBRA* 18 (3): 351–58. https://doi.org/10.1016/j.tiv.2003.10.004.

Demir, Eşref. 2021. 'A Review on Nanotoxicity and Nanogenotoxicity of Different Shapes of Nanomaterials'. *Journal of Applied Toxicology* 41 (1): 118–47. https://doi.org/10.1002/jat.4061.

Diakonov, Igor I., Gleb S. Pokrovski, Pascale Bénézeth, Jacques Schott, Jean-Louis Dandurand, and Jocelyne Escalier. 1997. 'Gallium Speciation in Aqueous Solution. Experimental Study and Modelling: Part 1. Thermodynamic Properties of Ga(OH)4− to 300°C'. *Geochimica et Cosmochimica Acta* 61 (7): 1333–43. https://doi.org/10.1016/S0016-7037(97)00011-2.

Dutkiewicz, T. 1977. 'Experimental Studies on Arsenic Absorption Routes in Rats'. *Environmental Health Perspectives* 19 (August): 173–76. https://doi.org/10.1289/ehp.7719173.

Ergün, Recai, Ender Evcik, Dilek Ergün, Begüm Ergan, Esin Özkan, and Özge Gündüz. 2017. 'High-Resolution Computed Tomography and Pulmonary Function Findings of Occupational Arsenic Exposure in Workers'. *Balkan Medical Journal* 34 (3): 263–68. https://doi.org/10.4274/balkanmedj.2016.0795.

Fadhil, Eman A. A., Manal M. Abdullah, and Fadhel M. Lafta. 2024. 'Preparation of N-A Cysteine-Capped CdTe/CdS/ZnS Core/Shell/Shell QDs as a Selective Probe for Detecting Damaged DNA'. *International Journal of Nanoscience* 23 (02): 2350061. https://doi.org/10.1142/S0219581X23500618.

Fallah, Sina, Elham Yusefi-Tanha, and Jose R. Peralta-Videa. 2024. 'Interaction of Nanoparticles and Reactive Oxygen Species and Their Impact on Macromolecules and Plant Production'. *Plant Nano Biology* 10 (November): 100105. https://doi.org/10.1016/j.plana.2024.100105.

Fang, S., K. Adomi, S. Iyer, et al. 1990. 'Gallium Arsenide and Other Compound Semiconductors on Silicon'. *Journal of Applied Physics* 68 (November): R31–58. https://doi.org/10.1063/1.346284.

Fasano, W. J., L. A. Manning, and J. W. Green. 2002. 'Rapid Integrity Assessment of Rat and Human Epidermal Membranes for in Vitro Dermal Regulatory Testing: Correlation of Electrical Resistance with Tritiated Water Permeability'. *Toxicology in Vitro: An International Journal Published in Association with BIBRA* 16 (6): 731–40. https://doi.org/10.1016/s0887-2333(02)00084-x.

Fierz, M., C. Houle, P. Steigmeier, and H. Burtscher. 2011. 'Design, Calibration, and Field Performance of a Miniature Diffusion Size Classifier'. *Aerosol Science and Technology*, January 1. world. https://www.tandfonline.com/doi/abs/10.1080/02786826.2010.516283.

Filon, Francesca Larese, Mark Boeniger, Giovanni Maina, Gianpiero Adami, Paolo Spinelli, and Adriano Damian. 2006. 'Skin Absorption of Inorganic Lead (PbO) and the Effect of Skin Cleansers'. *Journal of Occupational and Environmental Medicine* 48 (7): 692–99. https://doi.org/10.1097/01.jom.0000214474.61563.1c.

Filon, Francesca Larese, Flavia D'Agostin, Matteo Crosera, Gianpiero Adami, Massimo Bovenzi, and Giovanni Maina. 2009. 'In Vitro Absorption of Metal Powders through Intact and Damaged Human Skin'. *Toxicology in Vitro: An International Journal Published in Association with BIBRA* 23 (4): 574–79. https://doi.org/10.1016/j.tiv.2009.01.015.

Flora, Swaran J S. 2000. 'Possible Health Hazards Associated with the Use of Toxic Metals in Semiconductor Industries'. *Journal of Occupational Health* 42 (3): 105–10. https://doi.org/10.1539/joh.42.105.

Flora, Swaran J. S., Kapil Bhatt, and Ashish Mehta. 2009. 'Arsenic Moiety in Gallium Arsenide Is Responsible for Neuronal Apoptosis and Behavioral Alterations in Rats'. *Toxicology and Applied Pharmacology*, Toxicants and Neurodegenerative Diseases, vol. 240 (2): 236–44. https://doi.org/10.1016/j.taap.2009.05.013.

Foroozandeh, Parisa, and Azlan Abdul Aziz. 2018. 'Insight into Cellular Uptake and Intracellular Trafficking of Nanoparticles'. *Nanoscale Research Letters* 13 (1): 339. https://doi.org/10.1186/s11671-018-2728-6.

Franz, T. J. 1975. 'Percutaneous Absorption on the Relevance of in Vitro Data'. *The Journal of Investigative Dermatology* 64 (3): 190–95. https://doi.org/10.1111/1523-1747.ep12533356.

Frey, Andreas, Katrin Ramaker, Niels Röckendorf, et al. 2019. 'Fate and Translocation of (Nano)Particulate Matter in the Gastrointestinal Tract'. In *Biological Responses to Nanoscale Particles: Molecular and Cellular Aspects and Methodological Approaches*, edited by Peter Gehr and Reinhard Zellner. Springer International Publishing. https://doi.org/10.1007/978-3-030-12461-8_12.

Fujihara, Junko, and Naoki Nishimoto. 2021. 'Dermal Absorption of Gallium Antimonide *in Vitro* and pro-Inflammatory Effects on Human Dermal Fibroblasts'. *Toxicology in Vitro* 71 (March): 105064. https://doi.org/10.1016/j.tiv.2020.105064.

Galey, Louis, Sabyne Audignon, Patrick Brochard, et al. 2023. 'Strategies to Assess Occupational Exposure to Airborne Nanoparticles: Systematic Review and Recommendations'. *Safety and Health at Work* 14 (2): 163. https://doi.org/10.1016/j.shaw.2023.02.002.

Ganguly, Priyanka, Ailish Breen, and Suresh C. Pillai. 2018. 'Toxicity of Nanomaterials: Exposure, Pathways, Assessment, and Recent Advances'. *ACS Biomaterials Science & Engineering* 4 (7): 2237–75. https://doi.org/10.1021/acsbiomaterials.8b00068.

Gatoo, Manzoor Ahmad, Sufia Naseem, Mir Yasir Arfat, Ayaz Mahmood Dar, Khusro Qasim, and Swaleha Zubair. 2014. 'Physicochemical Properties of Nanomaterials: Implication in Associated Toxic Manifestations'. *BioMed Research International* 2014 (1): 498420. https://doi.org/10.1155/2014/498420.

Geiser, Marianne, and Wolfgang G. Kreyling. 2010. 'Deposition and Biokinetics of Inhaled Nanoparticles'. *Particle and Fibre Toxicology* 7 (1): 2. https://doi.org/10.1186/1743-8977-7-2.

Ghazi, Rizwana, Talib K. Ibrahim, Jamal Abdul Nasir, et al. 2025. 'Iron Oxide Based Magnetic Nanoparticles for Hyperthermia, MRI and Drug Delivery Applications: A Review'. *RSC Advances* 15 (15): 11587–616. https://doi.org/10.1039/d5ra00728c.

Gondre-Lewis, Timothy A., Constance B. Hartmann, Rebecca E. Caffrey, and Kathleen L. McCoy. 2003. 'Gallium Arsenide Exposure Impairs Splenic B Cell Accessory Function'. *International Immunopharmacology* 3 (3): 403–15. https://doi.org/10.1016/S1567-5769(03)00007-9.

González-Fernández, Sara, Noelia Blanco-Agudín, David Rodríguez, Iván Fernández-Vega, Jesús Merayo-Lloves, and Luis M. Quirós. 2025. 'Silver Nanoparticles: A Versatile Tool Against Infectious and Non-Infectious Diseases'. *Antibiotics (Basel, Switzerland)* 14 (3): 289. https://doi.org/10.3390/antibiotics14030289.

Gopee, Neera V., Dean W. Roberts, Peggy Webb, et al. 2007. 'Migration of Intradermally Injected Quantum Dots to Sentinel Organs in Mice'. *Toxicological Sciences* 98 (1): 249–57. https://doi.org/10.1093/toxsci/kfm074.

Gopee, Neera V., Dean W. Roberts, Peggy Webb, et al. 2009. 'Quantitative Determination of Skin Penetration of PEG-Coated CdSe Quantum Dots in Dermabraded but Not Intact SKH-1 Hairless Mouse Skin'. *Toxicological Sciences: An Official Journal of the Society of Toxicology* 111 (1): 37–48. https://doi.org/10.1093/toxsci/kfp139.

Gratieri, Taís, Ulrich F. Schaefer, Lihong Jing, et al. 2010. 'Penetration of Quantum Dot Particles through Human Skin'. *Journal of Biomedical Nanotechnology* 6 (5): 586–95. https://doi.org/10.1166/jbn.2010.1155.

Guth, Katharina, Monika Schäfer-Korting, Eric Fabian, Robert Landsiedel, and Ben van Ravenzwaay. 2015. 'Suitability of Skin Integrity Tests for Dermal Absorption Studies in Vitro'. *Toxicology in Vitro* 29 (1): 113–23. https://doi.org/10.1016/j.tiv.2014.09.007.

Ham, Seunghon, Naroo Lee, Igchun Eom, et al. 2016. 'Comparison of Real Time Nanoparticle Monitoring Instruments in the Workplaces'. *Safety and Health at Work* 7 (4): 381–88. https://doi.org/10.1016/j.shaw.2016.08.001.

Hanlon, James, Karen S. Galea, and Steven Verpaele. 2021. 'Review of Workplace Based Aerosol Sampler Comparison Studies, 2004–2020'. *International Journal of Environmental Research and Public Health* 18 (13): 13. https://doi.org/10.3390/ijerph18136819.

Hartmann, Constance B., M. Travis Harrison, and Kathleen L. McCoy. 2005. 'Immunotoxicity of Gallium Arsenide on Antigen Presentation: Comparative Study of Intratracheal and Intraperitoneal Exposure Routes'. *Journal of Immunotoxicology* 2 (1): 1–9. https://doi.org/10.1080/15476910590930083.

Hethnawi, Afif, Osama Kashif, Robin Jeong, et al. 2023. 'Green Synthesis of Novel Titanomagnetite Nanoparticles for Oil Spill Cleanup'. *Colloids and Surfaces A: Physicochemical and Engineering Aspects* 664 (May): 131191. https://doi.org/10.1016/j.colsurfa.2023.131191.

Huy, Tran Q., Pham T.M. Huyen, Anh-Tuan Le, and Matteo Tonezzer. 2020. 'Recent Advances of Silver Nanoparticles in Cancer Diagnosis and Treatment'. *Anti-Cancer Agents in Medicinal Chemistry* 20 (11): 1276–87. https://doi.org/10.2174/1871520619666190710121727.

Ichihara, Sahoko. 2025. 'Effects of Engineered Nanomaterials on the Cardiovascular System'. *Journal of Occupational Health* 67 (1): uiae080. https://doi.org/10.1093/joccuh/uiae080.

'ISO 80004-1:2023(En), Nanotechnologies – Vocabulary — Part 1: Core Vocabulary'. n.d. Accessed 6 March 2025. https://www.iso.org/obp/ui/en/#iso:std:iso:80004:-1:ed-1:v1:en.

'ISO/TS 21623:2017(En), Workplace Exposure — Assessment of Dermal Exposure to Nano-Objects and Their Aggregates and Agglomerates (NOAA)'. n.d. Accessed 16 June 2025. https://www.iso.org/obp/ui#iso:std:iso:ts:21623:ed-1:v1:en.

Joudeh, Nadeem, and Dirk Linke. 2022. 'Nanoparticle Classification, Physicochemical Properties, Characterization, and Applications: A Comprehensive Review for Biologists'. *Journal of Nanobiotechnology* 20 (1): 262. https://doi.org/10.1186/s12951-022-01477-8.

Kessler, Amanda, Jonas Hedberg, Eva Blomberg, and Inger Odnevall. 2022. 'Reactive Oxygen Species Formed by Metal and Metal Oxide Nanoparticles in Physiological Media-A Review of Reactions of Importance to Nanotoxicity and Proposal for Categorization'. *Nanomaterials (Basel, Switzerland)* 12 (11): 1922. https://doi.org/10.3390/nano12111922.

Keurentjes, Anne J., Ivone Jakasa, and Sanja Kezic. 2021. 'Research Techniques Made Simple: Stratum Corneum Tape Stripping'. *Journal of Investigative Dermatology* 141 (5): 1129-1133.e1. https://doi.org/10.1016/j.jid.2021.01.004.

Khushnood, Muhammad. 2024. 'Nanomaterials: Surface Area to Volume Ratio'. *Journal of Materials Science and Nanomaterials* 8 (5): 1–3. https://doi.org/10.4172/jmsn.1000159.

Kohl, Yvonne, Elise Rundén-Pran, Espen Mariussen, et al. 2020. 'Genotoxicity of Nanomaterials: Advanced In Vitro Models and High Throughput Methods for Human Hazard Assessment—A Review'. *Nanomaterials* 10 (10): 1911. https://doi.org/10.3390/nano10101911.

Koltsov, Denis, and Iwona Koltsov. 2017. 'Application of Nanomaterials to Industry: How Are Nanomaterials Used and What Drives Future Applications?' In *Metrology and Standardization of Nanotechnology*. John Wiley & Sons, Ltd. https://doi.org/10.1002/9783527800308.ch26.

Kumar, Rajesh, O. Al-Dossary, Girish Kumar, and Ahmad Umar. 2015. 'Zinc Oxide Nanostructures for NO2 Gas–Sensor Applications: A Review'. *Nano-Micro Letters* 7 (2): 97–120. https://doi.org/10.1007/s40820-014-0023-3.

Labouta, Hagar I., and Marc Schneider. 2013. 'Interaction of Inorganic Nanoparticles with the Skin Barrier: Current Status and Critical Review'. *Nanomedicine: Nanotechnology, Biology, and Medicine* 9 (1): 39–54. https://doi.org/10.1016/j.nano.2012.04.004.

Larese Filon, Francesca. 2017. 'Skin Exposure to Nanoparticles and Possible Sensitization Risk'. In *Allergy and Immunotoxicology in Occupational Health*, edited by Takemi Otsuki, Claudia Petrarca, and Mario Di Gioacchino. Springer. https://doi.org/10.1007/978-981-10-0351-6_11.

Larese Filon, Francesca, Dhimiter Bello, John W. Cherrie, Anne Sleeuwenhoek, Suzanne Spaan, and Derk H. Brouwer. 2016. 'Occupational Dermal Exposure to Nanoparticles and Nano-Enabled Products: Part I-Factors Affecting Skin Absorption'. *International Journal of Hygiene and Environmental Health* 219 (6): 536–44. https://doi.org/10.1016/j.ijheh.2016.05.009.

Larese Filon, Francesca, Matteo Crosera, Marcella Mauro, et al. 2016. 'Palladium Nanoparticles Exposure: Evaluation of Permeation through Damaged and Intact Human Skin'. *Environmental Pollution* 214 (July): 497–503. https://doi.org/10.1016/j.envpol.2016.04.077.

Larese Filon, Francesca, Giovanna Marussi, Mickael Payet, et al. 2025. 'Skin Absorption of Metals Derived from Hydrogenated Stainless Particles in Human Skin: Results from the TITANS Project'. *Environmental Pollution* 364 (January): 125327. https://doi.org/10.1016/j.envpol.2024.125327.

Larese Filon, Francesca, Marcella Mauro, Gianpiero Adami, Massimo Bovenzi, and Matteo Crosera. 2015. 'Nanoparticles Skin Absorption: New Aspects for a Safety Profile Evaluation'. *Regulatory Toxicology and Pharmacology* 72 (2): 310–22. https://doi.org/10.1016/j.yrtph.2015.05.005.

Larese, Francesca Filon, Flavia D'Agostin, Matteo Crosera, et al. 2009. 'Human Skin Penetration of Silver Nanoparticles through Intact and Damaged Skin'. *Toxicology* 255 (1–2): 33–37. https://doi.org/10.1016/j.tox.2008.09.025.

Larese, Francesca, Adami Gianpietro, Marta Venier, Giovanni Maina, and Nadia Renzi. 2007. 'In Vitro Percutaneous Absorption of Metal Compounds'. *Toxicology Letters* 170 (1): 49–56. https://doi.org/10.1016/j.toxlet.2007.02.009.

Leikauf, George D., Sang-Heon Kim, and An-Soo Jang. 2020. 'Mechanisms of Ultrafine Particle-Induced Respiratory Health Effects'. *Experimental & Molecular Medicine* 52 (3): 329–37. https://doi.org/10.1038/s12276-020-0394-0.

Li, Can, N. Clament Sagaya Selvam, and Jiye Fang. 2023. 'Shape-Controlled Synthesis of Platinum-Based Nanocrystals and Their Electrocatalytic Applications in Fuel Cells'. *Nano-Micro Letters* 15 (1): 83. https://doi.org/10.1007/s40820-023-01060-2.

Li, Jingya, Daolei Cui, Ziyue Yang, et al. 2024. 'Health Risk Assessment of Heavy Metal(Loid)s in Road Dust via Dermal Exposure Pathway from a Low Latitude Plateau Provincial Capital City: The Importance of Toxicological Verification'. *Environmental Research* 252 (July): 118890. https://doi.org/10.1016/j.envres.2024.118890.

Li, K. G., J. T. Chen, S. S. Bai, et al. 2009. 'Intracellular Oxidative Stress and Cadmium Ions Release Induce Cytotoxicity of Unmodified Cadmium Sulfide Quantum Dots'. *Toxicology in Vitro* 23 (6): 1007–13. https://doi.org/10.1016/j.tiv.2009.06.020.

Lin, Xubo, Yi Y. Zuo, and Ning Gu. 2015. 'Shape Affects the Interactions of Nanoparticles with Pulmonary Surfactant'. *Science China Materials* 58 (1): 28–37. https://doi.org/10.1007/s40843-014-0018-5.

Liu, Yuewei, Catherine C. Beaucham, Terri A. Pearce, and Ziqing Zhuang. 2014. 'Assessment of Two Portable Real-Time Particle Monitors Used in Nanomaterial Workplace Exposure Evaluations'. *PLOS ONE* 9 (8): e105769. https://doi.org/10.1371/journal.pone.0105769.

Lizonova, Denisa, Amogh Nagarkar, Philip Demokritou, and Georgios A. Kelesidis. 2024. 'Effective Density of Inhaled Environmental and Engineered Nanoparticles and Its Impact on the Lung Deposition and Dosimetry'. *Particle and Fibre Toxicology* 21 (1): 7. https://doi.org/10.1186/s12989-024-00567-9.

Lowney, Yvette W., Michael V. Ruby, Ronald C. Wester, et al. 2005. 'Percutaneous Absorption of Arsenic from Environmental Media'. *Toxicology and Industrial Health* 21 (1–2): 1–14. https://doi.org/10.1191/0748233705th205oa.

Lowney, Yvette W., Ronald C. Wester, Rosalind A. Schoof, Colleen A. Cushing, Melanie Edwards, and Michael V. Ruby. 2007. 'Dermal Absorption of Arsenic from Soils as Measured in the Rhesus Monkey'. *Toxicological Sciences: An Official Journal of the Society of Toxicology* 100 (2): 381–92. https://doi.org/10.1093/toxsci/kfm175.

Lu, Bingqing, Jiaqi Wang, A. Jan Hendriks, and Tom M. Nolte. 2024. 'Clearance of Nanoparticles from Blood: Effects of Hydrodynamic Size and Surface Coatings'. *Environmental Science: Nano* 11 (1): 406–17. https://doi.org/10.1039/D3EN00812F.

Magnano, Greta Camilla, Giovanna Marussi, Matteo Crosera, et al. 2024. 'Probing the Effectiveness of Barrier Creams against Human Skin Penetration of Nickel Powder'. *International Journal of Cosmetic Science* 46 (1): 39–50. https://doi.org/10.1111/ics.12893.

Magnano, Greta Camilla, Giovanna Marussi, Elena Pavoni, Gianpiero Adami, Francesca Larese Filon, and Matteo Crosera. 2022. 'Percutaneous Metals Absorption Following Exposure to Road Dust Powder'. *Environmental Pollution* 292 (January): 118353. https://doi.org/10.1016/j.envpol.2021.118353.

Ma-Hock, L., S. Brill, W. Wohlleben, et al. 2012. 'Short Term Inhalation Toxicity of a Liquid Aerosol of CdS/$Cd(OH)_2$ Core Shell Quantum Dots in Male Wistar Rats'. *Toxicology Letters* 208 (2): 115–24. https://doi.org/10.1016/j.toxlet.2011.10.011.

Mancini, Michael C., Brad A. Kairdolf, Andrew M. Smith, and Shuming Nie. 2008. 'Oxidative Quenching and Degradation of Polymer-Encapsulated Quantum Dots: New Insights into the Long Term Fate and Toxicity of Nanocrystals In-Vivo'. *Journal of the American Chemical Society* 130 (33): 10836–37. https://doi.org/10.1021/ja8040477.

Marin Villegas, Carlos A., and Gerald J. Zagury. 2023. 'Metal(Loid) Speciation in Dermal Bioaccessibility Extracts from Contaminated Soils and Permeation through Synthetic Skin'. *Journal of Hazardous Materials* 455 (August): 131523. https://doi.org/10.1016/j.jhazmat.2023.131523.

Mauro, Marcella, Matteo Crosera, Marco Pelin, et al. 2015. 'Cobalt Oxide Nanoparticles: Behavior towards Intact and Impaired Human Skin and Keratinocytes Toxicity'. *International Journal of Environmental Research and Public Health* 12 (7): 8263–80. https://doi.org/10.3390/ijerph120708263.

Medici, Serenella, Massimiliano Peana, Alessio Pelucelli, and Maria Antonietta Zoroddu. 2021. 'An Updated Overview on Metal Nanoparticles Toxicity'. *Seminars in Cancer Biology*, Metal Carcinogenesis, vol. 76 (November): 17–26. https://doi.org/10.1016/j.semcancer.2021.06.020.

Misra, Chandan, Manisha Singh, Si Shen, Constantinos Sioutas, and Peter M Hall. 2002. 'Development and Evaluation of a Personal Cascade Impactor Sampler (PCIS)'. *Journal of Aerosol Science* 33 (7): 1027–47. https://doi.org/10.1016/S0021-8502(02)00055-1.

Mo, Dan, Liang Hu, Guangming Zeng, et al. 2017. 'Cadmium-Containing Quantum Dots: Properties, Applications, and Toxicity'. *Applied Microbiology and Biotechnology* 101 (7): 2713–33. https://doi.org/10.1007/s00253-017-8140-9.

Monteiro-Riviere, N. A., and L. W. Zhang. 2009. 'Assessment of Quantum Dot Penetration into Skin in Different Species Under Different Mechanical Actions'. In *Nanomaterials: Risks and Benefits*, edited by Igor Linkov and Jeffery Steevens. NATO Science for Peace and Security Series C: Environmental Security. Springer Netherlands. https://doi.org/10.1007/978-1-4020-9491-0_3.

Navarro, Divina A., Sarbajit Banerjee, Diana S. Aga, and David F. Watson. 2010. 'Partitioning of Hydrophobic CdSe Quantum Dots into Aqueous Dispersions of Humic Substances: Influence of Capping-Group Functionality on the Phase-Transfer Mechanism'. *Journal of Colloid and Interface Science* 348 (1): 119–28. https://doi.org/10.1016/j.jcis.2010.04.021.

Nguyen, Chi H., Chao Zeng, Scott Boitano, Jim A. Field, and Reyes Sierra-Alvarez. 2020. 'Cytotoxicity Assessment of Gallium- and Indium-Based Nanoparticles Toward Human Bronchial Epithelial Cells Using an Impedance-Based Real-Time Cell Analyzer'. *International Journal of Toxicology* 39 (3): 218–31. https://doi.org/10.1177/1091581820914255.

Nguyen, Kathy C., Peter Rippstein, Azam F. Tayabali, and William G. Willmore. 2015. 'Mitochondrial Toxicity of Cadmium Telluride Quantum Dot Nanoparticles in Mammalian Hepatocytes'. *Toxicological Sciences* 146 (1): 31–42. https://doi.org/10.1093/toxsci/kfv068.

NIOSH Risk Assessment of Engineered Nanomaterials | Blogs | CDC. 2024. June 3. https://blogs.cdc.gov/niosh-science-blog/2024/06/03/nano_20_risk/.

Nurchi, Valeria M., Aleksandra Buha Djordjevic, Guido Crisponi, Jan Alexander, Geir Bjørklund, and Jan Aaseth. 2020. 'Arsenic Toxicity: Molecular Targets and Therapeutic Agents'. *Biomolecules* 10 (2): 235. https://doi.org/10.3390/biom10020235.

OECD. n.d. 'OECD Series on the Safety of Manufactured Nanomaterials and Other Advanced Materials'. Accessed 28 February 2025. https://www.oecd.org/en/publications/oecd-series-on-the-safety-of-manufactured-nanomaterials-and-other-advanced-materials_e7a5fc17-en.html.

Ouypornkochagorn, Sairoong, and Jörg Feldmann. 2010. 'Dermal Uptake of Arsenic through Human Skin Depends Strongly on Its Speciation'. *Environmental Science & Technology* 44 (10): 3972–78. https://doi.org/10.1021/es903667y.

Paesano, Laura, Alessio Perotti, Annamaria Buschini, et al. 2016. 'Markers for Toxicity to HepG2 Exposed to Cadmium Sulphide Quantum Dots; Damage to Mitochondria'. *Toxicology* 374 (December): 18–28. https://doi.org/10.1016/j.tox.2016.11.012.

Pandiyaraj, Vaanmathy, Ankita Murmu, Saravana Kumari Pandy, Murugan Sevanan, and Shanamitha Arjunan. 2023. 'Metal Nanoparticles and Its Application on Phenolic and Heavy Metal Pollutants'. Physical Sciences Reviews. *Physical Sciences Reviews* 8 (10): 2879–97. https://doi.org/10.1515/psr-2021-0058.

Portugal, José, Carmen Bedia, Fulvio Amato, et al. 2024. 'Toxicity of Airborne Nanoparticles: Facts and Challenges'. *Environment International* 190 (August): 108889. https://doi.org/10.1016/j.envint.2024.108889.

Prow, Tarl W., Nancy A. Monteiro-Riviere, Alfred O. Inman, et al. 2012. 'Quantum Dot Penetration into Viable Human Skin'. *Nanotoxicology* 6 (2): 173–85. https://doi.org/10.3109/17435390.2011.569092.

Ramanavicius, Simonas, Arunas Jagminas, and Arunas Ramanavicius. 2022. 'Gas Sensors Based on Titanium Oxides (Review)'. *Coatings* 12 (5): 5. https://doi.org/10.3390/coatings12050699.

Ramos-Ruiz, Adriana, James A. Field, Wenjie Sun, and Reyes Sierra-Alvarez. 2018. 'Gallium Arsenide (GaAs) Leaching Behavior and Surface Chemistry Changes in Response to pH and O2'. *Waste Management* 77 (July): 1–9. https://doi.org/10.1016/j.wasman.2018.04.027.

Ratnaike, R. N. 2003. 'Acute and Chronic Arsenic Toxicity'. *Postgraduate Medical Journal* 79 (933): 391–96. https://doi.org/10.1136/pmj.79.933.391.

Repetto, Guillermo, Ana del Peso, and Sara Maisanaba. 2023. 'Gallium, Indium, and Thallium'. In *Patty's Toxicology*. John Wiley & Sons, Ltd. https://doi.org/10.1002/0471125474.tox032.pub3.

Roberts, Jenny R., James M. Antonini, Dale W. Porter, et al. 2013. 'Lung Toxicity and Biodistribution of Cd/Se-ZnS Quantum Dots with Different Surface Functional Groups after Pulmonary Exposure in Rats'. *Particle and Fibre Toxicology* 10 (1): 5. https://doi.org/10.1186/1743-8977-10-5.

Robins, R. G. 1981. 'The Solubility of Metal Arsenates'. *Metallurgical Transactions B* 12 (1): 103–9. https://doi.org/10.1007/BF02674763.

Rosner, Mitchell H., and Dean E. Carter. 1987. 'Metabolism and Excretion of Gallium Arsenide and Arsenic Oxides by Hamsters Following Intratracheal Instillation'. *Fundamental and Applied Toxicology* 9 (4): 730–37. https://doi.org/10.1016/0272-0590(87)90180-1.

Ryman-Rasmussen, Jessica P., Jim E. Riviere, and Nancy A. Monteiro-Riviere. 2006. 'Penetration of Intact Skin by Quantum Dots with Diverse Physicochemical Properties'. *Toxicological Sciences* 91 (1): 159–65. https://doi.org/10.1093/toxsci/kfj122.

Saadh, Mohamed J., Wajida Ataallah Khidr, Karar H. Alfarttoosi, et al. 2025. 'Metal Nanoparticles as a Promising Therapeutic Approach for Prostate Cancer Diagnosis and Therapy: A Comprehensive Review'. *Medical Oncology (Northwood, London, England)* 42 (4): 83. https://doi.org/10.1007/s12032-025-02633-4.

Sahu, Saura C, and A Wallace Hayes. 2017. 'Toxicity of Nanomaterials Found in Human Environment: A Literature Review'. *Toxicology Research and Application* 1 (January): 2397847317726352. https://doi.org/10.1177/2397847317726352.

Saleh, Tawfik A. 2020. 'Nanomaterials: Classification, Properties, and Environmental Toxicities'. *Environmental Technology & Innovation* 20 (November): 101067. https://doi.org/10.1016/j.eti.2020.101067.

'Sampling and Analytical Methods | Occupational Safety and Health Administration'. n.d. Accessed 13 June 2025. https://www.osha.gov/chemicaldata/sampling-analytical-methods.

Sayes, Christie M., and David B. Warheit. 2009. 'Characterization of Nanomaterials for Toxicity Assessment'. *WIREs Nanomedicine and Nanobiotechnology* 1 (6): 660–70. https://doi.org/10.1002/wnan.58.

Scafa Udriște, Alexandru, Alexandra Cristina Burdușel, Adelina-Gabriela Niculescu, Marius Rădulescu, and Alexandru Mihai Grumezescu. 2024. 'Metal-Based Nanoparticles for Cardiovascular Diseases'. *International Journal of Molecular Sciences* 25 (2): 2. https://doi.org/10.3390/ijms25021001.

Senapati, Violet Aileen, and Ashutosh Kumar. 2018. 'ZnO Nanoparticles Dissolution, Penetration and Toxicity in Human Epidermal Cells. Influence of pH'. *Environmental Chemistry Letters* 16 (3): 1129–35. https://doi.org/10.1007/s10311-018-0736-5.

Sengul, Ayse Busra, and Eylem Asmatulu. 2020. 'Toxicity of Metal and Metal Oxide Nanoparticles: A Review'. *Environmental Chemistry Letters* 18 (5): 1659–83. https://doi.org/10.1007/s10311-020-01033-6.

Shukla, Ritesh K., Ashish Badiye, Kamayani Vajpayee, and Neeti Kapoor. 2021. 'Genotoxic Potential of Nanoparticles: Structural and Functional Modifications in DNA'. *Frontiers in Genetics* 12 (September). https://doi.org/10.3389/fgene.2021.728250.

Siddique, Sarkar, and James C. L. Chow. 2020. 'Gold Nanoparticles for Drug Delivery and Cancer Therapy'. *Applied Sciences* 10 (11): 11. https://doi.org/10.3390/app10113824.

Sonwani, Saurabh, Simran Madaan, Jagjot Arora, et al. 2021. 'Inhalation Exposure to Atmospheric Nanoparticles and Its Associated Impacts on Human Health: A Review'. *Frontiers in Sustainable Cities* 3 (August). https://doi.org/10.3389/frsc.2021.690444.

Srikanth, Koigoora. 2020. 'Routes of Exposures and Toxicity of Nanoparticles'. In *Model Organisms to Study Biological Activities and Toxicity of Nanoparticles*, edited by Busi Siddhardha, Madhu Dyavaiah, and Kaviyarasu Kasinathan. Springer. https://doi.org/10.1007/978-981-15-1702-0_13.

Sukhanova, Alyona, Svetlana Bozrova, Pavel Sokolov, Mikhail Berestovoy, Alexander Karaulov, and Igor Nabiev. 2018. 'Dependence of Nanoparticle Toxicity on Their Physical and Chemical Properties'. *Nanoscale Research Letters* 13 (1): 44. https://doi.org/10.1186/s11671-018-2457-x.

Sze, S. M., Yiming Li, and Kwok Kwok Ng. 2021. *Physics of Semiconductor Devices*. Fourth edition. Wiley.

Tanaka, Akiyo. 2004. 'Toxicity of Indium Arsenide, Gallium Arsenide, and Aluminium Gallium Arsenide'. *Toxicology and Applied Pharmacology* 198 (3): 405–11. https://doi.org/10.1016/j.taap.2003.10.019.

Teleanu, Daniel Mihai, Cristina Chircov, Alexandru Mihai Grumezescu, Adrian Volceanov, and Raluca Ioana Teleanu. 2018. 'Impact of Nanoparticles on Brain Health: An Up to Date Overview'. *Journal of Clinical Medicine* 7 (12): 12. https://doi.org/10.3390/jcm7120490.

Thanachoksawang, Chatchai, Panida Navasumrit, Potchanee Hunsonti, et al. 2022. 'Exposure to Airborne Iron Oxide Nanoparticles Induces Oxidative DNA Damage and Inflammatory Responses: A Pilot Study in Welders and in Human Lung Epithelial Cell Line'. *Toxicology and Environmental Health Sciences* 14 (4): 339–49. https://doi.org/10.1007/s13530-022-00148-3.

Tsoi, Kim M., Qin Dai, Benjamin A. Alman, and Warren C. W. Chan. 2013. 'Are Quantum Dots Toxic? Exploring the Discrepancy Between Cell Culture and Animal Studies'. *Accounts of Chemical Research* 46 (3): 662–71. https://doi.org/10.1021/ar300040z.

Turkall, Rita M., Gloria A. Skowronski, Duck H. Suh, and Mohamed S. Abdel-Rahman. 2003. 'Effect of a Chemical Mixture on Dermal Penetration of Arsenic and Nickel in Male Pig in Vitro'. *Journal of Toxicology and Environmental Health. Part A* 66 (7): 647–55. https://doi.org/10.1080/15287390309353772.

'UNI EN 17058:2019 - UNI Ente Italiano Di Normazione'. n.d. Accessed 13 June 2025. https://store.uni.com/uni-en-17058-2019.

Valdiglesias, Vanessa, Natalia Fernández-Bertólez, Gözde Kiliç, et al. 2016. 'Are Iron Oxide Nanoparticles Safe? Current Knowledge and Future Perspectives'. *Journal of Trace Elements in Medicine and Biology*, ISTERH congress, vol. 38 (December): 53–63. https://doi.org/10.1016/j.jtemb.2016.03.017.

Vijiyakumar, Naveen, and Sabina Evan Prince. 2025. 'A Comprehensive Review of Cadmium-Induced Toxicity, Signalling Pathways, and Potential Mitigation Strategies'. *Toxicology and Environmental Health Sciences* 17 (1): 79–94. https://doi.org/10.1007/s13530-024-00243-7.

Wang, Junfeng, Chunyang Jiang, Mohamed Alattar, et al. 2015. 'Oxidative Injury Induced by Cadmium Sulfide Nanoparticles in A549 Cells and Rat Lungs'. *Inhalation Toxicology* 27 (12): 649–58. https://doi.org/10.3109/08958378.2015.1088599.

Wang, Xiaomei, Jinglin Tian, Ken-Tye Yong, et al. 2016. 'Immunotoxicity Assessment of CdSe/ZnS Quantum Dots in Macrophages, Lymphocytes and BALB/c Mice'. *Journal of Nanobiotechnology* 14 (1): 10. https://doi.org/10.1186/s12951-016-0162-4.

Wang, Yu, Yilei Mo, Yingwei Sun, et al. 2024. 'Intestinal Nanoparticle Delivery and Cellular Response: A Review of the Bidirectional Nanoparticle-Cell Interplay in Mucosa Based on Physiochemical Properties'. *Journal of Nanobiotechnology* 22 (1): 669. https://doi.org/10.1186/s12951-024-02930-6.

Wang, Yung-Li, Yu-Hsuan Lee, Chu-Lin Chou, Yu-Sheng Chang, Wen-Chih Liu, and Hui-Wen Chiu. 2024. 'Oxidative Stress and Potential Effects of Metal Nanoparticles: A Review of Biocompatibility and Toxicity Concerns'. *Environmental Pollution* 346 (April): 123617. https://doi.org/10.1016/j.envpol.2024.123617.

Webb, D. R., I. G. Sipes, and D. E. Carter. 1984. 'In Vitro Solubility and in Vivo Toxicity of Gallium Arsenide'. *Toxicology and Applied Pharmacology* 76 (1): 96–104. https://doi.org/10.1016/0041-008x(84)90032-2.

Webb, D. R., S. E. Wilson, and D. E. Carter. 1986a. 'Comparative Pulmonary Toxicity of Gallium Arsenide, Gallium(III) Oxide, or Arsenic(III) Oxide Intratracheally Instilled into Rats'. *Toxicology and Applied Pharmacology* 82 (3): 405–16. https://doi.org/10.1016/0041-008X(86)90276-0.

Webb, D. R., S. E. Wilson, and D. E. Carter. 1986b. 'Comparative Pulmonary Toxicity of Gallium Arsenide, Gallium(III) Oxide, or Arsenic(III) Oxide Intratracheally Instilled into Rats'. *Toxicology and Applied Pharmacology* 82 (3): 405–16. https://doi.org/10.1016/0041-008X(86)90276-0.

Wen, Tao, Jianbo Liu, Weiwei He, and Aiyun Yang. 2020. 'Nanomaterials and Reactive Oxygen Species (ROS)'. In *Nanotechnology in Regenerative Medicine and Drug Delivery Therapy*, edited by Haiyan Xu and Ning Gu. Springer. https://doi.org/10.1007/978-981-15-5386-8_8.

Wester, R. C., H. I. Maibach, L. Sedik, J. Melendres, and M. Wade. 1993. 'In Vivo and in Vitro Percutaneous Absorption and Skin Decontamination of Arsenic from Water and Soil'. *Fundamental and Applied Toxicology: Official Journal of the Society of Toxicology* 20 (3): 336–40. https://doi.org/10.1006/faat.1993.1043.

Williams, Faith M. 2004. 'EDETOX. Evaluations and Predictions of Dermal Absorption of Toxic Chemicals'. *International Archives of Occupational and Environmental Health* 77 (2): 150–51. https://doi.org/10.1007/s00420-003-0484-z.

Wu, Tianshu, Keyu He, Qinglin Zhan, et al. 2015. 'Partial Protection of N-Acetylcysteine against MPA-Capped CdTe Quantum Dot-Induced Neurotoxicity in Rat Primary Cultured Hippocampal Neurons'. *Toxicology Research* 4 (6): 1613–22. https://doi.org/10.1039/c5tx00127g.

Xu, Houjun, Qingzhao Li, Yu Su, Yulan Hao, Licheng Yan, and Haijuan An. 2012. 'The Study on Toxicokinetics and Distribution of CdSe Quantum Dots in Rats'. In *Green Communications and Networks*, edited by Yuhang Yang and Maode Ma. Springer Netherlands. https://doi.org/10.1007/978-94-007-2169-2_161.

Xuan, Yang, Wenliang Zhang, Xinjiang Zhu, and Shubiao Zhang. 2023. 'An Updated Overview of Some Factors That Influence the Biological Effects of Nanoparticles'. *Frontiers in Bioengineering and Biotechnology* 11 (August). https://doi.org/10.3389/fbioe.2023.1254861.

Xue, Bing, Da-Wei Deng, Jie Cao, et al. 2012. 'Synthesis of NAC Capped near Infrared-Emitting CdTeS Alloyed Quantum Dots and Application for in Vivo Early Tumor Imaging'. *Dalton Transactions* 41 (16): 4935–47. https://doi.org/10.1039/C2DT12436J.

Yang, Xiupei, Zhihui Jia, Xiumei Cheng, Na Luo, and Martin M.F. Choi. 2018. 'Synthesis of N-Acetyl-l-Cysteine Capped Mn:Doped CdS Quantum Dots for Quantitative Detection of Copper Ions'. *Spectrochimica Acta Part A: Molecular and Biomolecular Spectroscopy* 199 (Complete): 455–61. https://doi.org/10.1016/j.saa.2018.04.003.

Yong, Ken-Tye, Wing-Cheung Law, Rui Hu, et al. 2013. 'Nanotoxicity Assessment of Quantum Dots: From Cellular to Primate Studies'. *Chemical Society Reviews* 42 (3): 1236–50. https://doi.org/10.1039/C2CS35392J.

Zanette, Caterina, and Giovanni Maina. 2009. 'Nanoparticle Dermal Absorption and Toxicity: A Review of the Literature'. *International Archives of Occupational and Environmental Health*, January

1.
https://www.academia.edu/17154511/Nanoparticle_dermal_absorption_and_toxicity_a_review_of_the_literature.

Zhang, Bokun, Xiaoyun Wang, Shuai Wang, et al. 2025. 'High-Energy-Density Lithium Manganese Iron Phosphate for Lithium-Ion Batteries: Progresses, Challenges, and Prospects'. *Journal of Energy Chemistry* 100 (January): 1–17. https://doi.org/10.1016/j.jechem.2024.08.011.

Zhang, Junhui, Maziar Ahmadi, Gemma Fargas, et al. 2022. 'Silver Nanoparticles for Conductive Inks: From Synthesis and Ink Formulation to Their Use in Printing Technologies'. *Metals* 12 (2): 2. https://doi.org/10.3390/met12020234.

Zhang, Naiding, Guiya Xiong, and Zhenjie Liu. 2022. 'Toxicity of Metal-Based Nanoparticles: Challenges in the Nano Era'. *Frontiers in Bioengineering and Biotechnology* 10 (November). https://doi.org/10.3389/fbioe.2022.1001572.

Zhang, Ting, Yuanyuan Hu, Meng Tang, et al. 2015. 'Liver Toxicity of Cadmium Telluride Quantum Dots (CdTe QDs) Due to Oxidative Stress in Vitro and in Vivo'. *International Journal of Molecular Sciences* 16 (10): 10. https://doi.org/10.3390/ijms161023279.

Zhao, Dan, Zhike He, Pui Shan Chan, et al. 2010. 'NAC-Capped Quantum Dot as Nuclear Staining Agent for Living Cells via an In Vivo Steering Strategy'. *The Journal of Physical Chemistry C* 114 (14): 6216–21. https://doi.org/10.1021/jp908418v.

Zhou, Jun, and Didier Astruc. 2024. 'Recent Trends and Perspectives in Palladium Nanocatalysis: From Nanoparticles to Frameworks, Atomically Precise Nanoclusters and Single-Atom Catalysts'. *Journal of Inorganic and Organometallic Polymers and Materials* 34 (7): 2903–25. https://doi.org/10.1007/s10904-024-03037-z.

Z. Janković, Nina, and Desirée L. Plata. 2019. 'Engineered Nanomaterials in the Context of Global Element Cycles'. *Environmental Science: Nano* 6 (9): 2697–711. https://doi.org/10.1039/C9EN00322C.

7. ANNEX

Questionnaire for assessing personal exposure to arsenic

Smoke: YES NO

If yes how many cigarettes per day on average

Use of paints: YES NO

Food habits:

Indicate the consumption of the following products

Consumption in grams

Consumption in grams	**Last week**	**Average weekly**	**Average monthly**
RICE:			
MILK RICE:			
CEREALS CONTAINING RICE:			
WHOLEGRAIN CEREALS:			
PRODUCTS CONTAINING WHOLE GRAINS:			
BIVALVE MOLLUSCS:			
CRUSTACEANS:			
CEPHALOPODS:			
FISH:			
FISH PRODUCTS:			
PLANT FOOD SUPPLEMENTS:			
ALGAE:			
FOOD PRODUCTS CONTAINING ALGAE:			